Università degli Studi di Napoli Federico II

Ph.D. School in Earth Sciences, Environment and Resources

XXXII Cycle

Ph.D. Thesis

Architecture of active fault zones by non-conventional 3D ERT technique. Applications to southern Apennines areas

Claudio De Paola

Supervisor

Prof. Rosa Di Maio

Co-supervisor

Dott. Ester Piegari

2019

CONTENTS

INTRODUCTION

This project aims at developing a methodology for reconstructing the architecture of active faults and modeling the processes that control the passage of gas and fluids within the damage zone through the integration of geophysical, geological and geochemical data. In particular, the use of a non-conventional 3D electrical resistivity tomography (ERT) technique is proposed and its efficiency is demonstrated by comparing the results of its application with those from standard procedures. After testing, it has been applied for the geoelectrical characterization of an active fault zone affected by an intense CO_2 degassing, allowing the 3D accurate characterization of the shallower part of the damage zone, as well as the 3D reconstruction of the complex CO_2 migration pathways shape.

The knowledge of regional seismic hazard passes through the identification and characterization of active faults. The palaeoseismological analyses provide key elements to interpret the seismogenic behavior of a fault and to define, in the best cases, magnitude, movement rate, return times and elapsed time of historical earthquakes.

The interpretation of geomorphological and structural features is a principal tool for Neotectonics, Earthquake Geology and Paleoseismology. However, it is also a major tool for seismic hazard assessment. There is an emerging tendency and need for incorporating fault specific information relating both to the identification and mapping of active faults, as well as extracting information regarding the recurrence interval of associated potential earthquakes. The geomorphology of active faulting has a dominant role in gathering such data. However, in some geological contexts, these elements can fail either for generally erosive phenomena or, more simply, for lack of competition between movement rates and exogenous dynamics. In these cases, the use of indirect methodologies, such as geophysical ones, plays a propaedeutic and decisive role in the study of active fault zones, providing a

fundamental contribution both for the physical identification of the possible fault emergence zone and for the definition of the geometry and dimension of the basin formed in the hanging wall, as for the case of Apennines normal faults.

The rise of gas along seismically active faults is the superficial manifestation of a migration path of gases from a deep natural source, and it indicates how the active fault segments are characterized by high permeability and porosity, acting as drains in the crust. If these gases reach the surface, they are usually discharged into the atmosphere from small areas known as *gas vents*. Understanding gas migration along fault systems is one of the key scientific problems in many geological research fields, such as geothermal exploration and gas risk assessment. In geothermal areas, large quantities of CO_2 are produced through thermo-metamorphic reactions and migrate to the surface along channels permeated by gases in fault and/or fracture systems. The strong focus is due to the potential impact of the natural release of CO_2 on human health and ecosystems, groundwater quality, soil mineralogy and CO_2 concentrations in the atmosphere.

For the purposes of the gas hazard assessment, the geophysical prospecting methods are successfully and increasingly applied for the identification of active faults and for the detection and monitoring of CO_2 degassing, both in volcanic and non-volcanic areas. In particular, over the last decade, geoelectrical surveys performed by electrical resistivity tomography (ERT) techniques have proven to be among the most appropriate methods to detect spatial distributions of carbon dioxide (Kiessling et al., 2010; Schmidt-Hattenberger et al., 2011; Bergmann et al., 2012; Furre et al. 2017), whose emission in non-volcanic areas is essentially controlled by fractures, faults and/or fault damage zones. The ERT prospecting can be performed to define 2D, 2.5D, 3D and 4D subsurface models. In particular, the unconventional 3D ERT data acquisition technique experienced in this PhD project, aims at defining the architecture of active fault zones in Ailano and Ciorlano areas

(Matese Mts., southern Italy), which control significant CO_2 flows (Ascione et al., 2017; Valente et al., 2017). The achievement of this goal, through the innovative geophysical technique proposed in this study, is essential not only to define the geoemtry of the active seismic zone, but also to understand the processes that govern the fluid flow along the damage zone that convey the gases towards the surface. Indeed, electrical resistivity tomographies can identify the areas of influence of the gas vent as both conductive and resistive anomalies, depending on the geological environment and the physical, chemical and biological conditions of the investigated risk areas.

In this context, this PhD thesis proposes a multidisciplinary research approach whose final objectives are: the 3D geoelectrical reconstruction of the studied fault structure and the identification of CO_2 anomalies with complex geometry in the Ciorlano area (crest of the Matese, southern Apennines). In particular, the work is aimed at localizing and modeling the preferential paths of non-volcanic CO_2 migration in the proximity of a gas vent detected in the study area, which recent accurate geological and geochemical analyses have classified as one of those with the highest non-volcanic natural emissions of CO_2 ever measured on Earth (Ascione et al., 2018).

The different phases of the work reflect the articulation of the present thesis, which is structured in five Chapters.

The first Chapter consists of two main parts. The first presents the state of the art on the geophysical methods used to characterize active fault zones. The second part summarizes research studies that show how geophysical investigations have been applied for identifying CO_2 degassing.

In the second Chapter, the development and fine-tuning of a high-resolution 3D ERT technique based on the use of unconventional acquisition geometries is presented. In particular, first the effectiveness of such a proposed technique is

demonstrated by comparing the results of its application with those obtained from a conventional technique in the same test area. Then, two cases are presented in which this non-conventional technique has been tested and developed in complex logistical conditions. The first application concerns geoelectrical characterization and monitoring of layered pyroclastic deposits covering a steep calcareous slope, whose complex topography prevents the use of conventional electrode layouts for 3D-resistivity imaging. The second application is about the exploration of the subsoil under a historic building, which would not have been possible with conventional techniques. It is worth noting that this experimental phase allowed to optimize the proposed non-conventional 3D ERT technique and to obtain a powerful tool for the 3D characterization of complex geological structures, which was then applied for the first time in a context of active faults with the presence of CO_2.

The third Chapter illustrates the geological setting of the Mt. Matese study areas, providing a review on the avalaible information on the morphological and tectonic features of the southern Apennines, with particular reference to the morpho-structural evolution of the Ciorlano area and to the hydrothermal systems of the Matese ridge.

The fourth Chapter is dedicated to the analysis of the 3D ERT data acquired in the Ailano and Ciorlano areas, whose inversion results have been used for identifying and modeling the fault zones and the active surface CO_2 degassing zones.

The fifth and last Chapter is devoted to numerical simulations of the CO_2 uprising along the main fault of Colla Sponeta, with the aim to reproduce the CO_2 fluxes measured in the area and, therefore, to get information on the rate of CO_2 released from the soil cover overlying the carbonate bedrock.

Chapter 1.

Geophysical investigations of fault zones and CO_2 degassing: state of the art

In this chapter, a brief summary of state of the art concerning the use of geophysical methods for the three-dimensional reconstruction of complex geological structures such as fault zones, as well as for the identification of CO2 degassing, is presented.

1.1 Seismic vs electrical resistivity data for structural geology studies

Geosciences, and geology in particular, deal with integrating various sources of data, often of limited, sparse and indirect nature, into scientific models. The use of limited data combined with our limited knowledge of the highly complex Earth system invariably infuses any model with uncertainty, mainly because geology is intrinsically based on interpreted data that often require reasoning about the processes that occur over geological timescales (Frodeman, 1995), which further increases the space of uncertainty. The interpretation of seismic and electrical resistivity data is the basis for constructing subsurface structural models.

Seismic reflection data interpretation is generally accomplished by correlating specific signal characteristics (seismic signature) with the different geological domains identified within the study area. Subsurface discontinuities create reflections and diffractions in seismic wave propagation (Khaidukov et al., 2004). Reflections are used conventionally to interpret structural and stratigraphic features as they are generated by interfaces with impedance contrasts. Diffractions are produced by local discontinuities that act like point-sources (Neidell and Taner, 1971; Zavalishin, 2000), becoming active as soon as the direct wave hits them.

Commonly, if such local bodies have size comparable to the seismic wavelength (Rayleigh criterion), they are ignored during processing (Khaidukov et al., 2004), and, consequently, this imposes a limit on the resolution of recorded backscattered waves (Moser and Howard, 2008; Gelius and Asgedom, 2011). A standard seismic interpretation is affected by a certain degree of uncertainty and/or subjectivity (particularly in the case of poor data quality) because it is generally based on a qualitative analysis of the amplitude, geometry, and lateral continuity of the reflections. Over the last years, the introduction of seismic attributes and related automated–semiautomated procedures has assumed an important role in reducing the subjectivity of seismic interpretations and in achieving quantitative results. A seismic attribute is a descriptive and quantifiable parameter that can be calculated on a single trace, on multiple traces, or 3D volumes and can be displayed at the same scale as the original data. Seismic data can therefore be considered a composition of constituent attributes (Taner et al., 1979; Barnes, 2000; Forte et al., 2012). The latter are measurements based on seismic data such as polarity, phase, frequency, or velocity (Dorn, 1998). They are calculated through signal and image processing algorithms and are used for both qualitative and quantitative interpretation of seismic dataset. In the nineties, seismic interpreters were making use of dip and azimuth maps (Brown, 1996). Amplitude extractions and seismic sequence attribute mapping were also established (Chopra and Marfurt, 2007). In order to reveal subtle stratigraphic features (e.g. buried deltas, river channels, reefs and dewatering structures), datasets were pre-conditioned (e.g. filtering random noise and pre-calculation of large scale linear or anisotropy features) leading to cross-correlation and coherence analysis (Marfurt and Chopra, 2007). However, due to the indirect, noisy and non-unique nature of seismic data processing into images, interpretation is inherently uncertain. This “subjective” uncertainty is in contrast to more “objective” uncertainty related to the geophysical acquisition of the data

themselves (Tannert et al., 2007; Bond, 2015). This raises the need to further understanding of the distribution of interpretational uncertainties in 3D space (Abrahamsen et al., 1992; Thore et al., 2002; Thiele et al., 2016; Godefroy et al., 2019). Additionally, the process of interpretation between seismic lines and cubes is fundamentally different and thus might lead to conceptually different uncertainties to be dominant (e.g., the need to connect fault evidence between seismic lines introduces significant uncertainty in widely spaced 2D interpretation compared to fault interpretation in seismic cubes; see Freeman et al., 1990).

The other methodology used for modeling subsoil structures is the electrical resistivity tomography (ERT). Already at the beginning of the 20th century, the geoelectric methods were used for the quantitative description of conductive anomalies identified in the subsoil (Petersson, 1907). The real turning point came in 1912, when Conrad Schlumberger in France and, about the same time, Frank Wenner in U.S.A. (Schlumberger, 1920; Kunetz, 1966) began their pioneering work, which has led today to the development of multi-electrode and multi-channel systems, to the implementation of semi-automatic processing codes and to the passage from one-dimensional analysis to interpretations in two and three dimensions of space, allowing applications in many fields, such as groundwater research, geo-environmental and civil engineering issues, natural hazard assessment, archaeological research, etc. The electrical resistivity tomography technique is an appropriate geophysical approach to obtain 2D or 3D images of the subsurface, as it represents the best compromise between high-resolution shallow geophysical methods, as the ground penetrating radar (GPR) technique, and low-resolution deep geophysical methods, as the seismic techniques (Bichler et al., 2004). In the last decades, many authors (Dahlin, 1996; Dahlin et al., 2002; Bentley and Gharibi, 2004; Gunther et al., 2006; Rucker et al., 2009) have experienced the problem related to complex 3D geophysical targets using standard 2D ERT data

acquisition techniques, and this is particularly true in case of near surface faulting and fracturing (Francese et al., 2009). A remarkable attempt to obtain 3D subsurface images using groups of parallel survey lines was proposed by Rucker et al. (2009), who applied 3D inversion procedures to apparent resistivity data acquired by 2D ERT technique along profiles, usually defined as 2.5D inversion approach. This approach, unlike a real 3D survey where transmitting and receiving electrodes are distributed in all directions of space and used simultaneously, is advantageous in terms of acquisition logistics. However, identification of faults by 2D acquisition techniques is difficult in areas of complex deformation patterns, unless a priori data (e.g. geological, geochemical, geotechnical) are used and/or the results are checked against other geophysical data (e.g. Mazzarini et al., 2009; Seminsky et al., 2016). For these geological contexts, the 3D ERT prospecting is probably the only one that is able to provide a detailed modeling of the fault architecture and of the fluid circulation along active fault systems. Fractured zones are natural preferential migration pathways for gas. Electrical resistivity tomograms identify zones of influence of gas vents as both conductive or resistive anomalies depending on the geological setting and the physical, chemical and biological soil environment of the investigated vents (Byrdina et al., 2009; Pettinelli et al., 2010).

1.1.1 Seismic surveys

Many existing interpretations of fault patterns in the subsurface imply relationships between fault geometry, displacement and strain distributed in the surrounding strata. Examples include fold-thrust systems (Boyer and Elliott, 1982; Suppe, 1983; Butler, 1987; Mitra, 1990; Suppe and Medwedeff, 1990; Cardozo et al., 2003; Butler and McCaffrey, 2004; Butler and Paton, 2010; Hardy and Allmendinger, 2011) and normal faults (Cowie and Scholz, 1992; Cartwright et al., 1995; Childs et al., 1996, 2003; Walsh et al., 2003a, b; Long and Imber, 2010; Jamieson, 2011). Fully testing

the applicability of these models demands determinations, if not of strain magnitudes, then at least descriptions of the strain patterns. The target is to map distributed deformation using seismic data (Figure 1.1).

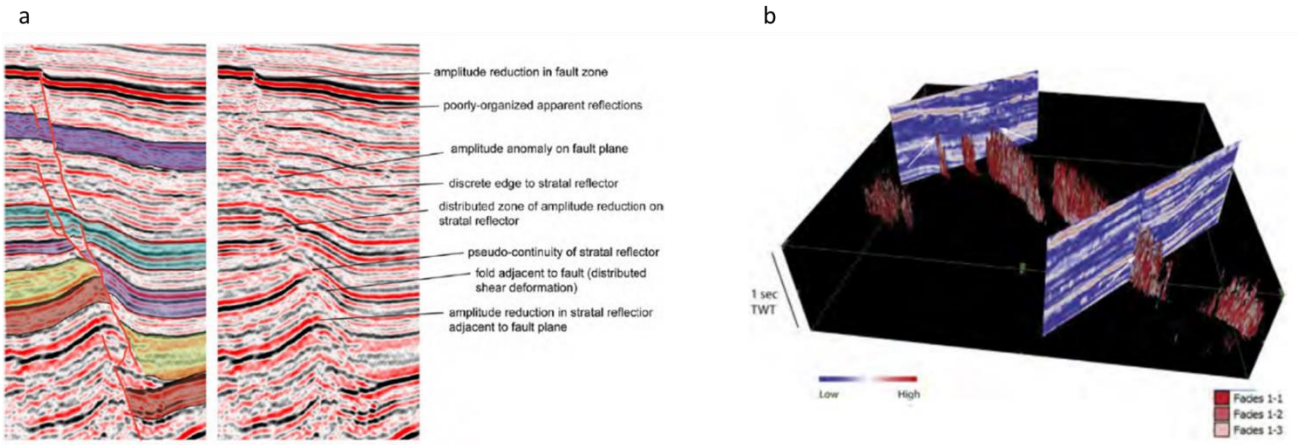

Figure 1.1 *a) Interpreted seismic image of a normal fault structure and related damage (North-sea, Virtual SA library) and relative characterization of the main reflectors along the fault structure. b) Cross-section representation of two arbitrary seismic line (expressed as envelope values) (modified from Ippoliti el al., 2016).*

Their ending is to provide an interpretational framework that could be applied to mapping volumes of deformation in the subsurface using seismic facies concepts that are well-established for high resolution stratigraphic interpretations. They use seismic attributes to provide information carried by the seismic signal that is otherwise not used in conventional seismic mapping. When interpreting stratigraphic features such as channels and marginal units to carbonate reefs (Marfurt and Chopra, 2007), different attributes are combined to create so-called "seismic texture" maps. The approach gained favor because sedimentary features with common signal character could be related to their inferred depositional environment (Fournier and Derain, 1995). Subsequently, a plethora of seismic attributes and textures have been developed using statistical measures to quantify stratigraphic interpretations by creating repeatable seismic facies to predict subsurface reservoir characteristics (Gerard and Buhrig, 1990; Evans et al., 1992;

West et al., 2002; Gao, 2003; Schlaf et al., 2005; Chopra and Marfurt, 2005; Gao, 2007; Corradi et al., 2009). Although this approach can greatly facilitate the creation of maps of striatal surfaces and, hence, the formulation of seismic stratigraphic models, this simplification can hamper understanding of subsurface structural geology (Hesthammer et al., 2001; Dutzer et al., 2009) and impact on the prediction of striatal juxtaposition and consequent models of fluid flow in hydrocarbon reservoirs (e.g. Faulkner et al., 2010).

Also, a recent study of Schaaf and Bond (2019) provides quantification of the scale of uncertainties involved in the structural interpretation of data-dense 3D seismic surveys. They show that the uncertainties recorded in 2D seismic interpretation experiments (e.g., Bond et al., 2007; Bond, 2015) are similarly seen in the interpretation of 3D seismic image data and, therefore, fault placement uncertainty strongly depends on seismic data quality.

1.1.2 Electrical resistivity tomography surveys

Among the various geophysical methods (seismic, electrical resistivity tomography, ground penetrating radar or gravimetric survey) that provide useful information about landslide geometry reconstruction and hydrological characteristics of the study areas, the electrical resistivity tomography (ERT) is among the most efficient. Shallow faults have become a frequent target of ERT in the last decade (e.g., Suzukietal., 2000; Caputo et al., 2003; Wise et al., 2003; Nguyen et al., 2005). Numerous studies, indeed, have demonstrated the success of the ERT profiling (Reynolds, 2011) in modeling structural setting of relatively complex geological areas thanks to the capability to define, in terms of electrical resistivity contrasts, the contact between different geological formations and the flexure structure produced by faulting (e.g., Di Maio et al., 2000; Park and Wernicke, 2003; Lebourg et al., 2005; Koukadaki et al., 2007; Giocoli et al., 2008; Vanneste et al., 2008; Jomard et al.,

2010; Chambers et al., 2011; Giocoli et al., 2011; Merritt et al., 2014; Seminsky et al., 2016; Uhlemann et al., 2017; Boyle et al., 2018; Břežný et al., 2018; De Paola et al., 2019). Dip-slip faults are usually observed in ERT profiles as sharp lateral resistivity contrasts caused by the juxtaposition of different sediment layers and/or by different hydrological conditions on both side of the fault (e.g., Suzuki et al., 2000; Caputo et al., 2003; Diaferia et al., 2006). As examples, Figs. 1.2 shows the results of a 2D deep ERT profile for the reconstruction of Apennine faults (Vitale et al., 2020), whilst Fig. 1.3 shows ERT shallow sections obtained along profiles distributed in the Hockai fault area (Ardenne, Belgium) (Lecocq and Camelbeeck, 2016).

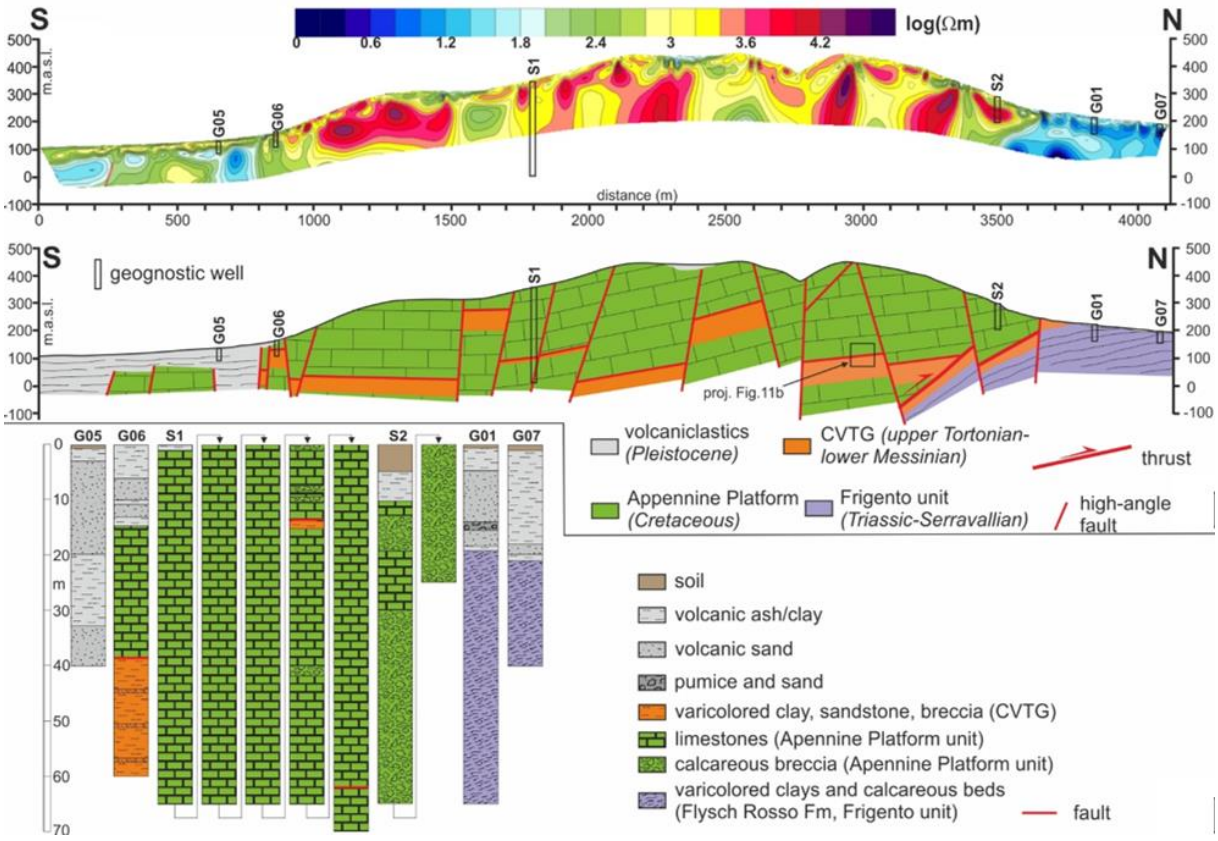

Figure 1.2 *ERT profile and relative cross-section of Apennine fault (Vitale et al., 2020).*

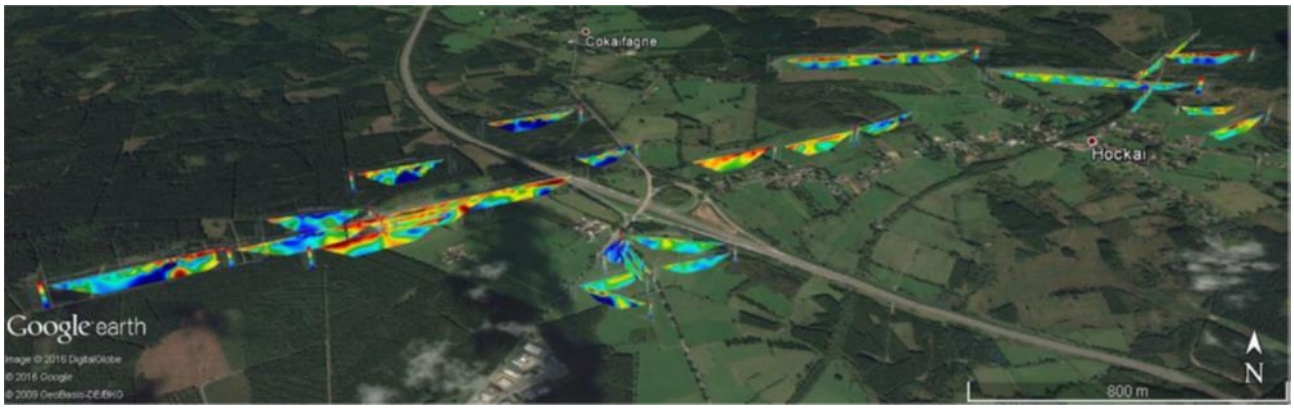

Figure 1.3 *Example of 2D electrical resistivity tomographies carried out across the Hockai Fault Zone (Ardenne, Belgium) (Lecocq and Camelbeeck, 2016).*

To obtain 3D views of fault zones, pseudo-3D imaging of shallow fault areas, coming from the integration of parallel 2D ERT profiles, has been also used. Fig. 1.4b visualizes in 3D the active normal Geleen fault bordering the Roer Valley graben in northeast Belgium (Vanneste et al., 2008), by 3D inversion of 2D ERT data acquired along 10 shallow resistivity profiles (Fig. 1.4a). The ERT prospecting shows the fault as a broad, near-vertical anomaly characterized by sharp lateral resistivity contrasts, with an associated vertical offset of sediment layers. It is worth noting that this approach is currently preferred to actual 3D resistivity surveys, as fewer electrodes, less data acquisition time and less advanced equipment and data processing software are needed. However, this approach fails in areas with complex geology that cannot be approximated by two-dimensional structures. In this case, as we will see in the next Chapter, unconventional data acquisition geometries have been tested (Vargas et al., 2014) to obtain an effective description of the study area.

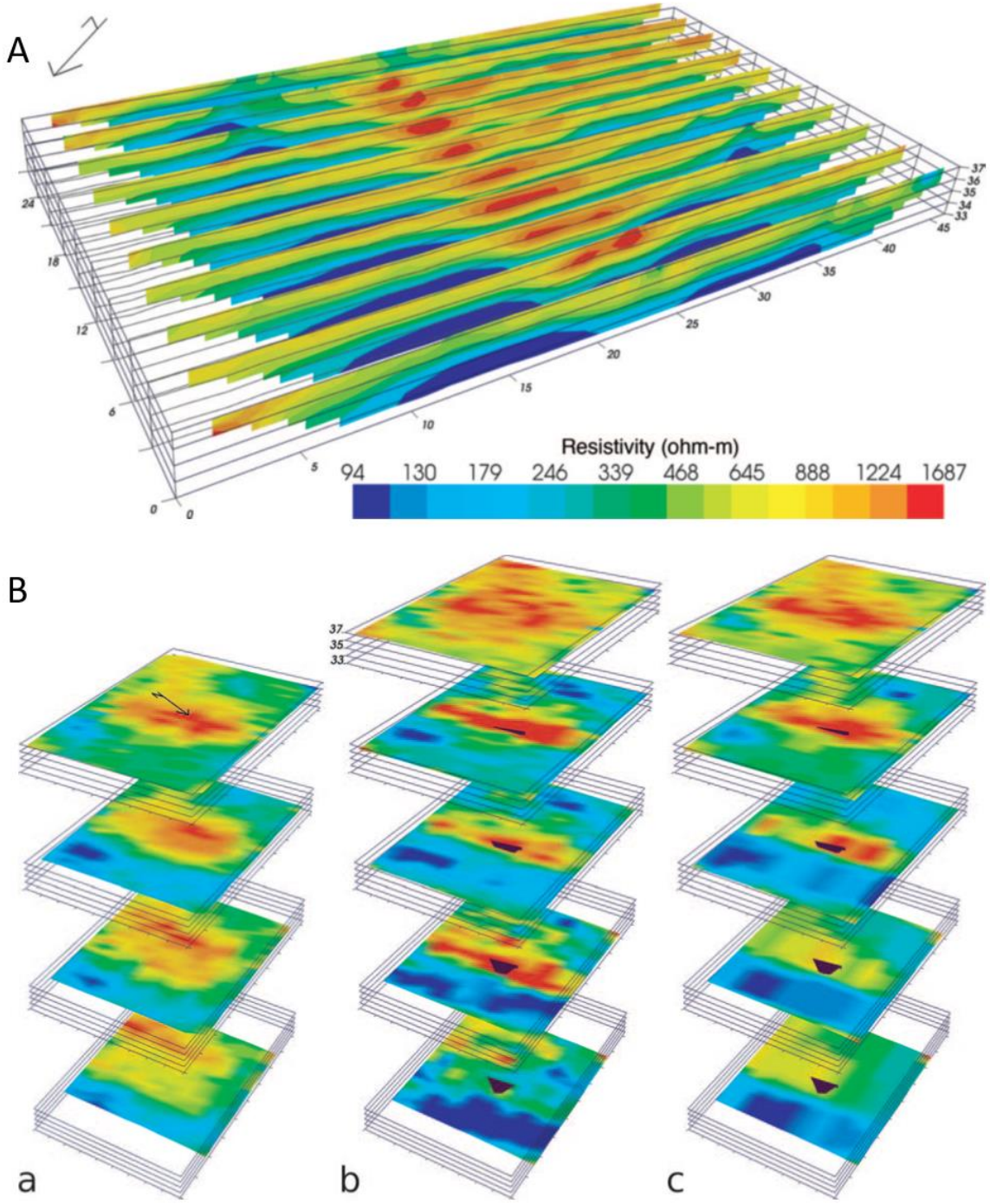

Figure 1.2 *A) Set of ten parallel, shallow resistivity profiles across the Geleen fault (north-east Belgium); B) resistivity maps showing resistivity variations in horizontal slices at different depths across the fault: (a) raw data, (b) normal inversion, (c) robust inversion (modified from Vanneste et al., 2008).*

1.2 Geophysical investigations for identifying CO_2 degassing

In recent years, attention has been focused on the potential impact of the natural release of CO_2 on human health and ecosystems, on the quality of groundwater, on soil mineralogy and CO_2 concentrations in the atmosphere. Therefore, the identification and the geometrical characterization of the CO_2-permeable active faults is fundamental not only for defining the seismic-active zone, but also for understanding the processes governing the flow of fluids along the damage zone of faults that convey the gases towards the surface. Fluid migration along faults can be highly complex and spatially variable, with the potential for channeled flow, accumulation in capped porous units, fault cross-flow, lateral migration along strike, or complete sealing. The presence of CO_2 exhaled by deeper reservoirs may play a dominant role in controlling transport and redistribution of radon towards the earth's surface (e.g. Etiope and Lombardi, 1995; Ciotoli et al., 1999; Yang et al., 2003; Etiope et al., 2005; Yang et al., 2005; Walia et al., 2010). However, the degassing process can be influenced by several factors, e.g. the geological structure within the fault, the sedimentary cover itself, the groundwater level variation, and the meteorological condition (Heinicke et al., 1995; Kemski et al., 1996; Papp et al., 2008).

The geophysical methods most commonly used for studying and monitoring the CO_2 migration along seismically active faults are:

- Seismic tomography: its performance varies significantly depending on reservoir depth, properties and pressure-temperature conditions (McKenna et al., 2003). More specifically, surface 3D seismic data offer the possibility to quantify total amounts of CO_2 in the reservoir and also to identify migration from the storage reservoir into and through the overburden. Moreover, borehole seismic methods, such as cross-hole surveys and vertical seismic profiling (VSP), provide a direct measurement of velocity and signal attenuation (both key indicators of fluid

saturation) providing information complementary to the surface methods (Kikuta et al., 2005). Multicomponent (MC) seismic methods record both the compressional (P-wave) and shear (S-wave) components of the ground motion. By analyzing combined P- and S-wave signals, it is possible to obtain a more complete picture of the fluid behavior, including improved discrimination of fluid pressure and saturation changes and better imaging beneath gas accumulations (Angerer et al., 2001; Wilson and Monea, 2004).

- Gravimetric methods: the opportunity of monitoring CO_2 with repeated gravity measurements is strongly dependent on fluid density and subsurface distribution; the size of the gravity change provides information on subsurface volumes and densities, while gravity spatial variation gives information on lateral CO_2 distribution. Gravimetric surveys have provided valuable independent information capable of reducing uncertainty in the seismic analysis, as shown by Nooner et al. (2006). Nevertheless, the weakest aspect of the gravity data is in resolving absolute depth information on the CO_2 accumulation (Chadwick et al., 2009).
- Electromagnetic and electrical methods: the presence of CO_2 increases the resistivity of the rock system; therefore, these methods are suitable for monitoring storage in salt formations where CO_2 is displacing more conductive formation waters (e.g. Sherlock et al., 2013).
- Acoustic imaging and sonar bathymetry: can provide important shallow monitoring information over large areas above storage sites (e.g. Leighton et al., 2012). They offer the capability of imaging gas escape structures at the seabed.
- Remote sensing: airborne techniques have been used to detect conductivity anomalies associated with hydrogeochemical changes in ground water (e.g. Zhang, 2019). These methods could potentially detect changes in shallow (< 100

m depth) groundwater resistivity due to the presence of dissolved CO_2 (Trautz et al., 2013).

The geophysical signal strength has a strong correlation with CO_2 leakage mass, but not with the brine leakage mass. Both seismic and gravity methods are sensitive to changes in formation density or CO_2 saturation where the CO_2 gas displaces the shallow groundwater and it is trapped below a confining layer. The seismic method is much more sensitive to a small leak than the gravity method. Magnetotelluric (MT) and ERT methods are sensitive to changes in both CO_2 saturation and concentration, resulting from brine leakage and dissolved CO_2. MT has a shallow blind zone (0-50 m) and is less sensitive to near-surface gas-phase CO_2, but it has better resolution and a much larger penetration depth than ERT. Without the near-surface caprock layer, CO_2 gas will leak into the atmosphere and will accumulate less near the ground surface. The smaller accumulations may prevent seismic and gravity sensors from detecting the gas-phase leakage plume, but the CO_2 dissolved in the aqueous phase may be detected by ERT or MT. The bulk electrical resistivity of sedimentary units depends strongly on the pore fluid content and pore connectivity (Gueguen and Palciauskas, 1994).

In the following, applications of electrical and electromagnetic methods for investigating CO_2 degassing are briefly summarized, as these methods are among the best candidates for such studies.

1.2.1 Electromagnetic methods

Electromagnetic (em) sounding methods aim to determine variations in the earth's electrical conductivity with depth. These methods include natural-field methods (magnetotellurics and audiomagnetotellurics), and controlled-source induction methods, as well as high-frequency radiation techniques such as ground-penetrating radar (GPR). Usually they are applied for characterizing and monitoring natural

reservoirs by virtue of their sensitivity to changes in the physical properties of the reservoir (electrical conductors in the case of aquifers and resistors in the case of hydrocarbons). In the case of CO_2 injection into salt formations, laboratory measurements demonstrate that there will be large increases in resistivity by two or more orders of magnitude, as the salt fluids are displaced by CO_2 (Fig. 1.8).

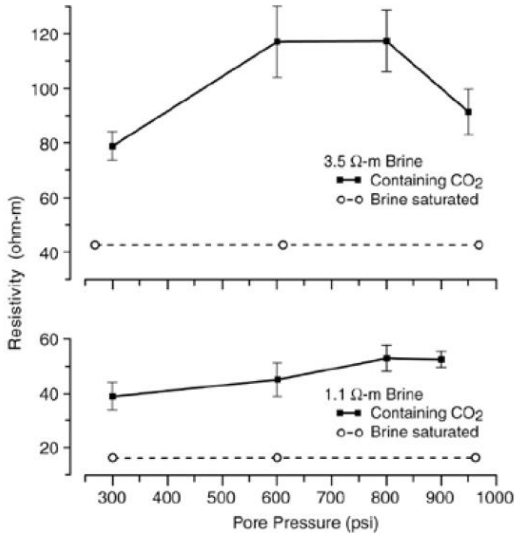

Figure 1.3 *Changes in resistivity of brine-filled rock formations with variable saline content when CO_2 is injected into them (Myer, 2001).*

Such changes are observable on the surface using appropriately designed em surveys, either using natural or controlled sources. The MT technique is sensitive to interconnected fluid network and can image these zones at crustal and upper mantle scales. Low resistivities in the lower crust and upper mantle can reflect zones of aqueous fluids, partial melts and/or mineralization due to fluid-driven chemical precipitation reactions. MT is not able to distinguish unambiguously between conductive fluids and other conductive phases at depth. Regardless of the conductive phase, however, the high conductivity must have long-range interconnections to be visible with MT measurements. For example, magnetotelluric studies at the San Andreas Fault Zone (Fig. 1.9), and at many other active and fossil

tectonic systems (e.g. Becken and Ritter, 2012), imaged electrical conductivity anomalies on various crustal and upper mantle scales, which seem closely related to active or ancient tectonic processes. Many of the high-conductivity anomalies associated with active tectonic settings are interpreted with saline or hydrothermal aqueous fluids residing in interconnected porosity networks.

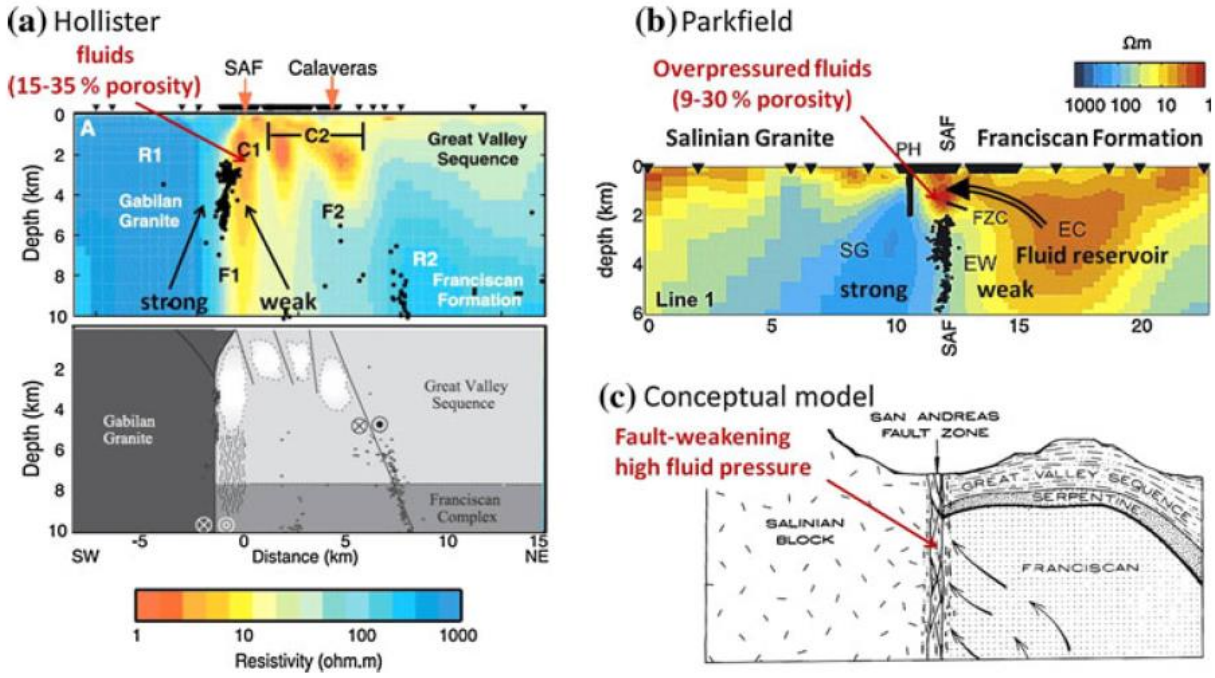

Figure 1.4 *Upper crustal resistivity models obtained from 2D inversion of MT data (a) near Hollister and (b) near Parkfield (Becken and Ritter, 2012).*

Furthermore, numerous studies have proven the effectiveness of electromagnetic methods in CO_2 monitoring at small and medium scale (e.g. Pettinelli et al., 2010; Bergmann et al., 2012; Carrigan et al., 2013; Hovorka et al., 2013). In particular, Pettinelli et al. (2010) have compared the use of various em methods to characterize a CO_2 gas vent located in the extinct Latera caldera (central Italy). Fig. 1.10 shows their results from GPR and frequency-domain electromagnetic (FDEM) techniques, which seem clearly identify the geometrical structure of the vent and suggest an anomaly alignment (NNW-SSE) associated with the main fault.

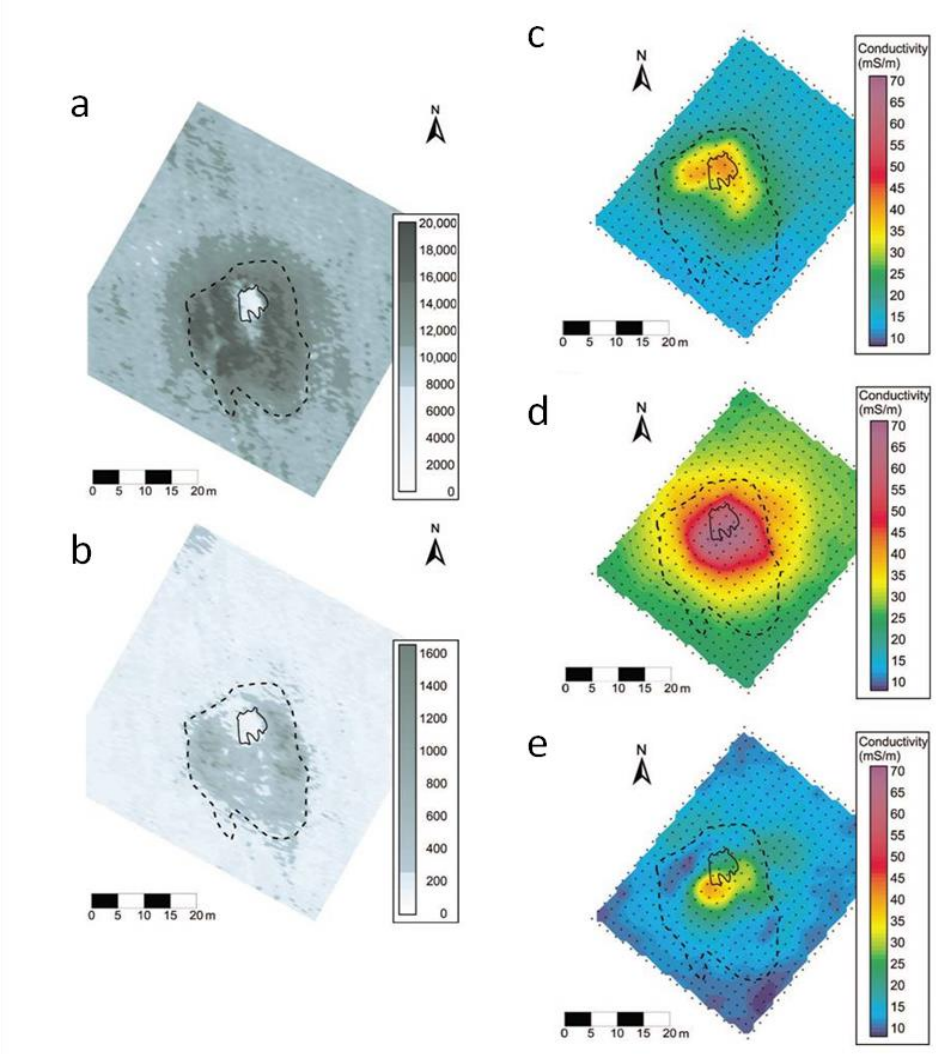

Figure 1.5 *Left panels: maps showing 0–5 ns (a) and 10–40 ns (b) time slices of the GPR grid data. Right panels: FDEM results collected over the gas vent. (c) Horizontal configuration for an integrated depth interval of 0–3 m; (d) vertical configuration for an integrated depth interval of 0–6 m; and (e) differential between (c) and (d) for an estimate of the 3–6-m depth interval (modified from Pettinelli et al., 2010).*

1.2.2 ERT

Geoelectrical methodologies allow to define the geometry of faults in the shallowest layers, identifying potential drilling sites for paleoseismology studies and detecting buried tectonic structures, including folded layers and abrupt changes in the thickness of sediments (Suzuki et al., 2000; McBride, 2003). In all these cases, the use of electrical resistivity measurements is promising, given that the rock electrical properties are more sensitive to the presence of fluids than the elastic properties

(Ramirez et al., 1993; Carcione et al., 2007; Nakatsuka et al., 2009; Carcione et al., 2012). The effectiveness of resistivity measurements for quantifying and monitoring CO_2 flows in geological formations depends by the strong relationships between the electrical resistivity and the same factors that are relevant for the CO_2 storage in water (i.e. water saturation, type and concentration of ions present in the fluid, pH, cation exchange capacity of minerals, and temperature). In fact, as a result of these dependencies, high-resolution electrical resistivity tomographies have been successfully used both for the physical characterization of the site and for monitoring the migration in the subsoil of various fluids including flooding of underground steams, leakage of underground reservoirs, water infiltration and contaminant movement (e.g. Daily et al., 1992; Ramirez et al., 1993; Newmark et al., 1996; Daily et al., 1998; LaBrecque et al., 1998; Newmark et al., 1998). As it concerns CO_2 degassing phenomena, Byrdina et al. (2009) observed high-resistivity anomalies in a tectonically active area of central Nepal (south Asia), likely related to the permeable fracture zone that serves as a preferential route for gases and water (blue ellipse in Fig. 1.11). Conversely, Pettinelli et al. (2010) identified preferential gas rising zones as conductive anomalies in the extinct Latera caldera (central Italy) (Fig. 1.12).

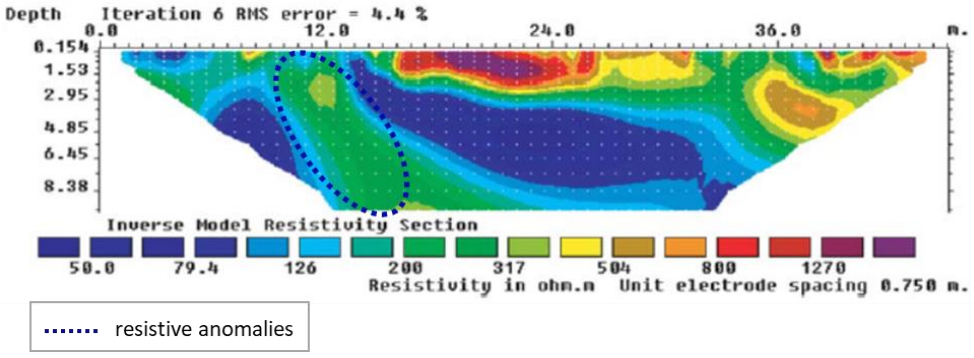

Figure 1.11 *Inverse resistivity model coming from an ERT profile located around hot springs in a tectonically active area of central Nepal (south Asia). The model shows a high-resistivity pattern (blue ellipse) centred on the gas vent and surrounded by moderately resistive sediments (modified from Byrdina et al., 2009).*

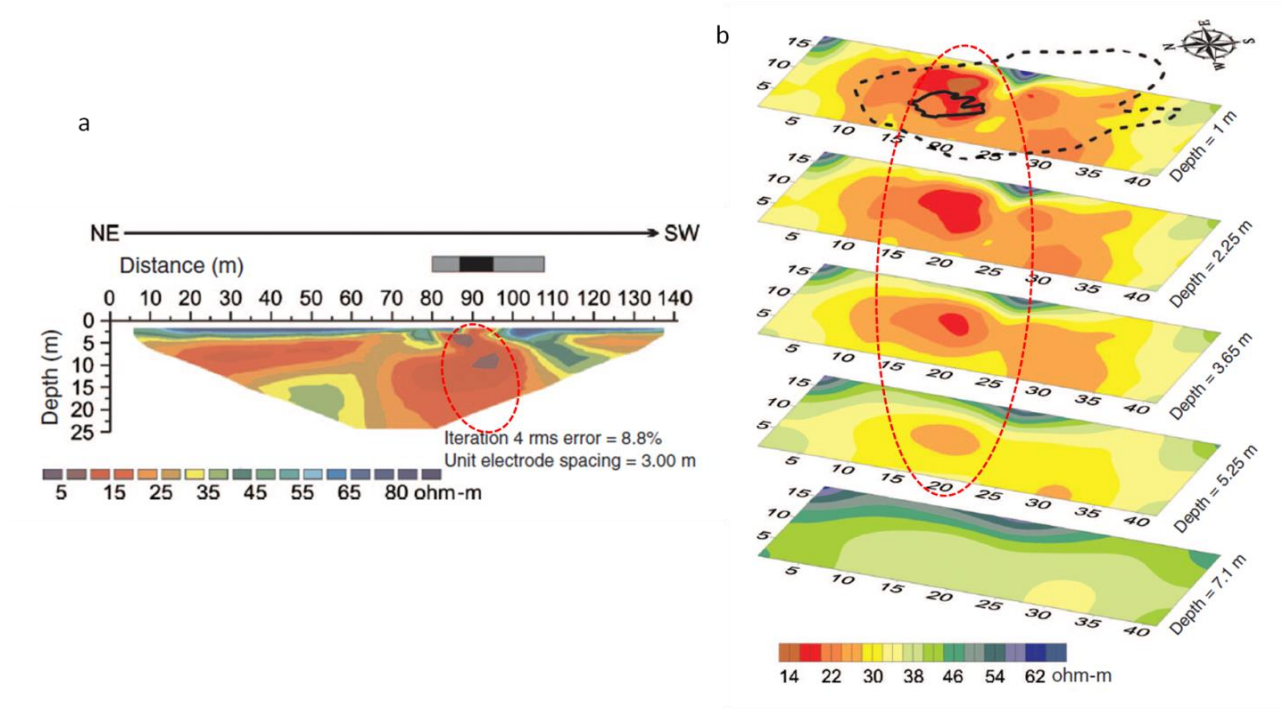

Figure 1.12 *(a) Inverse resistivity model coming from a NE-SW ERT profile crossing the FDEM survey area in Fig. 1.10. It shows a strong conductive area centred on the gas vent (red ellipse), dipping southward and increasing in dimension with depth, surrounded by moderately conductive sediments. (b) Series of horizontal-resistivity slices at different depths that show the results of the 3D ERT survey conducted almost entirely within the zone of influence of the gas vent. The strong conductive area (red ellipse) corresponds to the one centered on the gas vent shown in (a) (modified from Pettinelli et al., 2010).*

These results suggest that the preferential gas rising pathways can be highlighted in terms of conductive or resistive anomalies based on the geological setting and the chemical and biological environment of the investigated area (Arts et al., 2009; Byrdina et al., 2009).

Moreover, recent studies (Christensen et al., 2006; AlHagrey et al., 2010; Kiessling et al., 2010; Schmidt-Hattenberger et al., 2011; Bergmann et al., 2012) have shown that high-resolution electrical tomograms are efficient tools for detecting gas inside a conductive fluid and, more specifically, for highlighting resistivity changes caused by CO_2 migration in geological basins. In these geological settings, the interpretation is more complicated when attempts are made to detect the possible migration of CO_2 in the sedimentary coverings of geothermal reservoirs, which may be due to

faults and fractures or old damaged wells. The difficulty, in such cases, is that the host rock has a harder matrix and a lower porosity and permeability than the hosted materials. Furthermore, CO_2 can be present in the supercritical state, with a density and a mass modulus much higher than those of the gas phase (Picotti et al., 2012). Therefore, the fluid effect is lower than that observed in a softer and more permeable rock due to the reduced mobility of the fluid. To overcome these limitations, the indirect approach adopted in this PhD research project involves the use of high-resolution 3D electrical resistivity tomography surveys, in order to produce an accurate 3D representation of the physical state of the investigated subsurface volume, in terms of electrical resistivity value distribution that allows the identification of preferential CO_2 migration paths, whose dimensional complexity cannot be solved using 2D or 2.5D data acquisition techniques. To achieve this objective, the present PhD project aims to develop a new and more versatile 3D ERT data acquisition technique through the use of unconventional data acquisition geometries, which are able to overcome any logistical constraints. The proposed approach takes advantage from the results of its applications to small-scale engineering and geotechnical targets (e.g. cavity research, soil stabilization) (Dahlin et al., 1999; Schueremans et al., 2003; Farooq et al., 2007, Fischanger et al., 2007; Rittgers et al., 2010).

Chapter 2.

A non-conventional 3D ERT as a powerful tool for 3D characterization of complex geological structures

2.1 3D Electrical Resistivity Tomography (ERT) technique

Direct current (DC) electrical resistivity technique is one of the oldest and most commonly used geophysical exploration methods aimed at estimating the electrical resistivity of the subsurface (see standard textbooks on the subject, for example: Parasnis, 1986; Telford et al., 1990; Reynolds, 2011). Electrical resistivity, ρ, (or its inverse, electrical conductivity, σ) is an intrinsic electrical property of a material that measures its ability to resist an electrical current flow. The latter is governed by the well-known Ohm's law, which is written as:

$$\boldsymbol{J} = \frac{1}{\rho}\boldsymbol{E} ,$$

where ρ is the electrical resistivity of the medium, $\boldsymbol{J}$ is the current density and $\boldsymbol{E}$ is the electric field. In practice, the electric potential V is measured, which is linked to the electric field by the following equation:

$$\boldsymbol{E} = -\nabla V .$$

The electric potential is a function of three different conduction mechanisms: electronic, electrolytic and dielectric. Since most of the earth materials are insulators, the main conduction is of electrolytic type, i.e. current flows by ions in the fluids permeating porous and/or fractured soils and rocks. This means that the resistivity parameter is strongly affected by porosity, ground water content and percentage of dissolved salts (e.g., Sumner, 1976; Sharma, 1997).

In practice, for a semi-infinite homogeneous and isotropic medium, which is the simplest Earth model, the DC electrical resistivity measurements are performed by

injecting a direct current, *I*, through a pair of electrodes (current electrodes) placed on the land surface and measuring the resulting electrical voltage, ΔV, by using another two electrodes (potential electrodes), also placed on the surface. The electrical resistivity, ρ, is then calculated based on the mutual distance between the four electrodes, the electrical current injected into the ground, and the measured electrical potential difference:

$$\rho = K\frac{\Delta V}{I},$$

where *K* is the so-called geometric coefficient depending on the electrode configuration (e.g., Reynolds, 2011). For non-homogeneous soils, the above equation defines an apparent resistivity value that is a function of the geometry of the electrode array and the true resistivities and other characteristics of the subsurface materials, such as layer thicknesses, angles of dip, anisotropic properties, traversed by the electric current flow.

In the last few decades, due to significant progresses in instrumentation and data acquisition, processing and interpretation procedures, the electrical resistivity tomography (ERT), in 2D or 3D configuration, is among the most widely used techniques for DC electrical resistivity measurements in the field of the geophysical prospecting, as it allows very high-resolution imaging of the electrical properties of the subsurface (e.g., Revil et al., 2012; Loke et al., 2013). The 2D (or 3D) ERT prospecting is usually realized by using an array of electrodes disposed along a profile (or an area) that allows the estimation of a large number of resistivity values at different depths along the investigated profile (or area) to produce a very detailed image of the subsoil in terms of an apparent resistivity pseudosection (or pseudovolume). The latter enables a qualitative estimation of the electrical behaviour of the medium but does not provide the true resistivity and shapes of the of the different materials/structures present in the subsurface. Each acquired value, indeed, corresponds to a volumetric measurement, closely dependent on the type

of electrode array configuration, that is plotted against a pseudodepth. Thus, the apparent resistivity value distribution in a pseudo-section (or pseudo-volume) distorts the real subsurface picture. The subsequent inversion process of the observed apparent data permits to retrieve the true resistivity distribution in the underground, which is useful to define geometry and nature of subsurface targets, such as soil/bedrock interface, strata thickness, or depth and width of anomalous zones (e.g., Chambers et al., 2012; Kumar, 2012; Di Maio et al., 2015c).

Due to the nonlinear behaviour of the inverse problem for electromagnetic fields, the solutions are computed following iterative procedures (Daily and Owen, 1991; LaBrecque et al., 1996) that involves a simultaneous use of numerical modeling algorithms, based on Finite Elements (or Finite Differences) methods, and data optimization techniques, based on minimum squares procedures. In such an approach, the *forward model* (simulation of electric field for a given resistivity distribution using a discrete domain) is recurrently solved while changing the subsurface electrical properties. For the inversion of the 2D (or 3D) ERT data the most common and widely used inversion algorithm is that used by the Res2Dinv (or Res3Dinv) software (Loke and Barker, 1996; Loke et al., 2003). It is based on a smoothness-constrained least-squares method which allows to obtain two- or three-dimensional models through finite differences or finite elements computations, considering also the topographic corrections. To evaluate the fit of the obtained resistivity model, the root means square error (RMS) is considered, which provides the percentage difference between measured and calculated data.

The 3D inversion approach adopted for the present study and implemented by the ERT-Lab_64™ software (produced by Geostudi Astier Srl, Livorno, Italy, and Multi-Phase Technologies LLC, Nevada, USA) makes use of the Occam's regularization proposed by Constable et al. (1987) and further developed by Morelli and LaBrecque (1996) for the optimal management of noisy data. The iterative

procedure needs an initial guess, generally given by the homogeneous half-space derived from the statistical analysis of the acquired apparent resistivity values.

As it is well known, there are many advantages in performing 3D ERT surveys substantially linked to the high density of the acquired resistivity data, which significantly increases resolution and accuracy in defining the investigated buried volumes. Moreover, thanks to the possibility of extracting from the entire investigated volume horizontal and/or vertical resistivity plans with different orientation, as well as resistivity envelopes, the three-dimensional features of buried structures and/or fluid migration paths in active dynamics areas can be described with greater detail and effectiveness than those provided by 2D or 2.5D approaches. In fact, a 3D survey overcomes the lack of data between 2D lines, which occurs when the 2D ERT technique along parallel profiles is used, as well as it reduces the errors deriving from data interpolation when the 2.5D approach is adopted, which consists of 3D inversion of resistivity data acquired by 2D ERT surveys.

The traditional approach to the 3D ERT surveying usually requires that the electrodes are positioned in a square or rectangular grid keeping the distance between adjacent electrodes constant in the x and y directions (see par. 2.1.1). These electrode dispositions are difficult to realize in geological contexts where strong topographic variation, dense vegetation, rough terrain around landslide areas are present. To overcome these problems and reduce costs, advanced 3D ERT data acquisition techniques, that use unconventional electrode geometries, have been recently applied only in engineering and archaeological contexts. The application and optimization of these un-standard techniques in the geological field, through the creation and testing of ad hoc data acquisition sequences, constitutes the new approach proposed in this PhD thesis for the 3D characterization of complex geological structures (see par. 2.1.2).

In the following, after illustrating traditional and unconventional techniques, a comparison between the results of applying both approaches in the same test area is presented. Finally, the use of the proposed unconventional approach in different fields of geophysics is discussed.

2.1.1 Traditional approach

The electric resistivity tomography technique can be performed to define 2D, 2.5D or 3D models of the subsurface (e.g. Drahor et al., 2007; Chambers et al., 2011; Di Maio and Piegari, 2012; Di Maio et al., 2016). However, dense electrode arrays are required to ensure user-readable high resolution (HR) images. Since all geological structures in nature are mainly 3D, in theory a 3D resistivity survey, which uses a 3D interpretation model, should provide the most accurate results. However, it is not routinely used like 2D surveys, essentially due to the costs of the 3D technique that is comparatively higher than 2D for large investigation areas.

The choice of the electrode configuration is crucial to determine the output resolution and depth of investigation as well as the survey cost, being some configurations very time-consuming. The dipole-dipole, pole-pole and pole-dipole arrays are frequently used for 3D surveys (Loke and Barker, 1999), since other arrays have a poorer data coverage near the edges of the survey grid. The dipole-dipole array is recommended only for grids which are larger than 12 by 12 due to the poorer horizontal data coverage at the grid sides. The main problem that is likely to be faced with this array is the comparatively low signal strength. In this research work, all 3D ERT acquisitions were made using a pole-dipole array (Fig. 2.1), which is suitable for surveys with medium and large detection grids (12 by 12 and above). It has a better resolving power than the pole-pole array (Sasaki, 1992), and is less susceptible to telluric noise since both potential electrodes are kept within the survey grid. Compared to the dipole-dipole array, the pole-dipole configuration has

a significantly stronger signal strength, and, although it has one *remote electrode* (C2 *current electrode* in Fig. 2.1), the effect of this electrode on the measurements is much smaller compared to the pole-pole array. Since the pole-dipole array is an asymmetric array (Fig. 2.1a), all measurements with this device are generally carried out with an arrangement of the pole perpendicular with respect to the position of the *potential electrodes* (P1 and P2 in Fig. 2.1b).

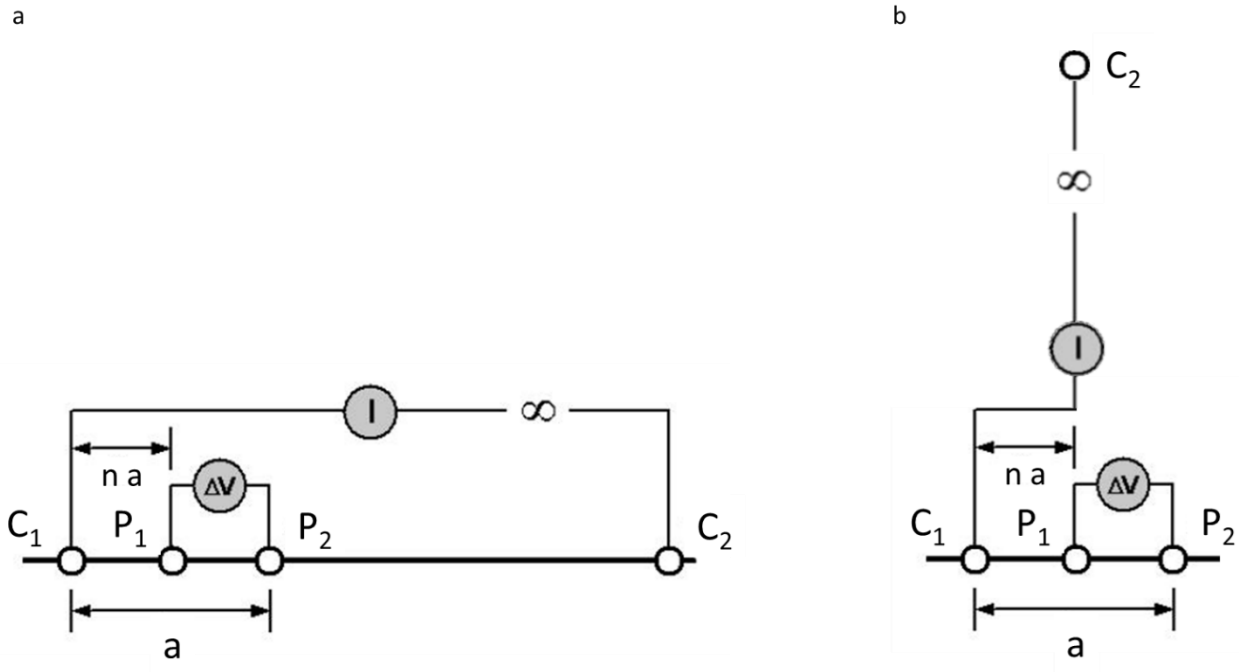

Figure 2.1 *The pole-dipole array: a) conventional pole-dipole array; b) pole-dipole array with an arrangement of the pole perpendicular with respect to the position of the* potential electrodes *(modified from Knödel et al., 2007).*

The electrodes for 3D surveys are normally arranged in a rectangular grid with a constant spacing between the electrodes. Fig. 2.2 shows a possible arrangement of the electrodes for a 3D survey using a system with 25 electrodes.

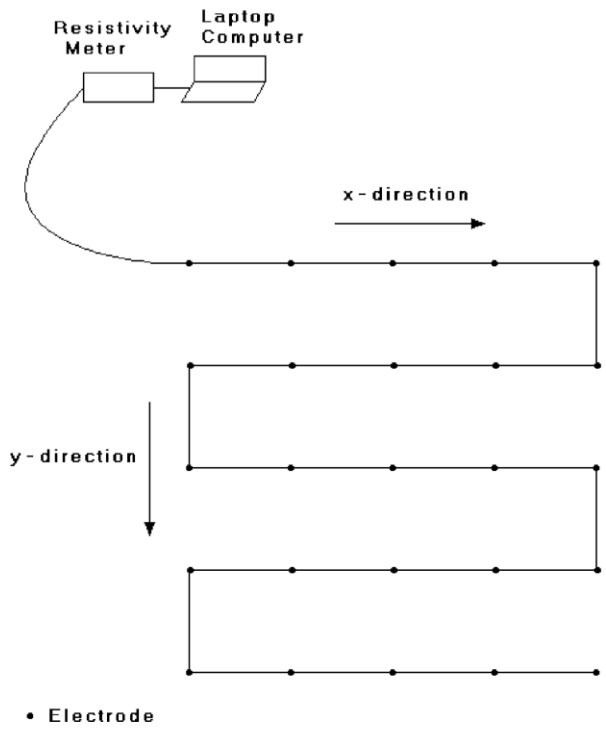

Figure 2.2 *The arrangement of the electrodes for a 3D ERT conventional survey (from Loke and Barker, 1999).*

In particular, for the pole-dipole electrode configuration the maximum number of independent measurements, n_{max}, that can be collected is given by $n_{max} = n_e(n_e - 1)/2$, where n_e is the number of electrodes. In this case, each electrode is in turn used as a current electrode and the potentials at all the other electrodes are measured. It is worth noting that because of reciprocity, it is only necessary to measure the potentials at the electrodes with a higher index number than the current electrode in Fig. 2.3a. It follows that for a 5x5 electrode grid, there are 300 possible measurements. For 7x7 and 10x10 electrode grids, the complete data set consists of 1176 and 4500 measurements, respectively, which can be very time-consuming (at least several hours). To reduce the number of measurements without seriously compromising the quality of the obtained model, the traditional 3D ERT approach involves the use of an alternative measurement sequence shown in Figure 2.3b, known as "cross-diagonal survey" technique. In this case, the potential is measured only at the electrodes along the x-direction, the y-direction and the 45° diagonal

lines passing through the current electrode. For a 7x7 grid, the number of measurements acquired by this arrangement is reduced to 476, which is about one-third of that required by a complete data set survey (Loke and Barker, 1996b).

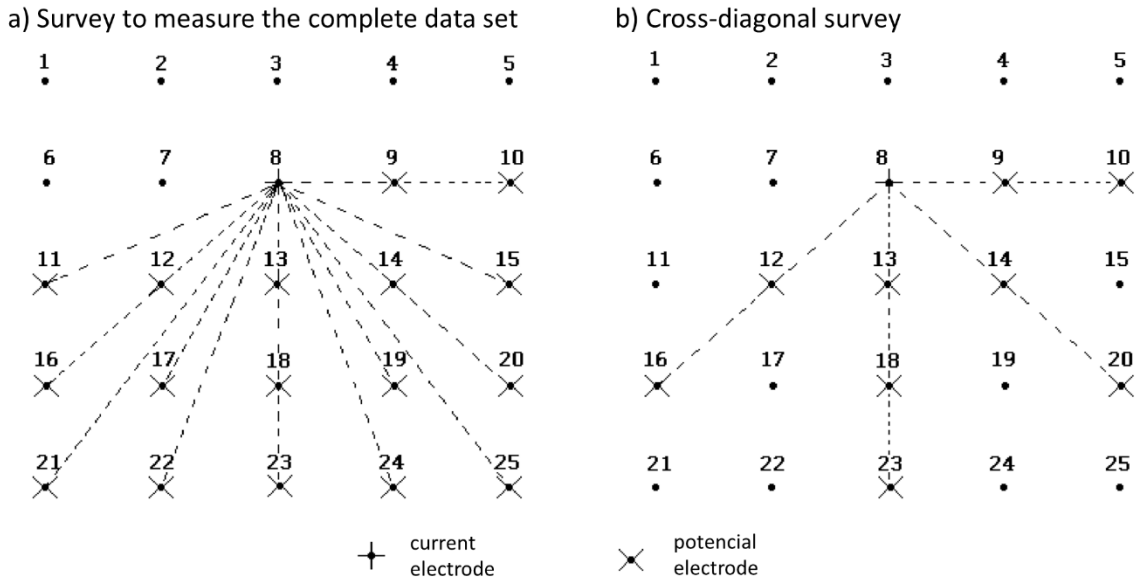

Figure 2.3 *Location of potential electrodes corresponding to a single current electrode in the arrangement used by (a) a survey to measure the complete data set and (b) a cross-diagonal survey (modified from Loke and Barker, 1999).*

However, for most 3D surveys aimed at both commercial and research purposes, grids formed by a number of electrodes lower than 10x10 have a poor use due to the small size of the area that in this case would be investigated. The latter is usually limited in size by the number of electrodes that can be managed by the modern georesistivimeters, generally equal to 48, 72 or 96, thus allowing high-resolution investigations only for the shallowest portions of the subsurface.

Summarizing, the main disadvantage of conventional 3D ERT data acquisition techniques is linked to the configuration of the electrodes, which must be arranged on the earth surface according to a regular 2D mesh. Such a requirement is often impractical both for logistical problems related to the characteristics of the survey areas (e.g. areas with complex topography) and for the limited extent of the area that can be investigated (Table 2.1) and, consequently, for the maximum exploration

depth that can be achieved. This explains the wide use of 2D ERT surveys along parallel profiles in many application fields, and the use of 3D data inversion techniques to interpret jointly the 2D ERT profiles, which is only practicable when the profiles are positioned at distances comparable with the interelectrode distance (2.5D approach).

Source	Location	Domain (m)	Dim. of acquisition/ processing	# Lines	# Electrode	Electrode spacing (m)	# Data	Array type	Acquisition channels
Park and Van (1991)	Nevada	200×200	3D grid/3D	–	25	50	300	PP	1
Loke and Barker (1996)	UK	7×7	3D grid/3D	–	50	0.5	476	PP	1
Chambers et al. (1999)	UK	95×95	2D orthogonal/3D	20	400	5	6927	PD	4
Bernstone et al. (2000)	Sweden	50×160	2D parallel/2D	6	440	2	–	Wenner	4
Jackson et al. (2001)	UK	20×10	3D grid/3D	–	200	1	4177	PD	–
Yi et al. (2001)	Korea	400×460	3D grid/3D	–	296	20	7952	Mod. PP and DD	–
Chambers et al. (2001)	UK	8×12	2D orthogonal/3D	37	404	0.5	8098	DD and Wenner	4
Dahlin et al. (2002)	Sweden	100×80	3D roll-along/3D	–	357	5	3840	PP	4
Ogilvy et al. (2002)	UK	175×190	2D parallel/3D	19 (area 1)	380	5	–	PD	–
Bentley and Gharibi (2004)	Canada	28×28	2D orthogonal/3D	16	432	1	–	DD	1
Nyquist and Roth (2005)	New Jersey	81×81	2D orthogonal/3D	56	784	3	10,583	DD	8
Gunther et al. (2006)	Germany	200×70	2D orthogonal/3D	14	577	1	4245	Wenner	–
Friedel et al. (2006)	Switzerland	25×25	2D orthogonal/3D	17	850	0.5	1466	Sch and DD	1
Chambers et al. (2006)	Scotland	155×210	2D orthogonal/3D	29	652	5	7300	Wenner and Sch	4
Mansoor and Slater (2007)	New Jersey	95×105	2D orthogonal/3D	20	1310	1.5	13,000	Mod. Wenner	10
Chambers et al. (2007)	UK	50×31	2D orthogonal/3D	29	1200	1	12,700	DD	8
Rucker et al. (2009)	Washington	850×550	2D orthogonal/3D	47	7035	3	118,165	PP	8

PP = pole–pole; PD = pole–dipole; DD = dipole–dipole; Sch = Schlumberger.

Table 2.1 *Examples from literature of three-dimensional electrical resistivity surveys that show the generally small dimension of the investigated area (from Rucker et al., 2009).*

2.1.2 A new proposal

To overcome the problems described above, different unconventional electrode configurations have been proposed.

In archaeological contexts, where sometimes the target is itself an obstacle, special geometry designs, such as circle, triangle and horseshoe (Fig. 2.4), have been developed to obtain appropriate geophysical information beneath the study area. Figs. 2.5 and 2.6 show some examples of 3D ERT applications for archaeological purposes. In particular, Fig. 2.5 illustrates the results obtained for the study of a pre-Hispanic circular pyramid (Cuicuilco, Mexico City) using a circular electrode array (Vargas et al., 2014), while Fig. 2.6 shows the interior imaging of El Castillo Pyramid (Chichen Itza, Mexico) provided by a 3D ERT survey performed using electrodes

distributions on each body of the pyramid, which consists of 9 levels (pyramidal bodies), plus a tenth level that corresponds to the ground level (Chávez et al., 2017).

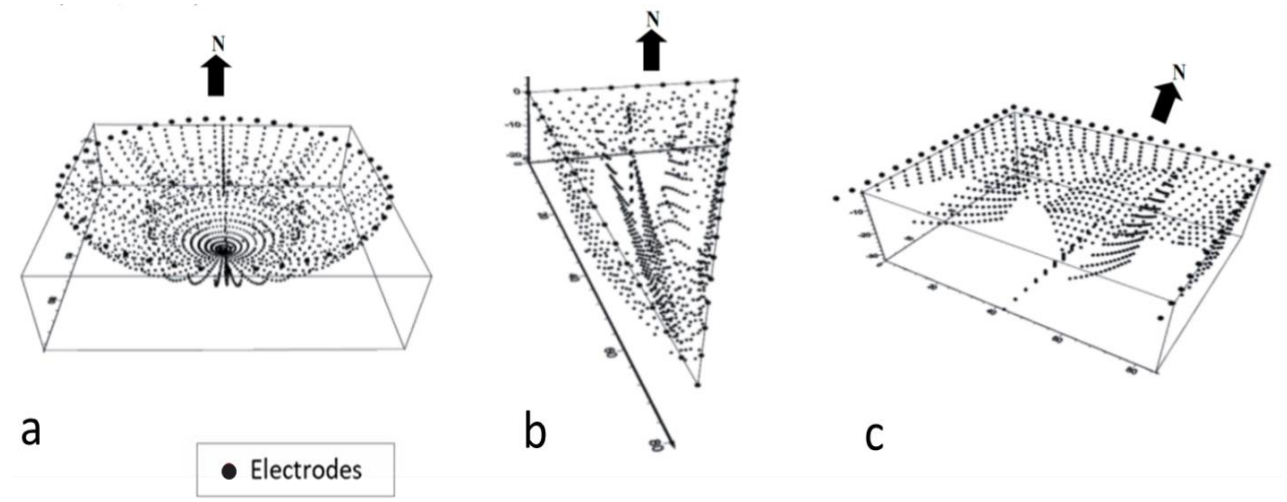

Figure 2.4 *Unconventional electrode arrays used for 3D ERT surveys in archaeological areas. The dots correspond to the apparent resistivities measured in depth using circle (a), triangle (b) and horseshoe (C) electrode configurations (modified from Vargas et al., 2014).*

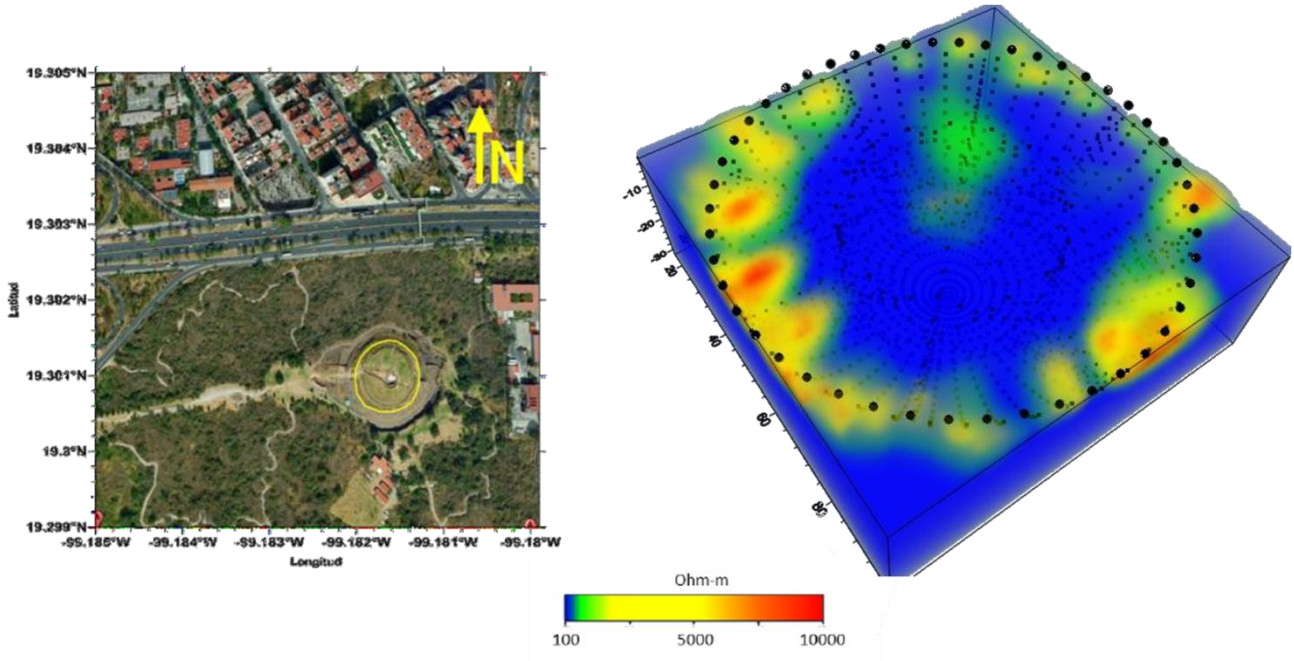

Figure 2.5 *Inverted solution of the 3D ERT data (right panel) obtained for the circular array applied in the Pyramid of Cuicuilco, southern portion of Mexico City (left panel) (modified from Vargas et al., 2014).*

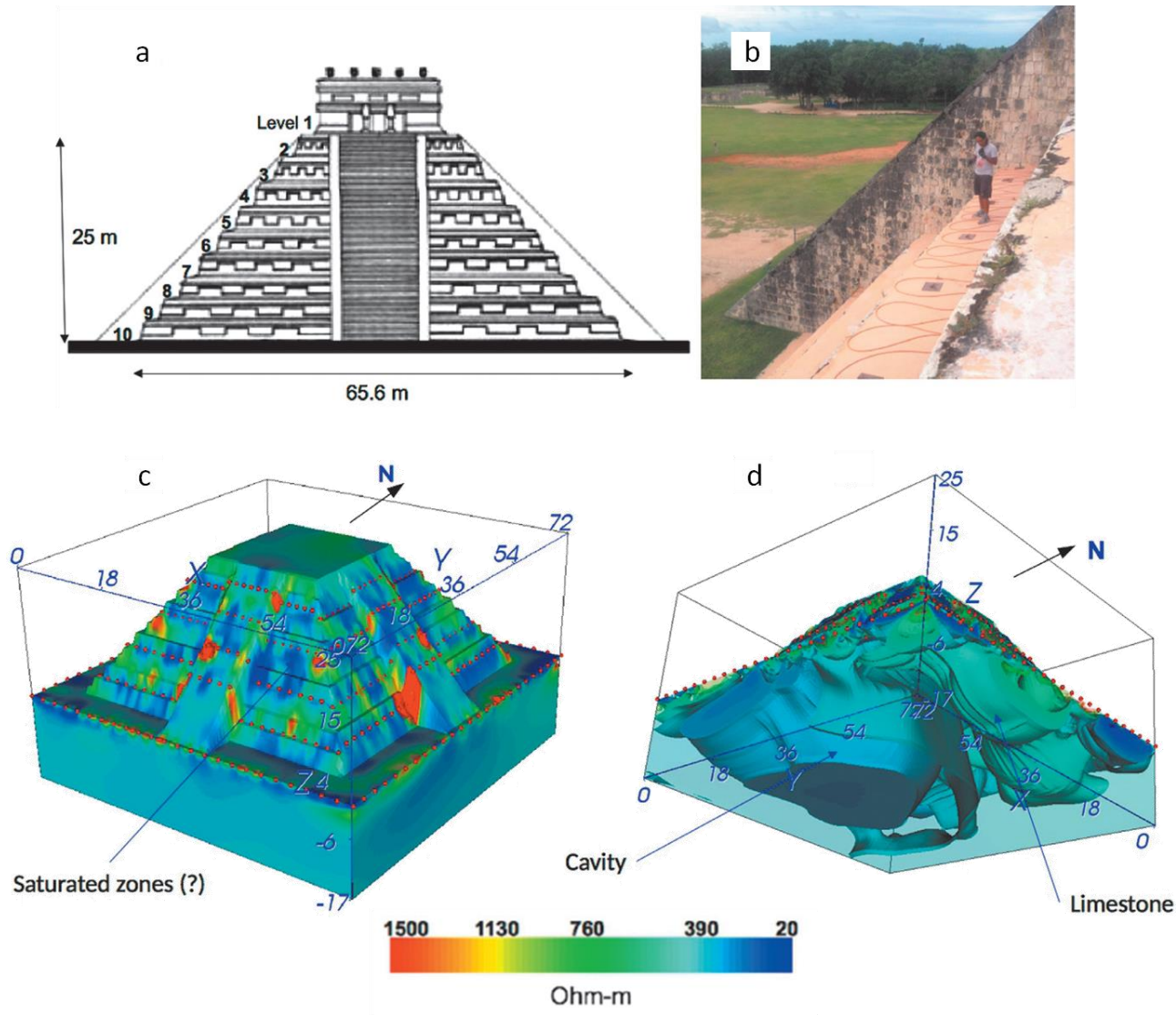

Figure 2.6 (a) Schematic depiction of the dimensions of El Castillo pyramid (Chichen Itza, Mexico) and the 10 bodies that make up this pre-Hispanic building. Electrodes position are shown as red dots. (b) Position of the electrodes deployed on each body. (c) Side view of the southern and western faces of El Castillo pyramid. The effects of the stairs are shown in red, while possible saturated zones are shown in blue. (d) Geometry of the cavity partially filled with water observing the model from its bottom part (modified from Chàvez et al., 2017).

For engineering applications, the most commonly used non-conventional acquisition geometries consist of L-, anular-, snake-shaped configurations (Fig. 2.7), whose parallel branches, unlike those used in conventional 2.5D geometries, are positioned at a distance that does not depend on the interelectrode distance.

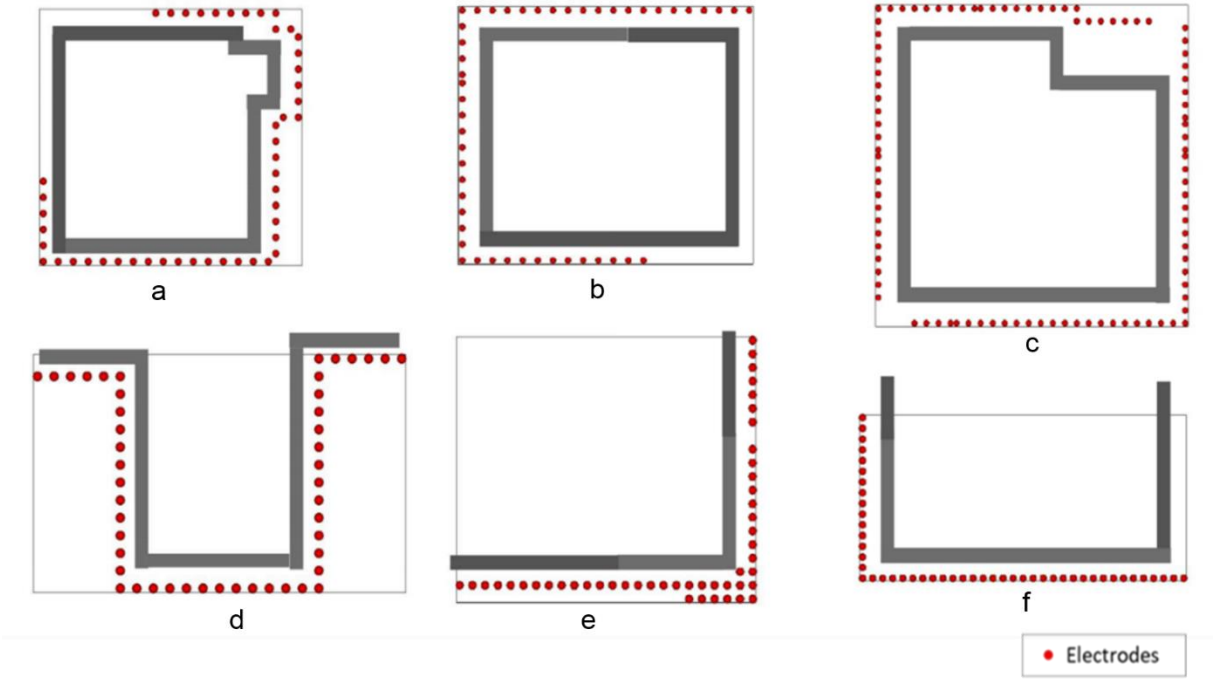

Figure 2.7 *Examples of non-conventional acquisition geometries for 3D ERT surveys: irregular geometry (a, c, e); C-shaped (b) and L-shaped (f) configurations.*

The innovation proposed in this research work consists in having tested and optimized this type of electrode layout for specific geological contexts, making it a powerful new tool for the 3D characterization of geological structures with complex geometries.

The innovative 3D acquisition scheme adopted is based on a sequence of measures designed ad hoc, which allows to use the electrodes of each multi-electrode cable both as transmission and as measuring devices. This means that the position of the transmitting (TX) and receiving (RX) dipoles is continuously modified to obtain a uniform coverage along the measurement profiles and along all three spatial directions. To obtain the optimal 3D acquisition configuration for each test area, the ERT-Lab sequencer software (ERT-Lab software tool, Fig. 2.8) was used, which allows, unlike the commonly used software, the setting of complex acquisition geometries.

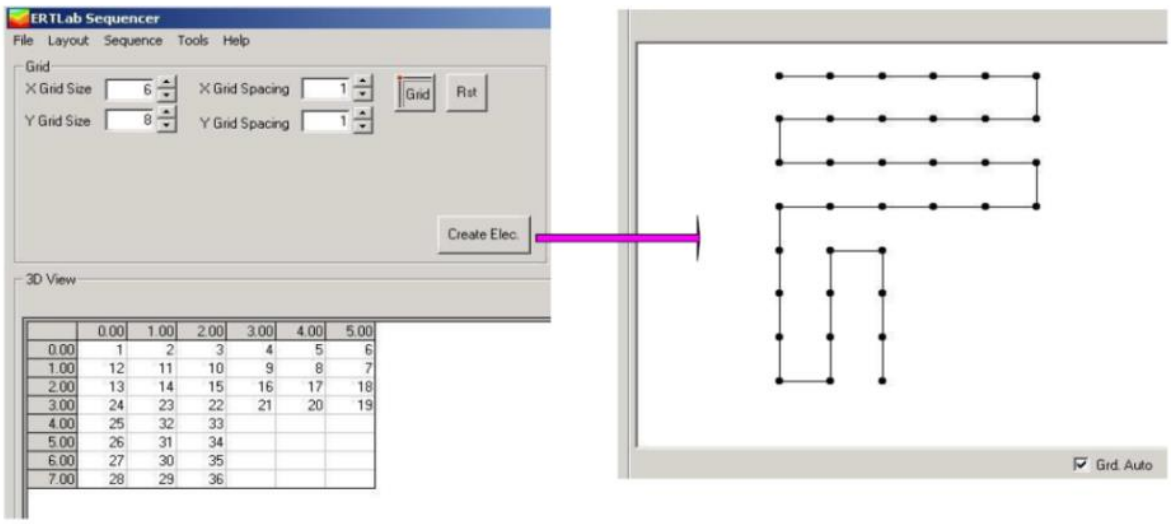

Figure 2.8 *Example of setting the geometry of geoelectric data acquisition sequences using the ERT-Lab Sequencer software (by GeoStudi Astier, Livorno). In particular it is possible to set, in addition to the interelectrode distance, the coordinate (x, y) of each electrode in order to create an acquisition sequence for any chosen unconventional geometry.*

Different data acquisition sequences were generated by testing different acquisition parameters. In Fig. 2.9, the used Sequencer parameters are shown: setting of the Polo-Dipole array (1 in Fig. 2.9); opening of the transmitting (TX)/receiver (RX) dipole (2 in Fig.2.9); quadripole direction (TX-RX along x, y, diagonal 1 and diagonal 2) (3 in Fig. 2.9); TX and RX position along the same cable or along different cables (4 in Fig. 2.9); depth and distance levels between the TX and RX dipoles (respectively, 5a and 6 in Fig. 2.9), which constrain the generation of the quadripoles to the geometric factor *K* (5b in Fig. 2.9).

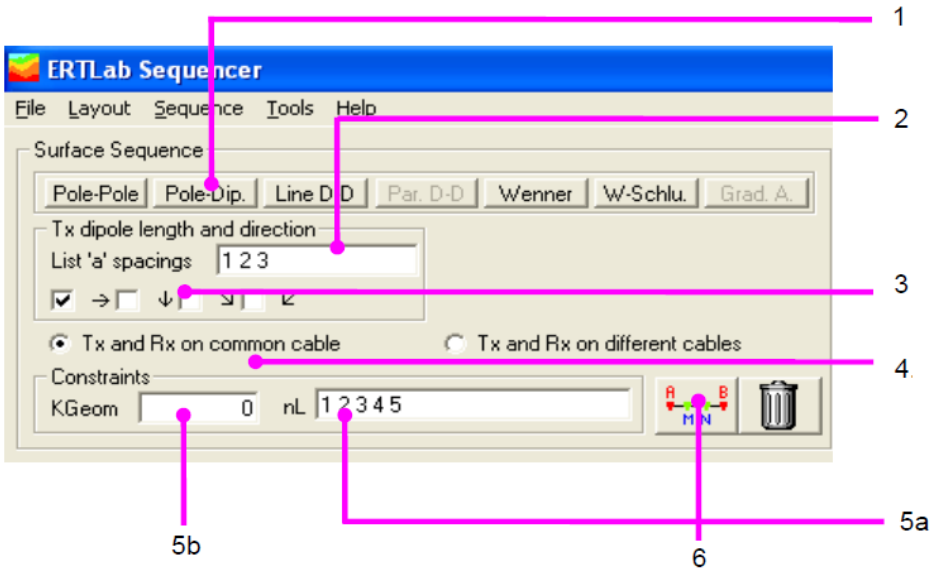

Figure 2.9 *Setting of the parameters related to the transmitting (TX) and receiver (RX) dipoles for the geoelectric data acquisition (by ERT-Lab Sequencer Software, GeoStudi Astier, Livorno). 1: setting of the Polo-Dipole array; 2: opening of the transmitting (TX)/receiver (RX) dipole; 3: quadripole direction (TX-RX along x, y, diagonal 1 and diagonal 2); 4: TX and RX position along the same cable or along different cables; 5 and 6: depth and distance levels, respectively, between the TX and RX dipoles.*

2.1.3 Traditional vs non-conventional approach

The proposed 3D ERT acquisition technique has been validated by comparing the results of its application in the test area shown in Fig. 2.10 with those coming from a standard 3D configuration of the electrodes disposed in the same site. In order to guarantee a comparison between the results from traditional and non-conventional 3D inversions, a geometry consisting of parallel profiles coinciding with some of those forming the standard ERT 3D acquisition was chosen.

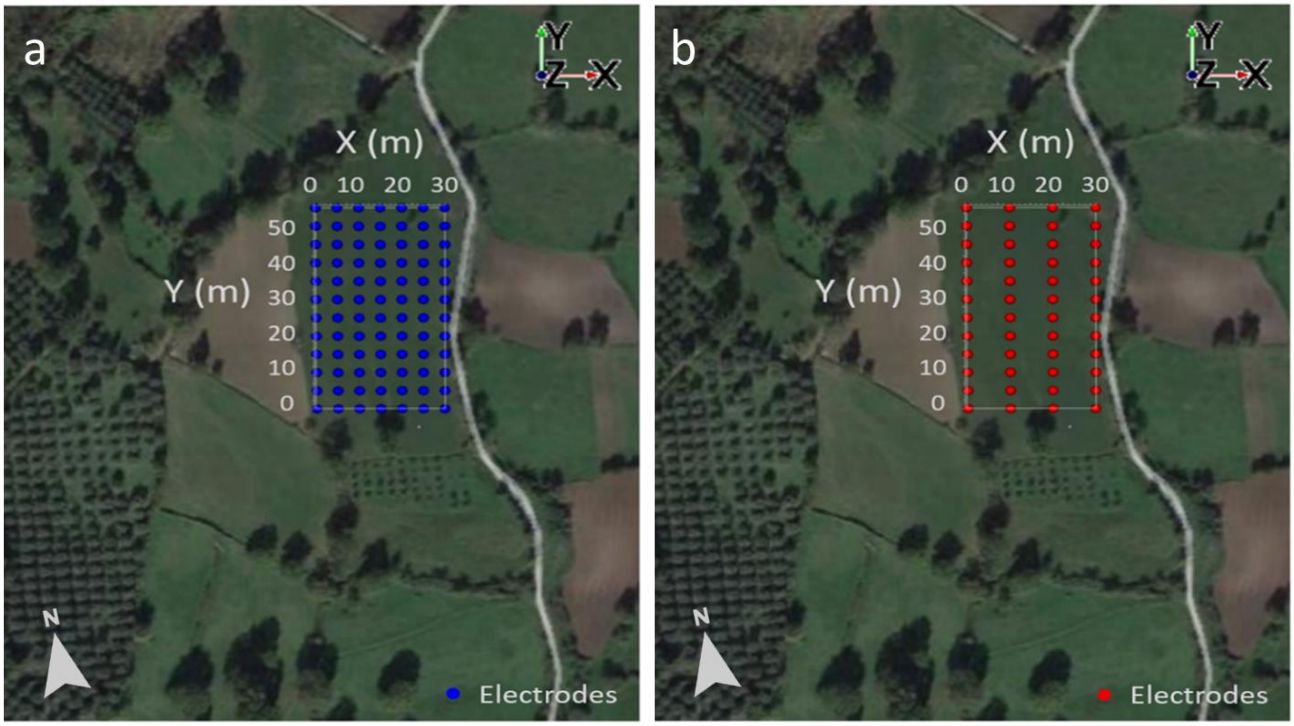

Figure 2.10 *Test area showing the electrode configurations used to test the efficiency of the proposed 3D ERT data acquisition technique: a) standard acquisition geometry; b) non-conventional acquisition geometry.*

The area, (30x55) m^2, has a flat topography. For the standard geometry, 84 electrodes were employed and distributed along seven parallel lines 5 m apart by using 12 electrodes for each line with an interelectrode distance of 5 m (blue dots in Fig. 2.10a). Whilist, for the non-conventional configuration 48 electrodes were used and located along four parallel lines with an inter-line space of 10 m and an electrode distance of 5 m. Therefore, 12 electrodes were used for each line (red dots in Fig. 2.10b). As it can be seen in Fig. 2.10b, the same area is covered with a number of electrodes almost half of those used for the standard configuration. Two data acquisition sequences were generated for the standard and non-conventional configurations, respectively, using the ERT-Lab Sequencer software (Fig. 2.10). The standard configuration allowed to obtain 470 quadrupoles by 70 current injections with period of 500 ms; the time interval for the data acquisition was about 7 minutes. The non-conventional configuration allowed to obtain 3419 quadrupoles by 370 current injections with period of 500 ms; the time interval for the data

acquisition was approximately 20 minutes. Therefore, the new proposed technique allowed to acquire a much larger number of data than that obtained with the standard technique despite the fact that fewer electrodes were used. This indisputable advantage of the new approach, which leads to ultra-high resolution 3D imaging of the investigated volume, is mainly due to the use of the latest generation Sequencer software (Figs. 2.8 and 2.9). The latter, indeed, permits to build acquisition sequences based on a continuous exchange between energizing dipole (TX) and receiving dipole (RX), also located on different cables (Morelli and LaBrecque, 1996), thus making possible to exploit all the possible TX/RX combinations of the specific electrode geometry adopted. In addition to the high-resolution, the new proposed technique is also able to reach an investigation depth greater than that obtained with the standard technique. This is clearly shown in Fig. 2.11, which displays the distribution of the measurement points extracted from the whole volume investigated by the standard and the non-conventional electrode configurations.

A scheme that synthesize the comparison between the acquisition parameters of the two techniques is shown in Tab. 2.2.

Technique	Array	Type of acquisition	Acquisition number	Electrode number	Quadrupole number	Electrode distance	Inter-line distance
Standard 3D ERT	Pole-dipole	3D	1	84	470	5 m	5 m
New 3D ERT	Pole-dipole	3D	1	48	3419	5 m	10 m

Table 2.2 *Comparison between the acquisition parameters used for the two 3D ERT surveys performed in the test area.*

The set of apparent resistivity data acquired for the two 3D ERT surveys has been appropriately filtered and only the data with a standard deviation (i.e. quality factor, Q) between 0 and 3 were used for the subsequent inversion process. The latter has been performed, for all the ERT surveys shown in this thesis, by taking into account

the elevations of the measurement electrodes, which have been acquired in the field using a high-precision GPS receiver.

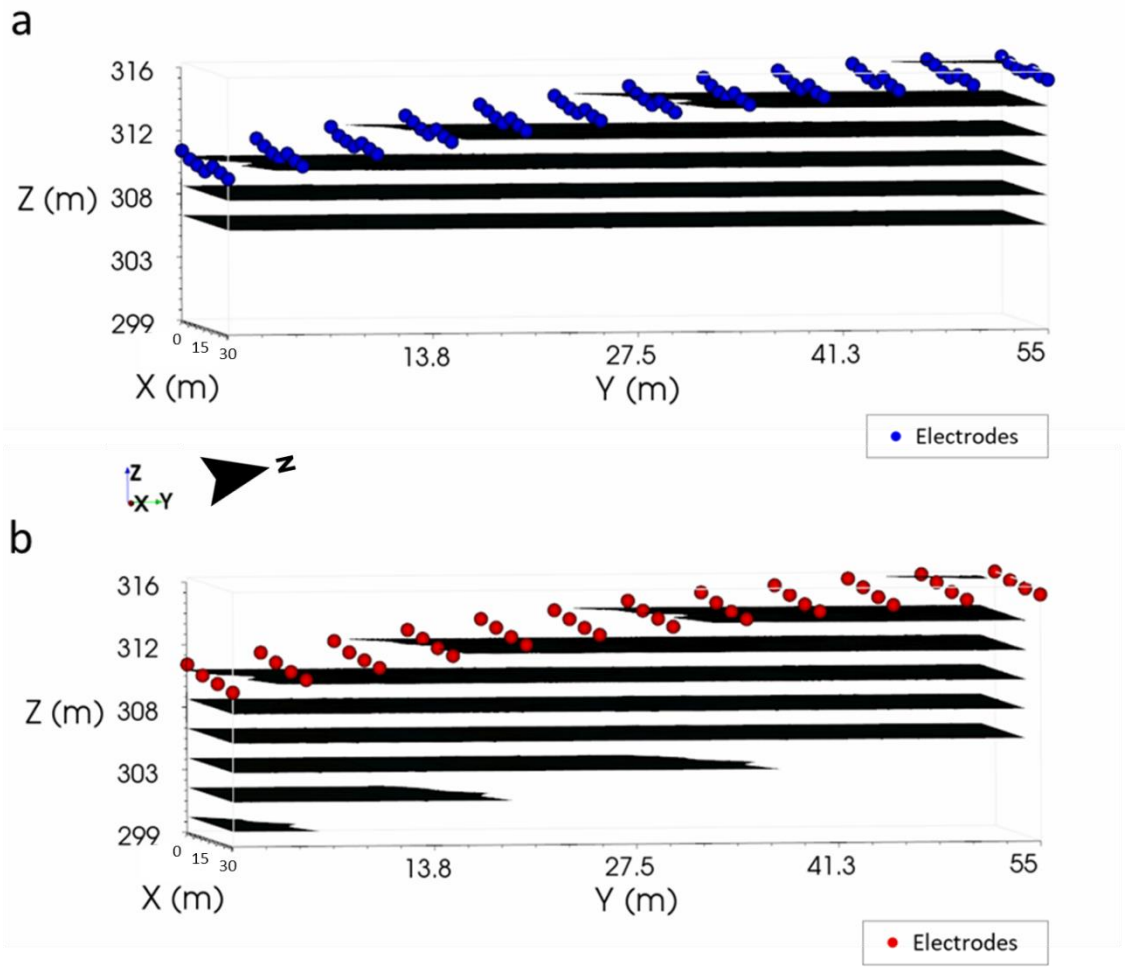

Figure 2.11 *Distribution of the measurement points (black strips) extracted from the whole volume investigated by standard (a) and non-conventional (b) 3D ERT data acquisition geometry.*

For a better visualization of the differences between the inversion results of the apparent resistivities collected by the two 3D ERT data acquisition techniques, Figs. 2.12 and 2.13 compare y-z plane slices and x-y plane slices, respectively, extracted from the 3D resistivity volumes corresponding to the two surveys. From the comparison, a higher resolution of the resistivity data volume provided by the non-conventional technique is clearly evident, despite the parallel branches were designed with equidistance not comparable with the electrode sampling step as for the standard technique. In fact, conductive anomalies, likely related to local lenses

of more or less imbibed material, are very well identified (Fig. 2.12b), as well as the geometry of resistive anomalies ascribable to not very compact material lenses (Fig. 2.13), which are also well evident in Fig. 2.12b. We note that the inversion results shown in Figs. 2.12a and 2.12a do not provide a reliable reconstruction of the investigated subsurface volumes due to the strong interpolations in areas not covered by data actually acquired. Therefore, the classic 3D ERT, in addition to being more expensive in terms of electrode installation times, appears to be reliable with a good approximation only for areas whose stratigraphy is not affected by abrupt lateral resistivity changes, as shown by the comparison in Figs. 2.12 and 2.13.

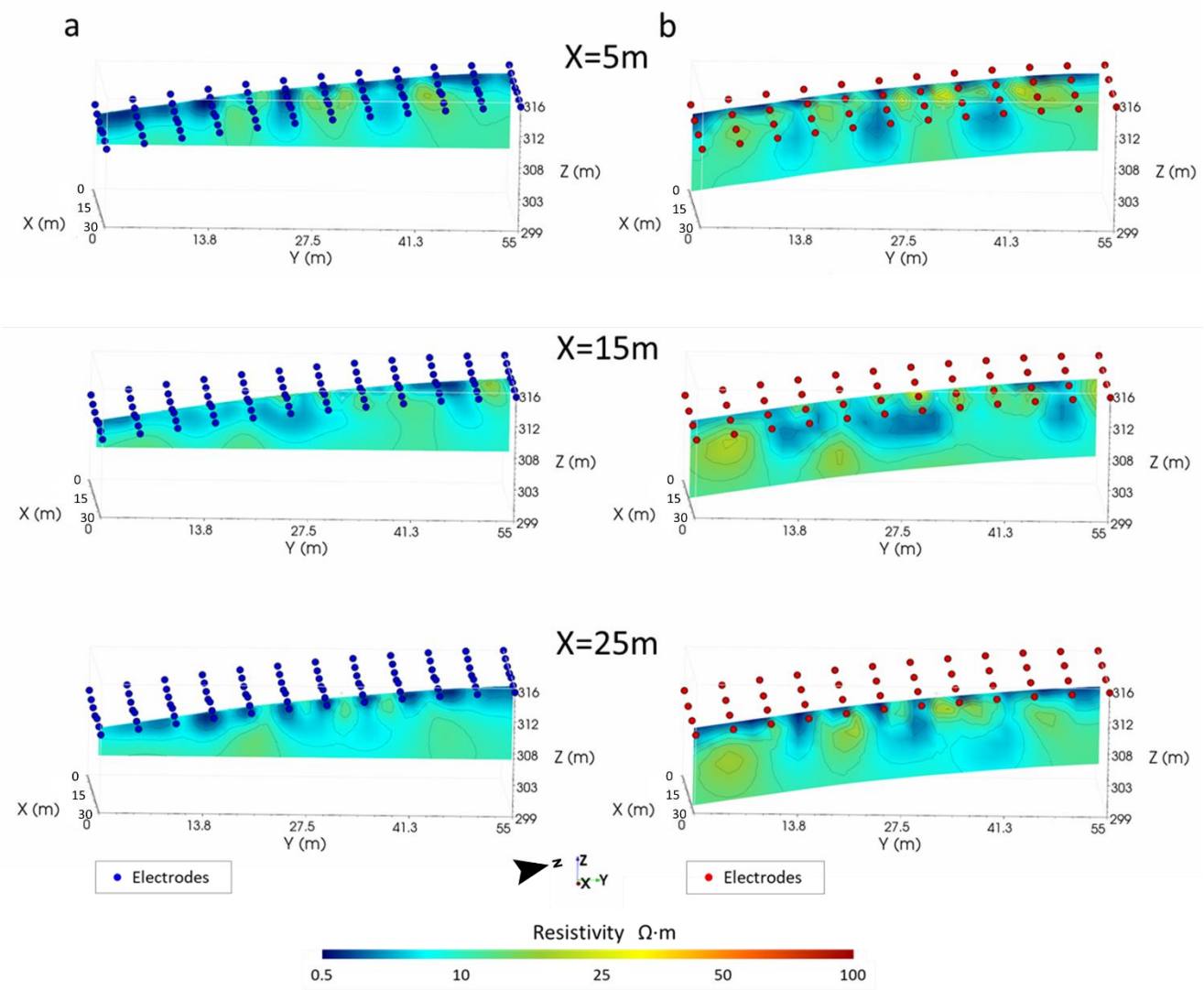

Figure 2.12 *Comparison between three y-z plane slices extracted from the 3D resistivity distributions provided by the inversion of the two sets of apparent resistivity data collected by using, respectively, standard (a) and non-conventional (b) 3D ERT data acquisition geometry.*

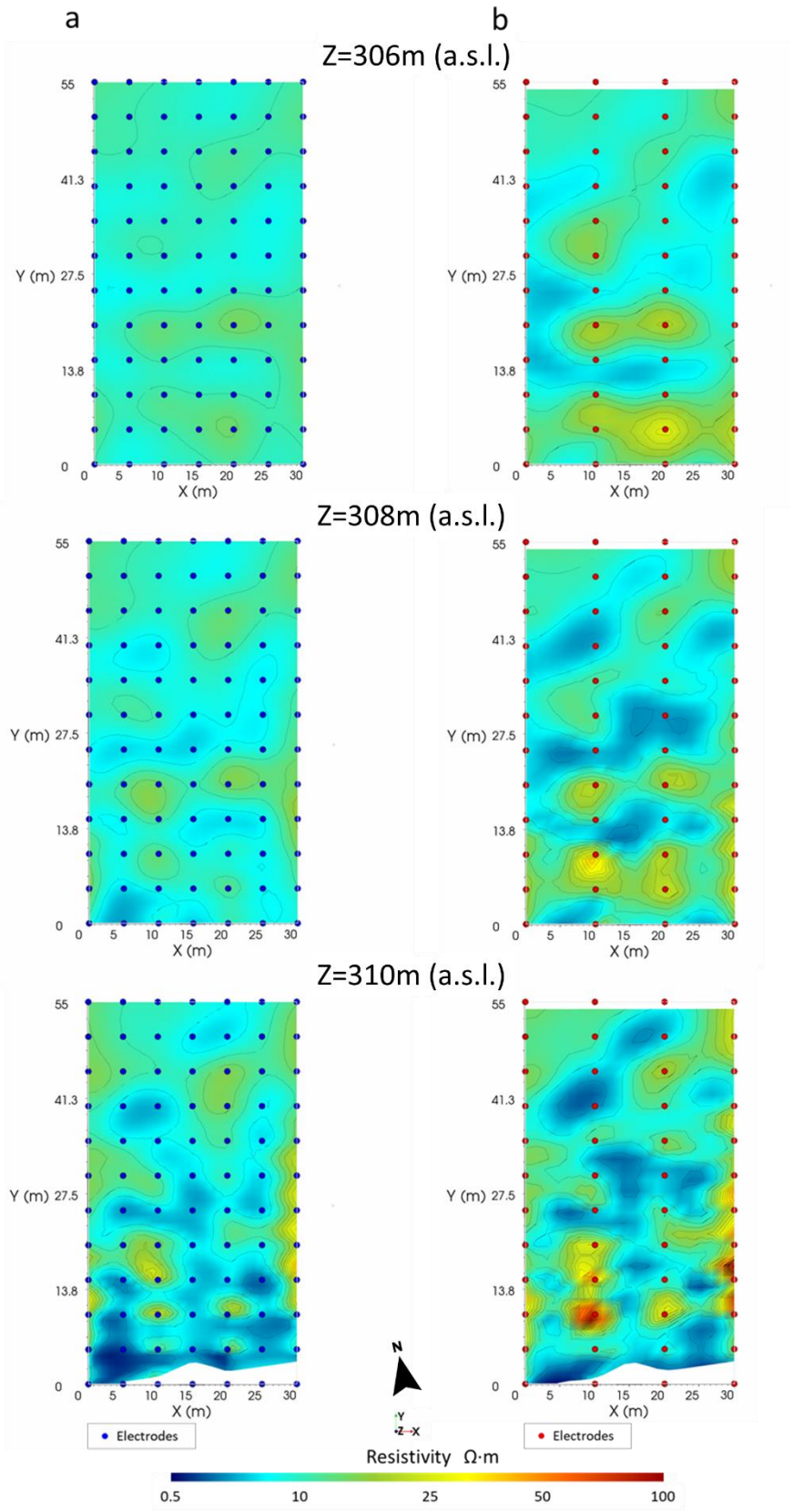

Figure 2.13 *Comparison between the Z slices extracted from the 3D resistivity distributions provided by the inversion of the two sets of apparent resistivity data collected by using, respectively, standard (a) and non-conventional (b) 3D ERT data acquisition geometry.*

In the light of the obtained results, it follows that 3D ERT surveys based on the innovative non-conventional data acquisition technique are to be preferred for the reconstruction of volumes characterized by conspicuous presence of fluids, such as those affecting the Matese areas, which are the focus of the present study. Indeed, the proposed technique, besides being faster, is more suitable in providing a detailed modeling of the underground fluid circulation and of the CO_2 plumes, which are typically 3D targets.

2.2 Applications to different fields of geophysics

In this section, the results of the proposed 3D ERT data acquisition technique applied to different exploration fields are presented and discussed.

2.2.1 3D reconstruction of buried civil engineering structures

The first two case-studies that we will illustrate refer to the identification, in logistically unfavorable contexts, of 3D structures of civil engineering interest. The aims of the two 3D ERT surveys are: in the first case, the identification of a conductive structure (concrete with metal reinforcement) in a conductive geological context; in the second case, the detection of a cavity in a resistive geological context. Fig. 2.14 shows the non-conventional 3D electrode configuration used in the first survey below the road Grosseto-Fano (central Italy). The aim of the work was the detection of the foundation, which support a bulkhead (De Paola et al., 2017). The fig. 2.15 shows the acquisition setting used in the second test case. The aim was the characterization of the material covering the tunnel in Palizzi area (SS 106 Jonica, southern Italy), which was escavated in a karst rock (De Paola et al., 2018).

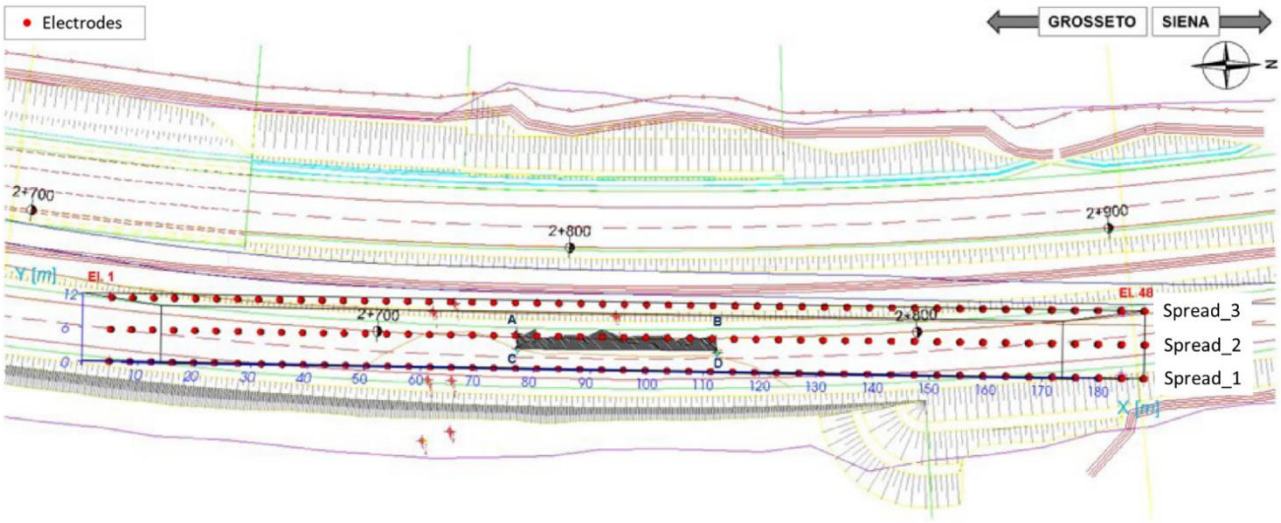

Figure 2.14 3D ERT *acquisition geometry used for the Grosseto-Fano highway survey (central Italy) (De Paola et. al., 2017).*

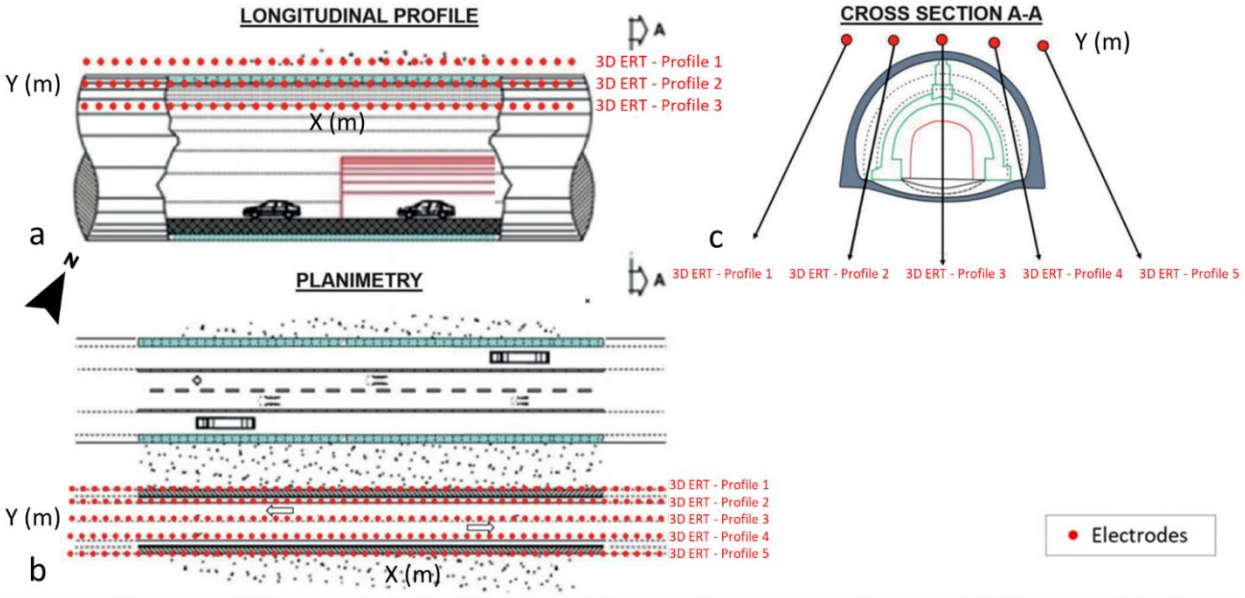

Figure 2.15 *3D ERT acquisition geometry used for the Palizzi survey area (SS 106 Jonica, southern Italy) (De Paola et. al., 2018).*

The first survey (Fig. 2.14) was performed with 3 parallel lines with an inter-space of about 6 m. Each line has 48 electrodes with an electrode distance of 4 m. The electrodes were inserted in the 40 cm deep hole located some in the ground and some in the asphalt. The chosen geometry allowed an investigation depth of

approximately 31 m below the ground level (b.g.l.). Two 3D acquisitions were made by using spreads_1_2, and spreads_2_3, respectively (see Fig. 2.14), which were then superimposed on the central spread_2 to guarantee total data coverage of the survey area. The geological setting of the area consists of quaternary soils of continental deposit represented by floods. The latter are more gravelly at the base and have frequent sandy and clay-silty levels upwards. From the analysis of the electrical tomographs (Fig. 2.16) obtained by the 3D inversion of the acquired apparent resistivity values, it is resulted that the poles are about 18÷20 m long starting from the top of the bulkhead. In particular, Fig. 2.16a shows the 3D model of the investigated volume in terms of electrical resistivity (ρ) distribution (Fig. 2.16a), while Figs. 2.16b,c highlight the very low-resistive zone (0.2 Ωm < ρ < 20 Ωm) likely related to the bulkhead. The latter appears characterized by a planar dimension of about 36 x 3.8 m^2, whose top is at 309.7 m above sea level, as subsequently verified through direct investigations (De Paola et al., 2017).

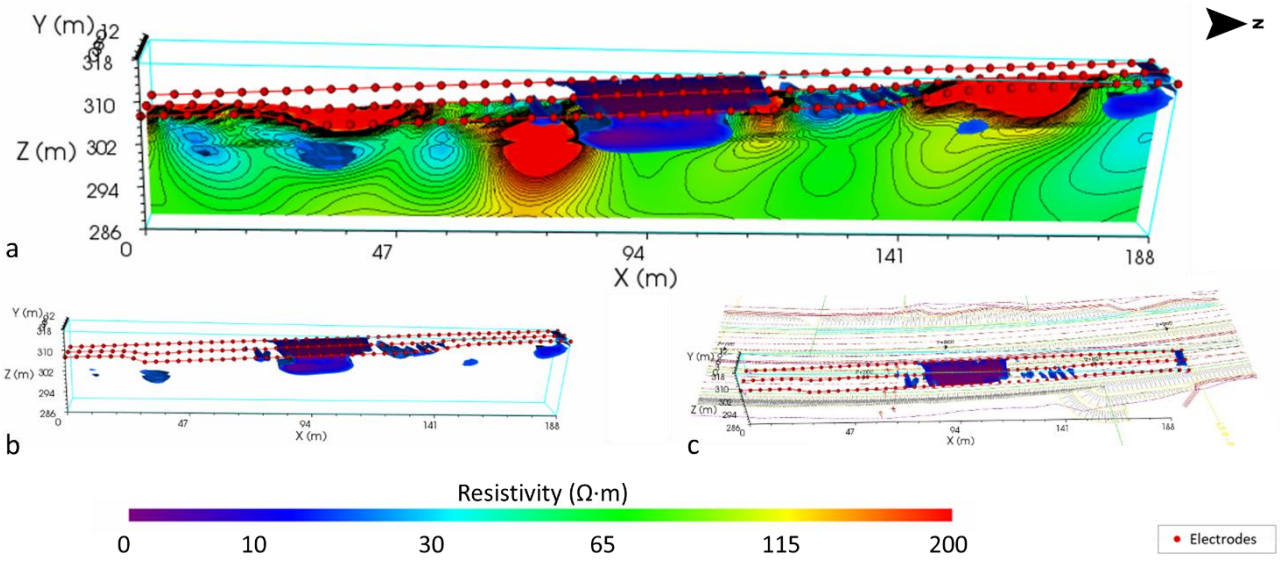

Figure 2.16 *High-resolution 3D electrical resistivity tomography obtained for the Grosseto-Fano motorway survey area (central Italy). a) 3D ERT model; b) low-resistivity volume (0.2 Ωm < ρ < 20 Ωm) observed between the progressive 74 and 114 along the X axis, which models the pile of bulkheads sought; c) the same volume shown in b) with top view (modified from De Paola et. al., 2017).*

The second case-study involved the use of a non-conventional 3D electrode geometry consisting of 5 profiles, 6 m apart from each other, formed by 48 electrodes spaced 2.5 m (Fig. 2.17).

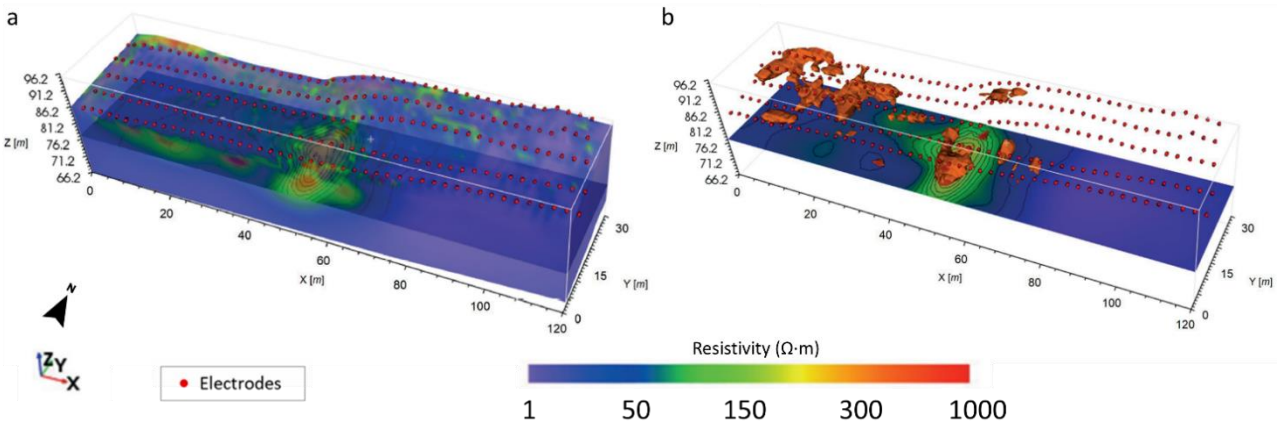

Figure 2.17 *High-resolution 3D electrical resistivity tomography obtained for the Palizzi survey area (SS 106 Jonica, southern Italy). a) 3D resistivity model; b) view of subsoil portions corresponding to the most resistive ranges (ρ ≥ 700 Ω·m) of Palizzi investigated area (from De Paola et. al., 2018a).*

The survey area is characterized by quaternary deposits. In particular, the studied deposit formation is an alternation of sand and silt, which appear more gravelly at the base (sand with metamorphic clasts). In civil engineering works, the presence of these poor cohesive deposits is an element of risk, because they can generate detachments during a tunnel excavation. The data processing showed a clear contrast between the sedimentary cover and the void created during the tunnel excavation, subsequently verified with direct investigations (De Paola et al., 2018). Indeed, the volumes characterized by high-resistivity values (> 800 Ωm) can be ascribed to the presence of cavities (see Fig. 2.17b), while values in the range 150 Ωm < ρ < 700 Ωm are representative of unconsolidated material and, finally, low-resistivity values, in the range 1 Ωm < ρ < 150 Ωm, can be associated with formations rich in silts and clay, which are present in the examined area (De Paola et al., 2018).

2.2.2 3D characterization of a steep slope susceptible to debris flow

In this section the results of the proposed technique applied to the electrical characterization of a steep pyroclastic cover, whose complex topography prevented the use of conventional electrode arrays, are briefly presented. The study area (Fig. 2.18) is sited on a pyroclastic slope of Mt. Faito (Campania Region, southern Italy), which is an area susceptible to flowslide and debris-flow phenomena (i.e. fast flow-like landslides) (De Paola et al., 2018b; Di Maio et al., 2020). Mt. Faito (1,131m a.s.l.), belonging to the Lattari Mts. in Sorrento Peninsula (Fig. 2.18a), is located inside the morphological-structural depression known as Campanian Plain (southern Italy), formed during the Plio-Quaternary phases of the southern Apennine orogenesis.

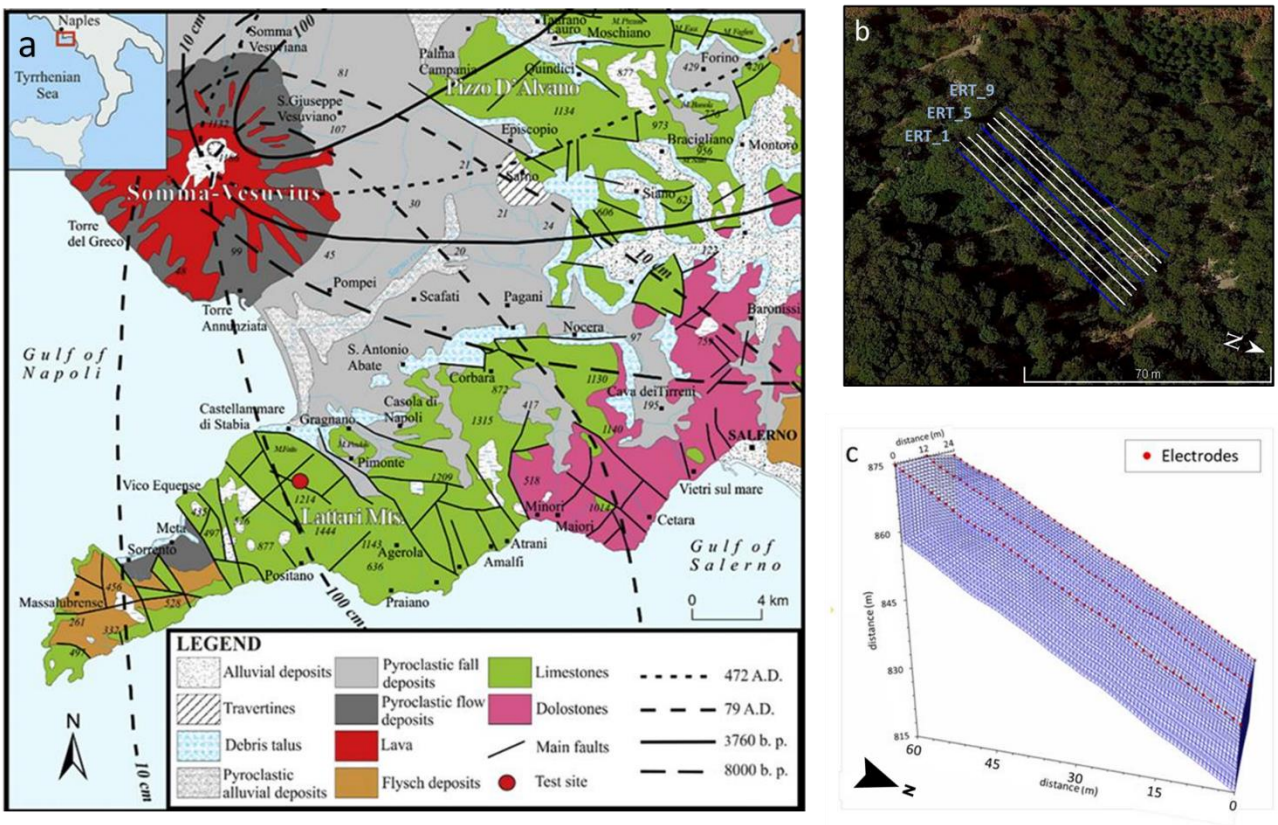

Figure 2.18 *Mt. Faito survey area (Campania Region, southern Italy): (a) geological map of the Sorrento Peninsula; (b) geophysical study area; (c) 3D mesh of the survey volume (from De Paola et. al., 2018b).*

The local stratigraphical setting of the survey area is shown in Fig. 2.19. It is made of a shallow layer (A), which can be divided into two pyroclastic horizons, A1 and A2: the former (20-30 cm thick) represents the upper portion of the soil affected by the action of microorganisms and vegetation; the latter (40-100 cm thick), made of brown pumice rich silty-sands, is representative of the final stage of the 79 CE eruption. The layer A overlaps a layer B, which consists of coarse white pumices of variable thickness (< 1 m up to > 2 m) and represents the main deposit of the ash fallout from the Mt. Vesuvius eruption occurred in 79 CE. Below B, a layer C is observed which consists of products from an older volcanic eruption (Ancient Phlegraean fall) generally splitted into three sublayers (more details are given in Di Maio et al., 2020). The described pyroclastic soil sequence buries the bedded limestone bedrock (R).

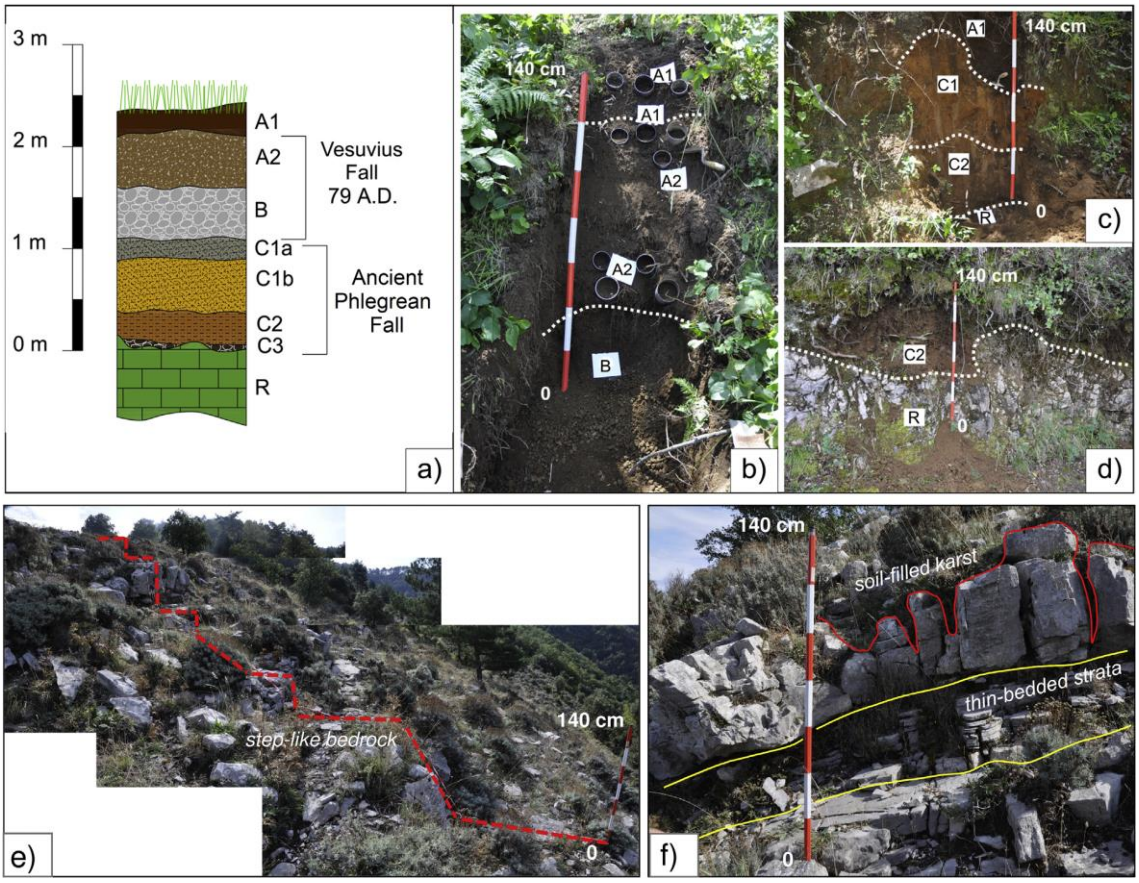

Figure 2.19 *a) Stratigraphic sequence of the Lattari Mts. (Naples, southern Italy; b) details of the 79 CE stratigraphic sequence; c) stratigraphic sequence of the Ancient Phlegraean fall; d) stratigraphic contact with the bedrock; e) limestone step-like bedrock; f) thin-bedded strata and detail of the upper karst portion (from Di Maio et al., 2020).*

The test site was chosen by virtue of the presence of the main geological and stratigraphic features significant for the initiation of flowslides. Indeed, it is characterized by a fractured and karst limestone bedrock covered by pyroclastic soils 1-2 m thick and slope angles between 27° and 35°, which are critical values for triggering such types of landslides. Observation of many flowslides in Campania Region has clearly shown that the trigger is caused by local slope conditions, which can vary within a wide range, resulting in a possible unfavourable combination. Buried predisposing factors are: i) critical geomorphological and stratigraphic contacts between shallower soils and bedrock (steeper than the average slope); ii) almost impermeable layers consisting of clayey ashes that seal the fractured limestone below the pyroclastic soils; iii) any preferential rainwater infiltration path,

consisting of zones of greater permeability; iv) springs that feed the surficial pyroclastic cover. It is therefore crucial to obtain accurate 3D reconstructions of the soil layers and their saturation degree, which can be only provided by high-resolution 3D ERT investigations.

The non-conventional 3D electrode geometry chosen for this survey area is consisted of three profiles of length 70.5 m and distant 12 m each other (blue lines in Fig. 2.18b). Thus, the three-dimensional ERT data were collected on a rectangular grid of (70.5 × 24.0) m^2 (Fig. 2.18b) (De Paola et al., 2018). A total of 144 electrode stations (red dots in Fig. 2.18c) along 3 lines, plus two infinite electrodes, were arranged in the field, and 23.200 data points were collected using the pole-dipole array with an inter-electrode space of 1.5 m. From the analysis of the 3D data inversion results shown in Fig. 2.20, a clear contrast between the pyroclastic cover and the limestone bedrock is well evident. Indeed, high-resistivity values, in the range 3000 Ωm < ρ < 7000 Ωm (Fig. 2.20b), characterize the shallowest layer, about 3-5 m thick, related to pumiceous pyroclasts whose grain size reduces from lapilli to coarse ashes. Conversely, low-resistivity values, in the range 200 Ωm < ρ < 500 Ωm (Fig. 2. 20b), characterize the upper part of the carbonate basement, about 4-5 m thick, likely associated to a high fracturing level and to karst phenomena, which favor water infiltration. Finally, the increasing of the resistivity values in the deeper portion of the investigated volume (800 Ωm < ρ < 2000 Ωm) should be associated to a low number of fractures and an unsaturation condition of the bedrock (De Paola et al., 2018).

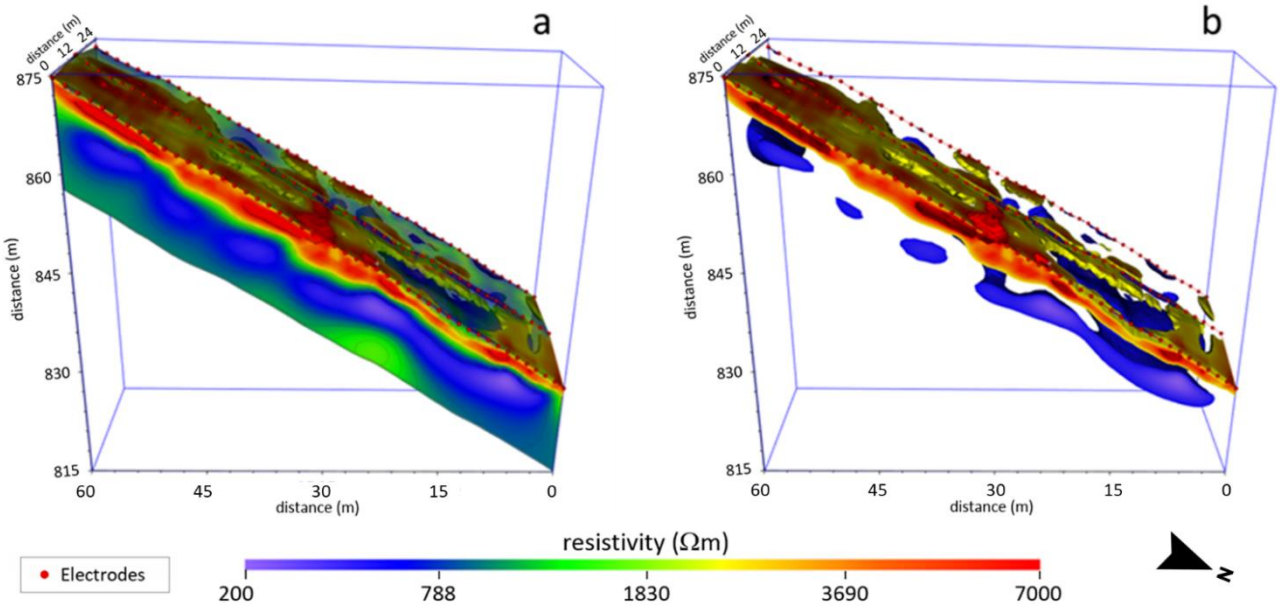

Figure 2.20 *High-resolution 3D electrical resistivity tomography obtained for the Mt. Faito survey area (Campania Region, southern Italy). (a) 3D resistivity model of the investigated volume; (b) subsurface volumes corresponding to the highest and lowest resistivity ranges, respectively, 3000 Ωm < ρ < 7000 Ωm (red-orange colour) and 200 Ωm < ρ < 500 Ωm (blue colour) (from De Paola et. al., 2018b).*

It is worth noting that, despite the logistical problems of the study area, due to high slope angles and dense vegetation, the adopted data acquisition scheme has provided a high-resolution geoelectrical characterization of the pyroclastic cover, whose knowledge is crucial for the identification of the factors that favour the triggering of dangerous debris landslides induced by intense rainfall events. In particular, the obtained resolution was found higher than that provided by a conventional 2.5D ERT survey performed along 9 parallel profiles (ERT_1÷ERT_9 in Fig. 2.18b) covering the survey area, whose results are shown in Fig. 2.21.

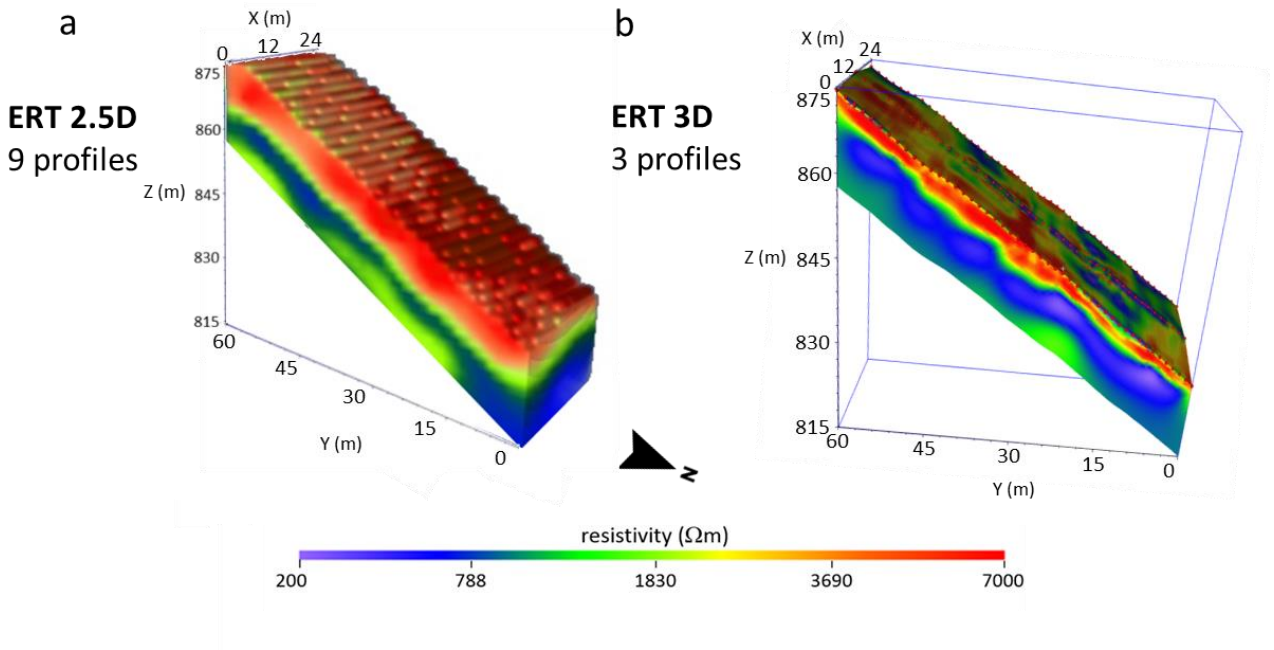

Figure 2.21 *Comparison of the results obtained for the Mt. Faito survey area (Campania Region, southern Italy). (a) 2.5D resistivity model of the investigated volume obtained from data acquired through profiles 1-9 (blue and white lines in Fig. 2.18b); (b) 3D resistivity model of the investigated volume obtained from data acquired through profiles 1, 5, 9 (blue lines in Fig. 2.18b) (from De Paola et. al., 2018b).*

2.2.2 3D modelling of the buried volume beneath a historical building

The use and form of many historical monuments have changed over the centuries due to various reasons which are sometimes difficult to recognize.In seismic areas, these monuments represent structures potentially capable of recording the effects of historical earthquakes, which research must decode before the restoration and architectural modification phases. These considerations apply to the Basilica of Santa Maria near Alvignano village (northern Campania Region, southern Italy), which has registered restorations and superpositions of more recent buildings throughout the centuries. Although the uncertainties cannot be dismissed regarding the nature of the historical damage in the Basilica, the tilting of almost all pillars, the crushed arches and the restoration of the apse have led to the hyphotesis that this damage was caused by an earthquake solicitation, whose effects could be locally

amplified by poor geological conditions. To gain information on the physical and geometrical features of the shallow subsurface beneath the Basilica of Santa Maria, which could explain the observed damages as a result of seismic shaking, a high-resolution 3D ERT survey was performed by using a non-conventional electrode geometry (Bottari et al., 2020). Specifically, a U-shaped electrode distribution along three sides of the Basilica (Fig. 2.22), and a sequence of ad hoc designed measures, were used to achieve uniform coverage along the three measurement profiles and in the investigated volume underneath the Basilica. It is worth noticing that such an arrangement was chosen to overcome logistic constraints, because the use of electrodes fixed in the floor was prevented.

Figure 2.22 *U-shaped electrode distribution along three external perimeter walls (dashed red lines) of the Basilica of Santa Maria near Alvignano village (northern Campania Region, southern Italy) (modified from Bottari et al., 2020).*

The ERT measurements were realized with 96 electrodes (38 along the two parallel lines and 20 along the perpendicular one) by using the IRIS Syscal Pro 96 multi-channel georesistivimeter (Bottari et al., 2020). The choice of the pole-dipole array with an inter-electrode space of 1.2 m allowed us to get 11.315 data points inside the investigated volume, and an investigation depth of about 9 m below the ground level was reached after inversion of the acquired apparent resistivity data (Fig. 2.23).

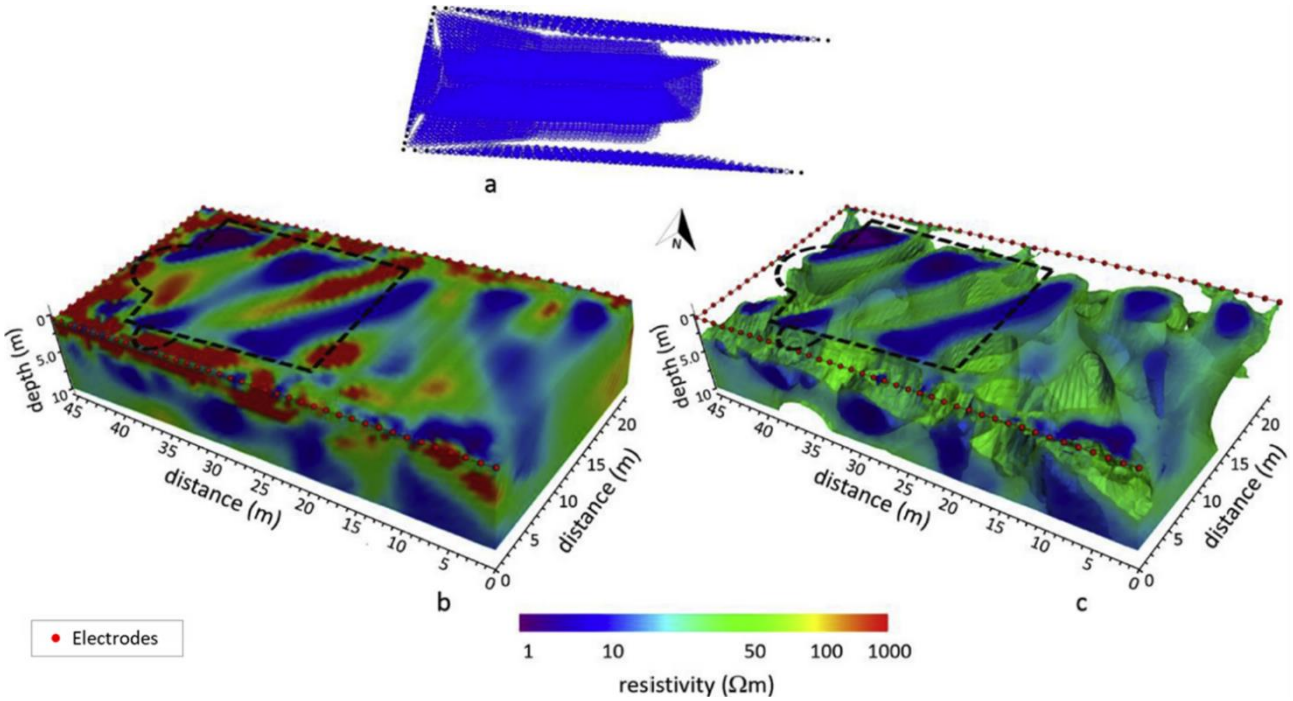

Figure 2.23 *High-resolution 3D electrical resistivity tomography obtained for the Alvignano survey area (Campania Region, southern Italy). a) 3D grid of the measurement points coming from the used cross-cable sequence; b) 3D electrical resistivity model of the investigated volume; c) resistivity volume displaying the following ranges of ρ values: 1 Ωm < ρ < 10 Ωm (blue colour), 10 Ωm < ρ < 30 Ωm (green colour). The black dashed line marks the perimeter walls of the Basilica (from Bottari et al., 2020).*

As shown in Figs. 2.23b and c, the buried volume appears generally conductive with resistivity values ranging from a few Ωm to about 30 Ωm, suggesting a significant looseness and saturation degree of the investigated deposits (Bottari et al., 2020). Fig. 2.24 shows the inverted resistivity volume by slices corresponding to four different depths, in order to better highlight the in-depth resistivity variations. At a depth of 1.5 m, alternated conductive and resistive strips with parallel NE-SW orientation are visible in the resistivity value distribution in the area below the Basilica paved floor. Interestingly, this alternate sequence disappears at depths greater than 4 m and a general increase of the resistivity value distribution is observed below the southern aisle area. This increasing trend of resistivity is found in the southern sector except for the region around the pillar marked by a black point in Fig. 2.24, where a reverse trend in resistivity values is observed and the

largest deformations of pillars are found. The 3D distribution of the resistivity values observed beneath the Basilica agree well with the data of boreholes drilled in its surrounding. These data, indeed, reveals that the shallow stratigraphy of the area consists of a layer made up of 1–1.5 m of vegetable-colluvial soil with reworked anthropic and pyroclastic material, which can be classified as a loose, incohesive sandy silt, followed by a 15–20 m thick sequence of ash deposits, locally containing altered pumice and lapilli clasts. Thus, the presence of loose and argillified pyroclastic deposits in the first 10÷15 m below the ground level could have caused the deformations observed in the pillars. Moreover, the lateral and vertical variations in resistivity values observed down to the maximum exploration depth (Figs. 2.24) suggest a significant inhomogeneity of the investigated deposits, which is compatible with different degrees of clay content. This inhomogeneity could have amplified the site effect during seismic shaking and caused the vertical crashing of the left aisle arches (Bottari et al., 2020).

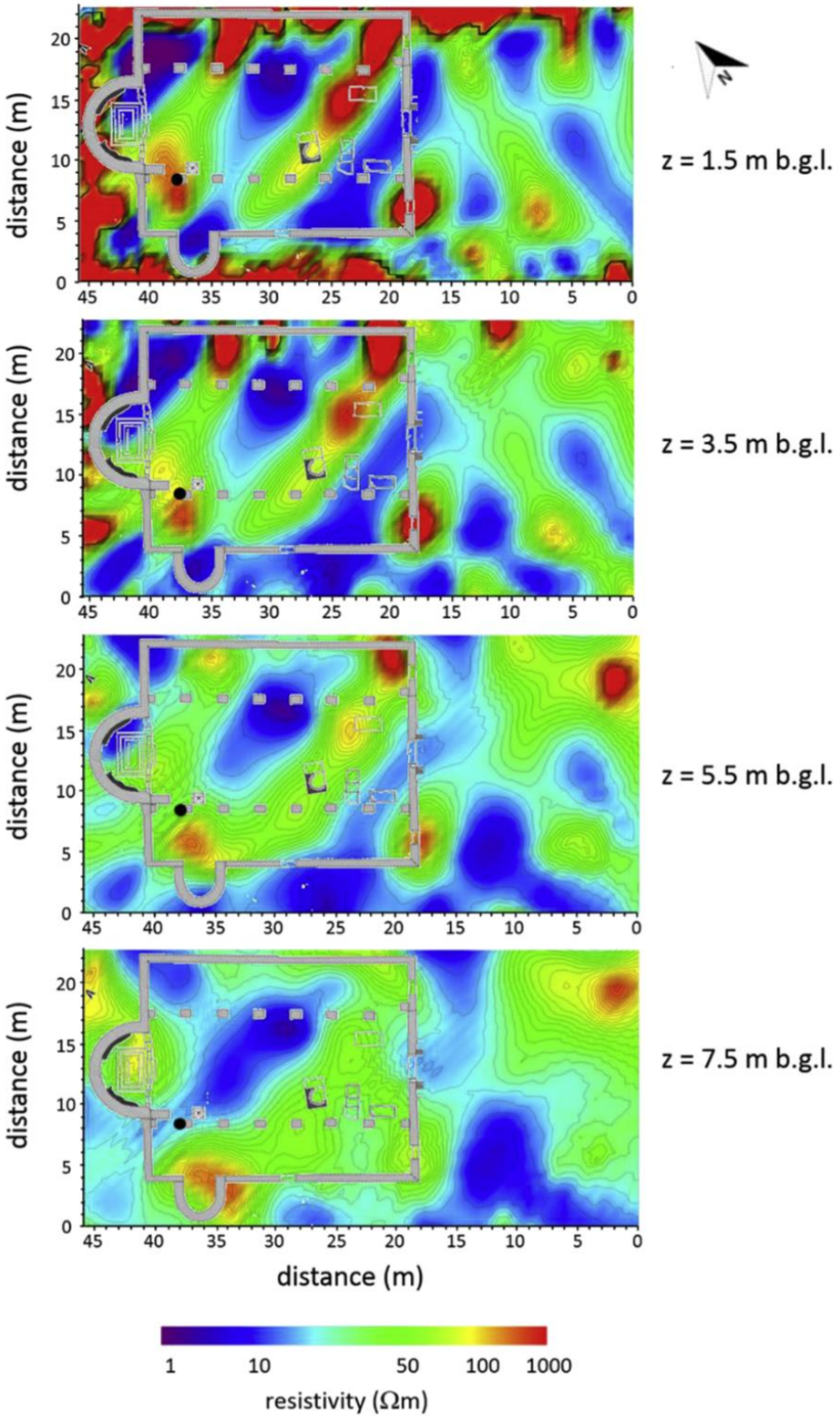

Figure 2.24 *Four slices of the 3D resistivity model shown in Fig. 2.23 at different depths superimposed on the plan of the Basilica of Santa Maria. The black dot marks a pillar of the left aisle (from Bottari et al., 2020).*

Chapter 3.

Geological background of active fault zones in the Matese ridge area (southern Italy)

3.1 Geological background and tectonic evolution of the southern Apennines

The southern Apennines (Fig. 3.1) are an orogenic belt derived from the convergence of the African and Eurasian plates in Late Cretaceous to Quaternary times (e.g. Dewey et al., 1989; Mazzoli and Helman 1994; Turco et al., 2012, and references therein), accompanied by the motion of minor blocks such as Corsica–Sardinia–Calabria (of European origin) and Adria (of African affinity).

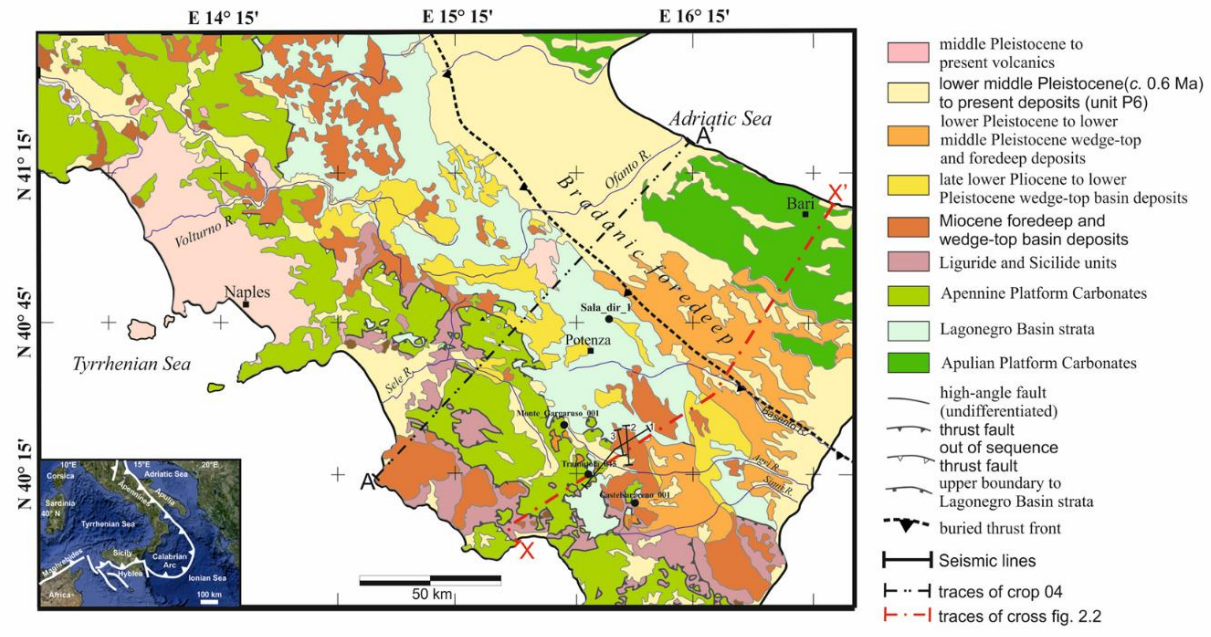

Figure 3.1 *Geological map of the southern Apennines (from Candela et al., 2015).*

These processes consumed the Neo-Tethyan oceanic lithosphere originally interposed between the two continental palaeomargins, whose evidences are the

outcrops of continental crust units of the Calabrian Arc (Bonardi et al., 1988; Ciarcia et al., 2009; Vitale et al., 2011; Ciarcia et al., 2012; Vitale et al., 2013). Thrusting was accompanied by back-arc extension and sea-floor spreading, first in the Liguro-Provençal Basin (Late Oligocene to Early Miocene) and then, in Late Miocene–Quaternary times, in the southern Tyrrhenian Sea (e.g. Faccenna et al., 1996; 1997; Kastens et al., 1988; Sartori, 2003, and references therein). In the Middle Pleistocene, crustal shortening ceased (e.g. Patacca and Scandone, 2001; Patacca et al., 2008) and NE-SW oriented horizontal extension became dominant over the whole orogen, where extensional faults postdate and dissect the thrust belt (e.g. Butler et al., 2004). Such faults are responsible for the active tectonics and seismogenesis in the southern Apennines (e.g. Cello et al. 1982; Cinque et al., 1993; Patacca et al., 1993; Hyppolyte et al., 1994; Cello et al., 2000; Caiazzo et al., 2006; Ascione et al., 2007). At a regional scale, the southern Apennines can be subdivided into three main elements: (i) the Bradanic foredeep, (ii) the Apennine accretionary wedge and (iii) the buried Apulian Platform (Fig. 3.2).

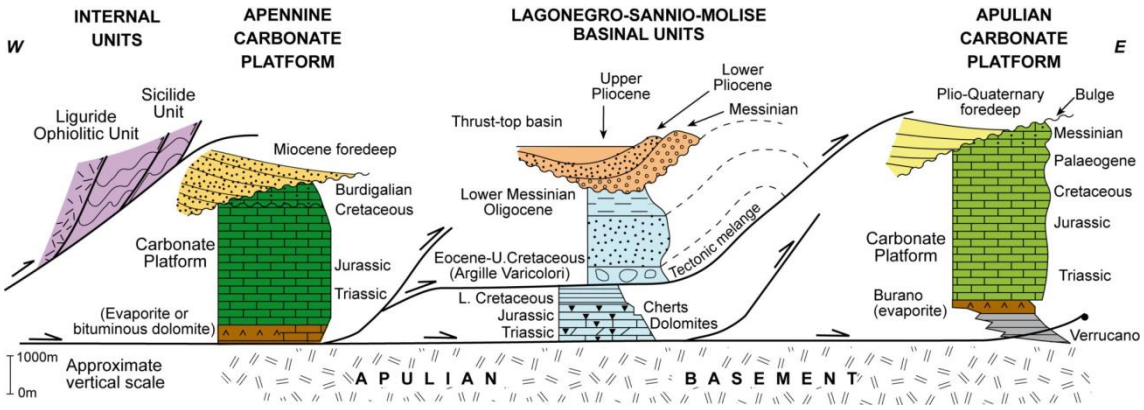

Figure 3.2 *Tectono-stratigraphic scheme of the southern Apennines (modified from Roure et al., 1991).*

The first element represents the main deposition of the Pliocene-Quaternary foreland basin system. The Apennine accretionary wedge is composed of Mesozoic-Tertiary carbonate platform/slope successions (Apennine Platform) and pelagic

basin successions (Lagonegro), stratigraphically covered by Neogene foredeep and wedge-top basin sediments. The structure at surface is characterized by low-angle tectonic contacts separating the Apennine Platform carbonates, in the hanging wall, and the Lagonegro basin successions in the footwall. These tectonic contacts consist of both thrusts – in part reactivated during extensional stages – and newly formed low-angle normal faults (Mazzoli et al., 2014). The buried Apulian Platform has a thickness from 6 km to 8 km and consists of a Mesozoic-Tertiary shallow-water carbonate succession continuous with that outcropping in the foreland to the NE (Shiner et al., 2004, and references therein). The detachment between the allochthonous units and the buried Apulian Platform unit is marked by a mélange zone of variable thickness, locally reaching ca. 1500 m (Mazzoli et al., 2001). The buried Apulian Platform is characterized by reverse-fault-related, open, long-wavelength folds that form the hydrocarbon traps for the significant oil discoveries in southern Italy (Shiner et al., 2004). Geophysical evidence shows that the crystalline basement is involved in deep-seated reverse faulting (Speranza and Chiappini, 2002; Improta and Corciulo, 2006; Steckler et al., 2008). The associated deformation is represented by significant vertical offsets along steep reverse faults, with relatively limited horizontal displacements. The involvement of the basement in different shortening phases suggests that the geodynamic evolution of the southern Apennines fold and thrust belt involves a mix of thin-skinned and thick-skinned tectonic styles (Fig. 3.3) (e.g. Menardi Noguera and Rea, 2000; Shiner et al., 2004; Butler and Mazzoli, 2006; Cippitelli, 2007; Mazzoli et al., 2008; 2012).

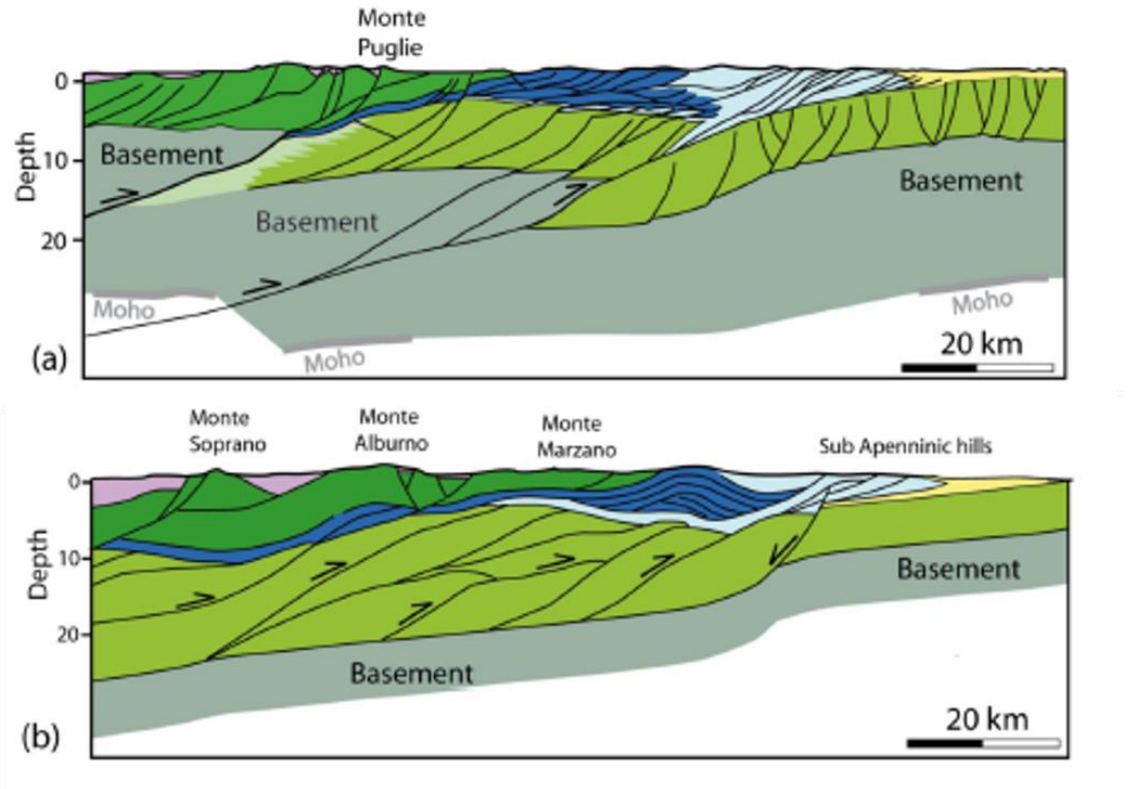

Figure 3.3 *Thin-skinned (a) and thick-skinned (b) tectonic styles (from Scrocca et al., 2010).*

The final switch from a thin-skinned to a thick-skinned style of thrusting has been related to the involvement of the Apulian Platform carbonates – and the underlying thick Adriatic crust – in shortening (e.g. Mazzoli et al., 2000; Shiner et al., 2004; Mazzoli et al., 2008; 2011), and possibly with slab detachment (Ascione et al., 2012) (Fig. 3.4).

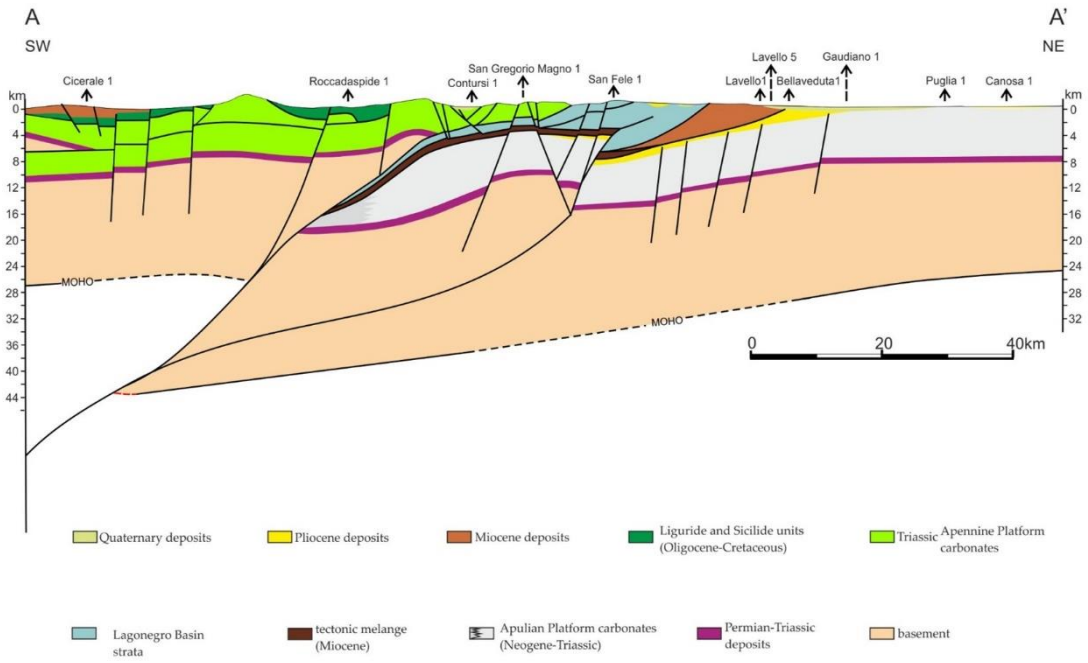

Figure 3.4 *Regional cross-section along the CROP-04 reflection seismic profile (modified from Mazzoli et al., 2013).*

Since the end of Middle Pleistocene (ca. 0.7 Ma), a substantial uplift of the outer domains of the chain and of the Bradanic foreland basin area (Fig. 3.4) occurred, being estimated to approximately 600-700 m (Cinque et al., 1993; Amato and Cinque, 1999). This uplift has been attributed to the rebound of the Apulian slab following complete detachment (Cinque et al., 1993; Ascione et al., 2012). Coeval erosion in the southern Apennines foothills and Bradanic foredeep is recorded by valley incision, providing mean erosion rate values of 0.2-0.3 mm/y (Amato et al., 2003). The sedimentary record of the Sant'Arcangelo wedge-top basin in the ca. 1.0-0.7 Ma time span provides mean erosion rate values of 0.25±0.07 mm/y (Capalbo et al., 2010). Although mean erosion rates can be different in general from millennial-scale erosion rates, cosmogenic nuclide-based erosion rates in the southern Apennines indicate similar values, ranging from 0.2 to 0.4 mm/y (Cyr et al., 2008).

3.2 Geological setting of the survey areas

The topography of the Matese area is dominated by the 2200 m high Matese ridge. This area is located in the Campania-Molise sector of the southern Apennines. In the study area, tectonic units of the fold and thrust belt are composed of Mesozoic-Tertiary successions covered by late Miocene foredeep basin deposits (Fig. 3.5).

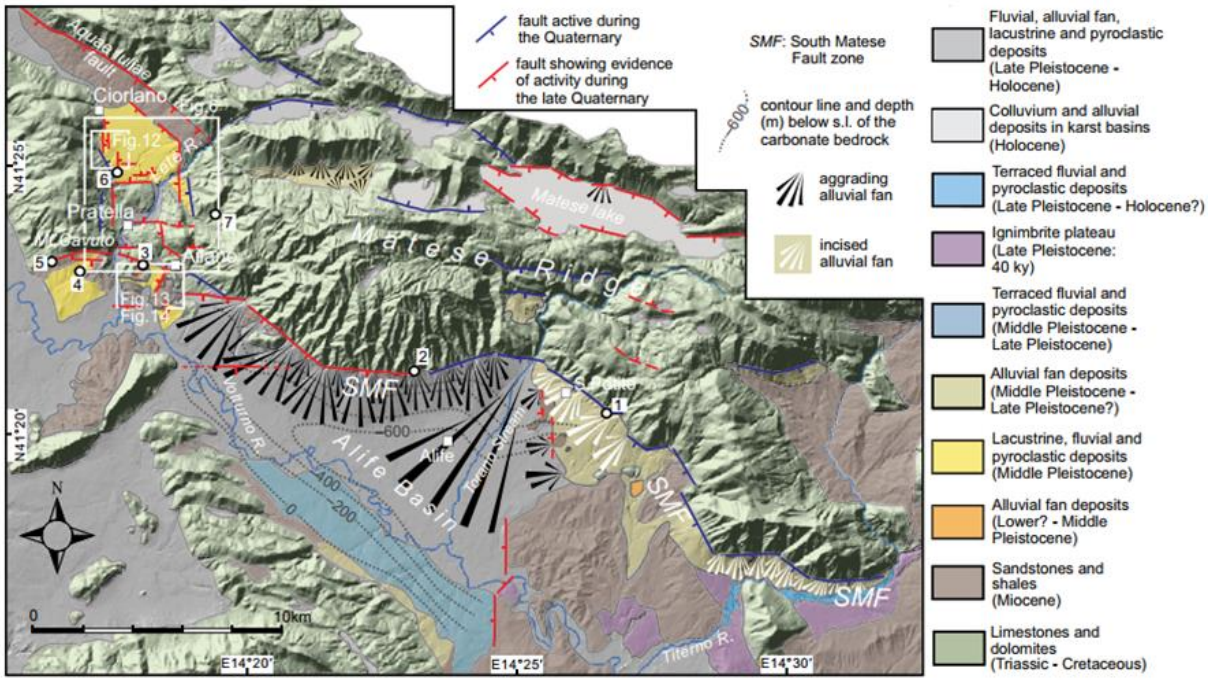

Figure 3.5 *Simplified geological map of the study area (from Ascione et al., 2018).*

These consist, from the top, of carbonate successions (Apennine Platform, outcropping in the Matese ridge), pelagic basin successions (Molise-Sannio Basin, outcropping to the N and E of the ridge). The top surface of Matese Ridge features karst topography characterized by several internally drained basins, such as the Matese Lake basin (Santangelo and Santo, 1991; Aucelli et al., 2013; Valente et al., 2018), and karst gorges, such as the Torano Stream (Lambiase and Ruggiero, 1980), which sinks underground to the east of San Gregorio Matese and emerges a few hundred meters downstream. Carbonates outcropping in Matese Ridge consist of inner platform to bypass and slope facies successions, separated by high-angle faults

that originally acted as normal faults in the Mesozoic, which were reactivated during Miocene shortening with minor reverse displacement (Calabrò et al., 2003). The thrust pile is dissected by NW-SE extensional structures and E-W trending high-angle faults generally showing left-lateral activity overprinted by either dip-slip or oblique right-lateral motion associated with reactivation during the Middle Pleistocene to Present tectonic regime (Mazzoli et al., 2000, and references therein). The area, including the southern Matese ridge and adjoining valleys, is affected by several extensional faults showing geomorphological-stratigraphical evidence of activity during the late Quaternary (Ascione et al., 2018). These structures control the formation of Quaternary continental basins including the Alife Basin. Many of the Quaternary faults in the Matese Ridge area show evidence of late Quaternary activity (Cinque et al., 2000, and references therein). In fact, the study area is located in the epicentral zone of multiple strong historical earthquakes. The most destructive events, with Mercalli-Cancani Sieberg intensities of X–XI, occurred in 1349, 1456, 1688 and 1805, and created ground effects such as surface faulting, sinkholes and landslides that led to thousands of casualties (Fig. 3.6). (e.g., Esposito et al., 1987; Gasperini et al., 1999; Michetti et al., 2000; Galli and Galadini, 2003; Di Bucci et al., 2005; Fracassi and Valensise, 2007; Porfido et al., 2007; Serva et al., 2007; Galli and Naso, 2009; Locati et al., 2011; Santo et al., 2011; Rovida et al., 2016).

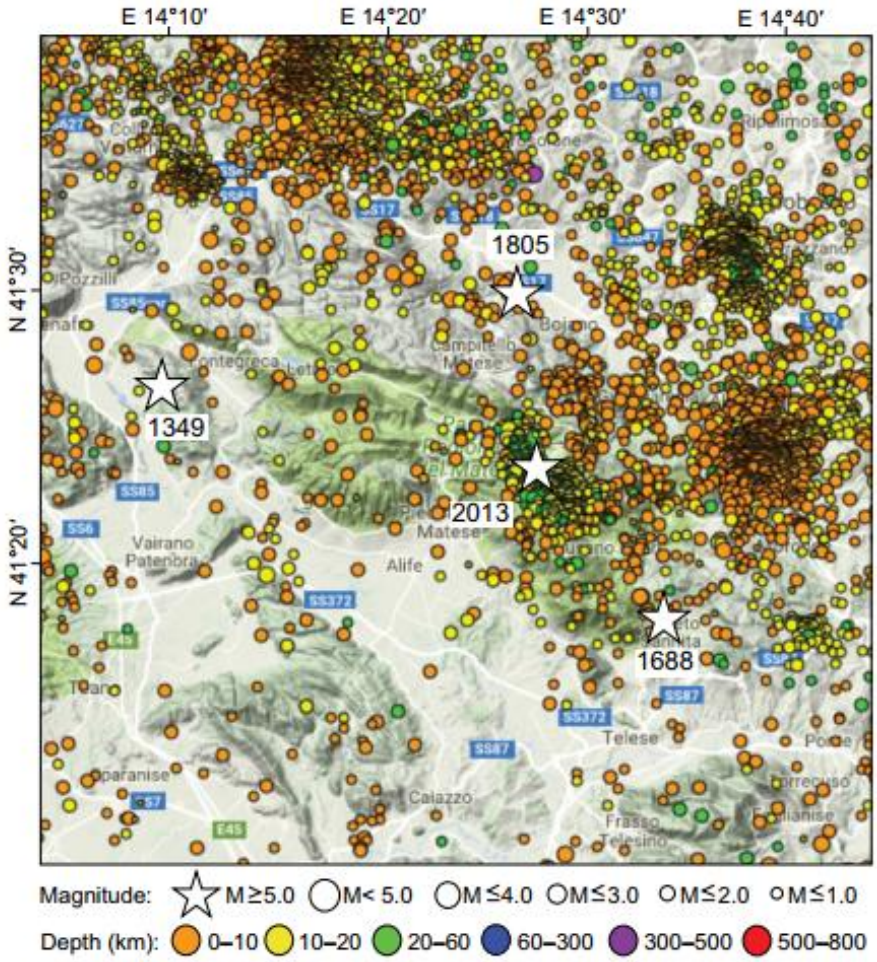

Figure 3.6 *Seismicity recorded from 1990 to the present (derived from the ISIDe database; http://isid.rm.ingv.it/iside) and locations of epicenters of strong historical earthquakes in the Matese ridge region, derived from Galli and Naso (2009) and the Parametric Catalogue of Italian Earthquakes 2015 (Rovida et al., 2016).*

The earthquakes of 1688 and 1805 were associated to seismogenic sources oriented NW-SE and NE, located to the north- eastern and northern border of the Matese ridge (Boschi et al., 1997; DISS Working Group, 2015). The earthquake of 1349 was associated to the SW-dipping Aquae Iuliae fault (Galli and Naso, 2009). Since 1805, the Matese area is affected by a deep seismicity with a rare number of earthquakes and seismic sequences (Alessio et al., 1990; Milano et al., 1999, Valensise and Pantosti, 2001; Milano et al., 2002; 2005; 2006). The last significant event was recorded on 29 December 2013, a moment magnitude (Mw) = 5.16±0.07 earthquake occurred. This earthquake was characterized by a normal fault

mechanism with a NE-oriented T-axis, which caused a series of coseismic surface effects including landslides and ground ruptures (Valente et al., 2018). During the latter event, the local population described the occurrence of a flame in an area very close to the epicentre of the earthquake, at the beginning of the main shock. This localized effect, commonly observed during earthquakes (Oddone, 1915), is frequent in those areas where strong gas emissions are detected (methane and/or hydrogen) (Ascione et al., 2014). In fact, to the south of Matese ridge there are numerous effects associated with the gas emission on the surface (surroundings of Ciorlano and Ailano villages; e.g. Googas, 2006) that may be associated with the localized rising of fluids. Such phenomena include: (i) mineral springs (e.g. Acqua Lete mineral water springs; Corniello et al., 1999) in the Pratella area; (ii) thermal springs in the Telese and Venafro areas (Italiano et al., 2000); (iii) calcareous tufa and travertine deposits (surroundings of Venafro and Telese), carbonates bearing a crustal signature (Ascione et al., 2014); and (iv) clusters of sinkholes formed in carbonate rocks (around Pratella and Telese), which are related to enhanced dissolution associated with fluids rising along active faults (Santo et al., 2011). A lot of structural information on the active fault system in the Matese area was recently obtained through the detection of anomalous emissions of different species of gas (CO_2, CH_4, Rn and He) along the fault lines. It can be concluded that these emissions indicate a strong gas leak along the active fault segments. This suggests that the active fault system of the Matese is composed of a complex network of fractures that connect surface faults to deeply rooted structures.

3.2.1 Spatial distribution of non-volcanic CO_2 emissions

The area of the southern Matese ridge is characterized by manifestation of natural gas spills, CO_2-dominant not affected by volcanic activity. The isotopic signature (i.e., 13C and 3He/4He) of the majority of non-volcanic gas emissions suggests that the

gas is primarily produced by a combination of upper mantle degassing and/or metamorphic decarbonation of marine limestones (Chiodini et al., 1999; Italiano et al., 2000; Chiodini et al., 2004; Minissale, 2004; Italiano et al., 2008; Caracausi et al., 2013). Current models of degassing in non-volcanic areas of the Apennines imply that the process occurs by a deep hot source and the progressive dehydration of the subducted Adriatic-Apulian plate (Chiodini et al., 2004; Frezzotti et al., 2009; Chiarabba and Chiodini, 2013; Chiodini et al., 2013). Also, mechanical energy released during seismic events has been recently proposed as a possible additional source of CO_2 due to friction-related heating and associated decarbonation processes (e.g. De Paola et al., 2011) in Apennines areas where the contribution of CO_2 degassing from the mantle is low (Italiano et al., 2008). Specifically, this study is focused on the high gas emissions occurring in areas surrounding the Ciorlano and Ailano villages. In particular, a very high density of gas vents covering areas from about 200 m to 2 km^2 in width has been identified in the Ailano area. Furthermore, the area between Ailano and Ciorlano is characterized by a dense distribution of gas vents and dolines, with the latter affecting both carbonate rocks and the overlying Quaternary deposits. This type of phenomenon is commonly interpreted as an indicator of intense alteration associated with the increase of fluids and correlated to the fluid-rock interactions that occur in depth preferentially along active faults (Annunziatellis et al., 2008; Santo et al., 2011). In particular, data obtained from geomorphological, structural and soil gas surveys indicate that the main Colle Sponeta fault scarp is characterized by a large number of gas vents recognized in the field by the scarce and/or total absence of vegetation, bubbling phenomena in the water sources and sinkholes related to strong CO_2 emissions (Fig. 3.7). The average value of CO_2 (6.81%) in the Colle Sponeta area is twice the average of the surveyed volcanic areas of Central and Southern Italy (3.33%). CO_2 and CO_2 flow maps in Ciorlano area (Fig. 3.8) indicate gas emissions located in a region that is sectioned by

a large number of faults. The alignments of the gas vents are consistent with the directions of the fault segments active during the late Quaternary. In particular, the high values of concentrations and flow of CO_2 in the Ciorlano area, which also correspond to high concentrations of He in the soil gas, clearly follow the Colle Sponeta fault scarp (Fig. 3.7).

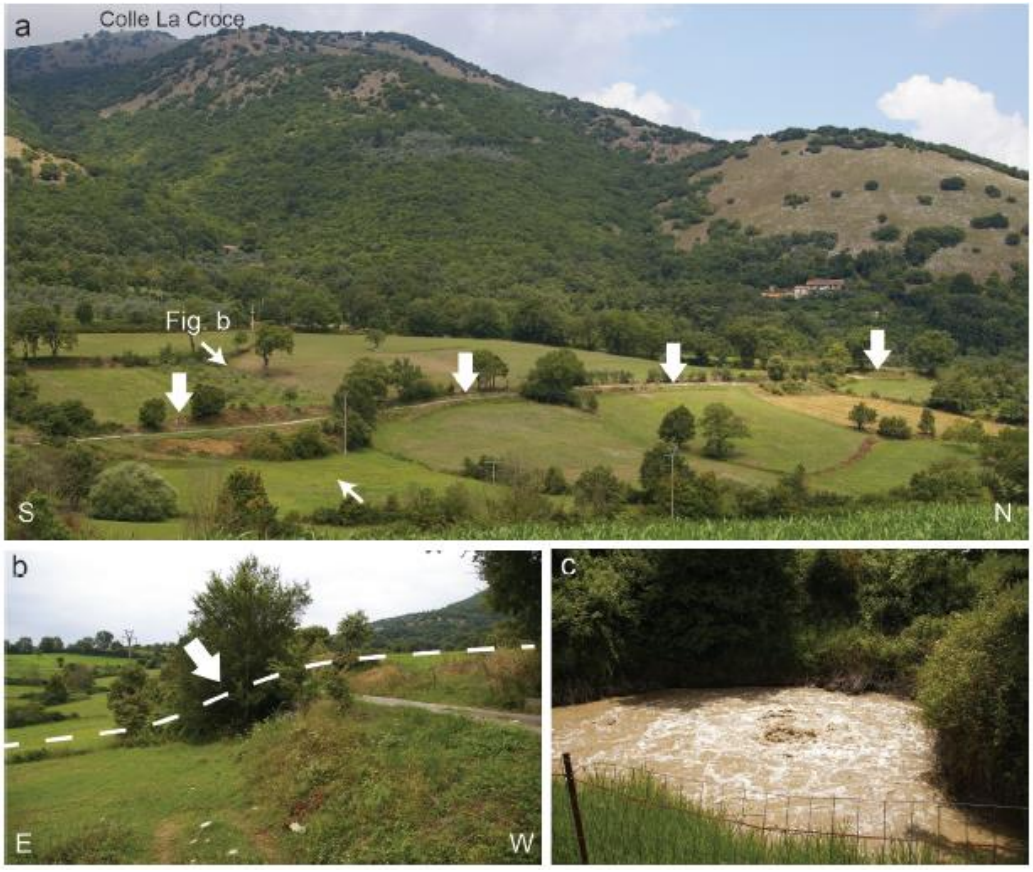

Figure 3.7 *Images of the Colle Sponeta area. (a) Frontal view (taken from the E) and (b) profile view (taken from the N) of the Colle Sponeta fault scarp. (c) Sinkhole with bubbling due to a free gas phase upwelling (from Ascione et al., 2018).*

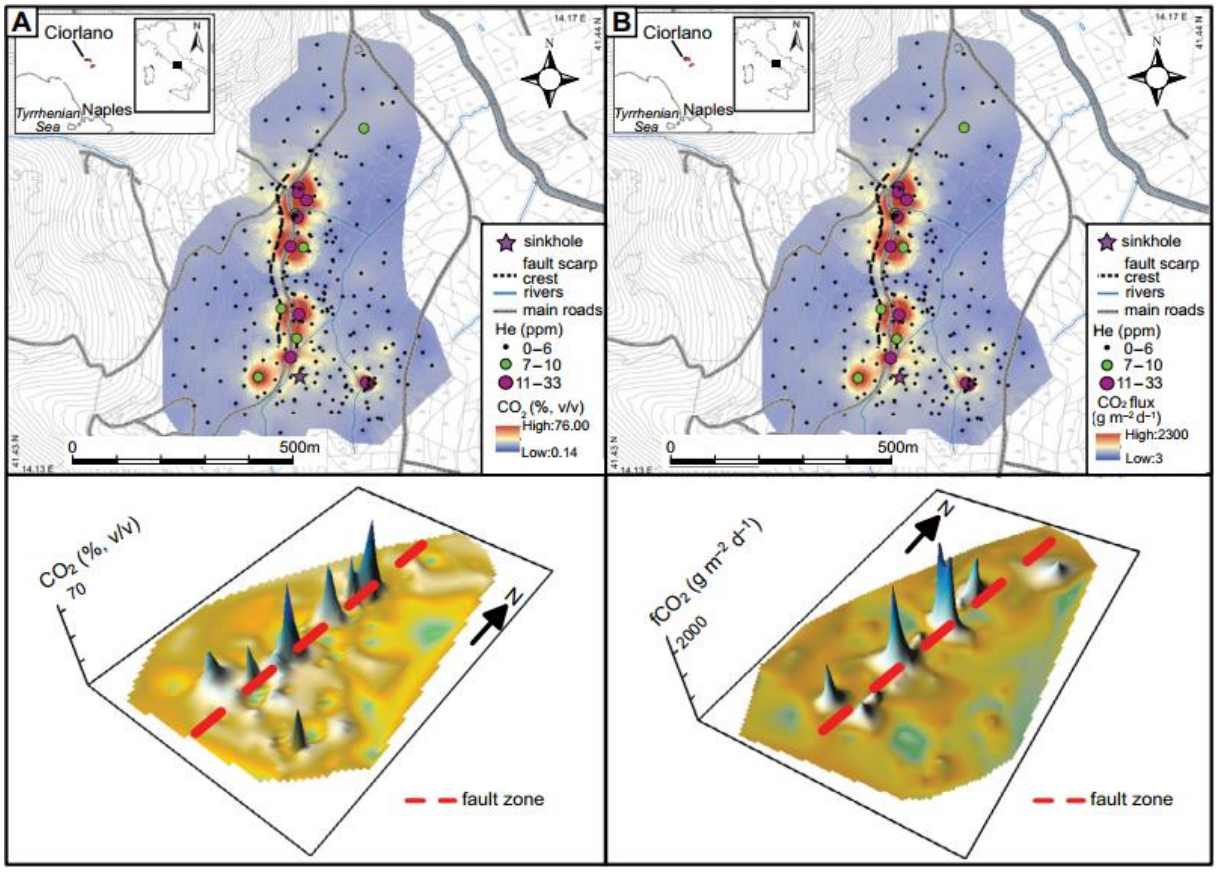

Figure 3.8 *2D and 3D spatial distribution of soil CO_2 concentration (A) and flow (B) at the Ciorlano site. The distribution of the CO_2 concentration and flux and the He concentration in the soil gas (violet and green circles, respectively) highlight anomalies aligned along the N-S Colle Sponeta fault scarp (from Ascione et al., 2018).*

These observations suggest that the gas vents, as well as the diffuse anomalous emissions, are strongly controlled by the fault network, which is able to sustain a high level of structural permeability along the fault direction. Noteworthy is the presence of high concentrations of He coupled with the high concentrations of CO_2 along the fault trace. These concentrations are rarely observed in non-volcanic districts and may suggest the presence of a wider degassing area connected to a deeply rooted active regional fault in the southern Matese area. Generally, CO_2 in soil gas has a wider area of anomalous values around the gas vent due to lateral diffusion effects induced by its greater density (Beaubien et al., 2014). This behavior allows the tracing of the fault that is permeable to the underlying gas. However, the CO_2 flow distribution shows very high anomaly values at the core of the gas vent

with respect to the surrounding area, and a fast decrease of the anomalous values outside the gas vent (Fig. 3.8B). This implies the occurrence of emissions in a restricted area around the core of the gas vent, where the geotechnical properties of the sediments have been locally compromised.

Chapter 4.

3D Geoelectrical reconstruction of fault zones

4.1 Ailano Area (Caserta, southern Italy)

The Ailano survey area is characterized by fluids and CO_2 leakage, as shown in Fig. 4.1. Several aligned sinkholes have been identified in the area (see Fig 4.1a, b, c) along the fault direction (yellow dashed line in Fig. 4.1a). The alignment is also identified by areas dried up by the leakage of CO_2 that occurs directly from the ground without giving rise to sinkholes (see dashed blue circle in Fig. 4.1d).

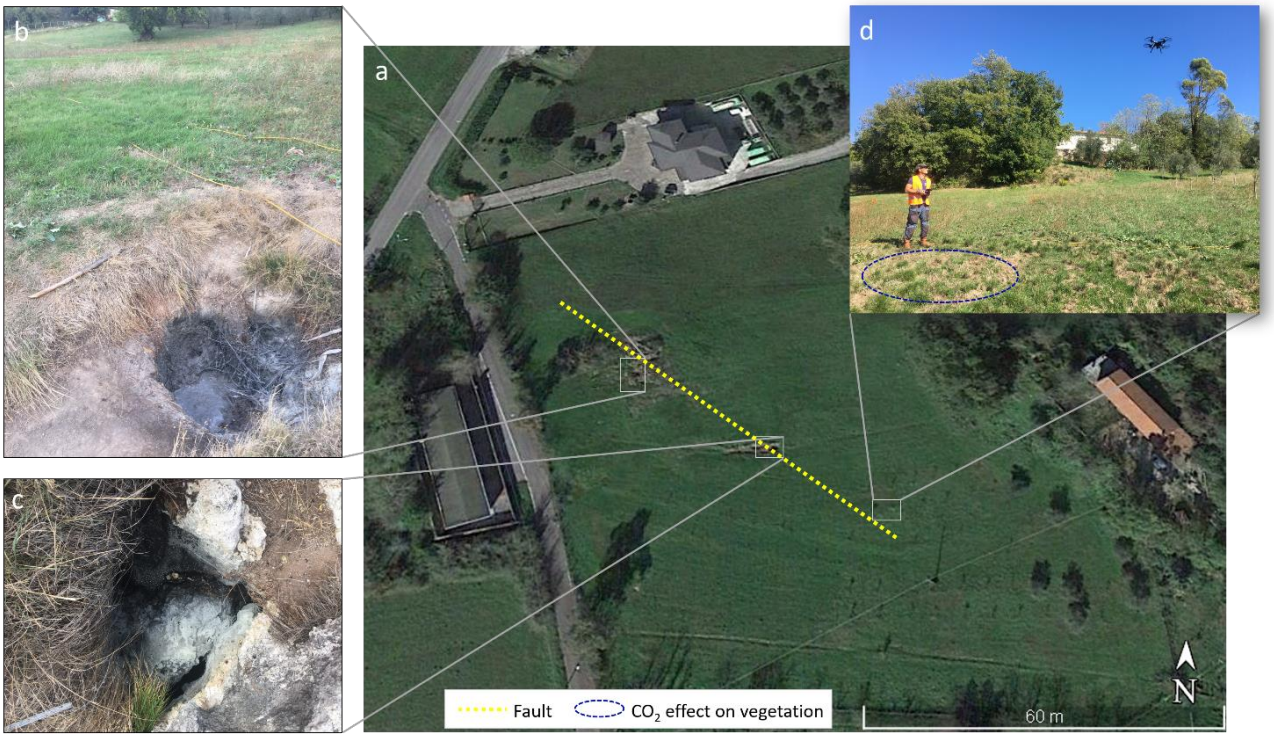

Figure 4.1 *a) Ailano survey area (Caserta, southern Italy), the dotted yellow line indicates the direction of the fault zone; b) and c): sinkholes with fluids and CO_2 leakage; d) area dried up by CO_2 leakage from the ground (dashed blue circle).*

The application of the proposed 3D ERT technique in this area was aimed at reconstructing the buried volume in the attempt to identify the active fault zones that control the release of significant CO_2 flows. Furthermore, 2D ERTs along the same profiles used for the 3D ERT survey were carried out for further calibration of the new technique.

4.1.1 Data collecting

The apparent resistivity data were collected using 4 parallel spreads of 48 electrodes with an electrode spacing of 2 m (Tab. 4.1) according to the target of the survey. The parallel lines, 22 m distant from each other, allowed to obtain a high-resolution 3D model with XYZ dimensions equal to (66 x 94 x 18) m^3 (Figs. 4.2, 4.3). Such an acquisition geometry was chosen for understanding what results this method could have guaranteed by using a small electrode spacing and a relatively large distance between the acquisition lines (about 10 times the electrode spacing).

Site	Array	Type of acquisition	Acquisition number	Electrode number	Quadrupole number	Electrode distance	Inter-line distance
Ailano (Caserta, southern Italy)	Pole-dipole	2D	4	48	1434	2 m	22 m
		3D	3	96	7722	2 m	22 m

Table 4.1 *Acquisition parameters for the 2D and 3D ERT surveys performed in the Ailano study area.*

The 3D ERT was implemented in three phases which involved the data acquisition between pairs of consecutive spreads as shown in Fig. 4.3, i.e. from Spread_1 to Spread_2, from Spread_2 to Spread_3 and from Spread_3 to Spread_4. In this way, each acquisition overlapped the adjacent spreading to ensure optimal coverage of the whole investigated area (66 m x 94 m). Each 3D acquisition was performed by a sequence consisting of 1006 current injections and 7722 measurement quadrupoles. The entire survey was completed in about 150 minutes, obtaining an investigation depth of about 18 m.

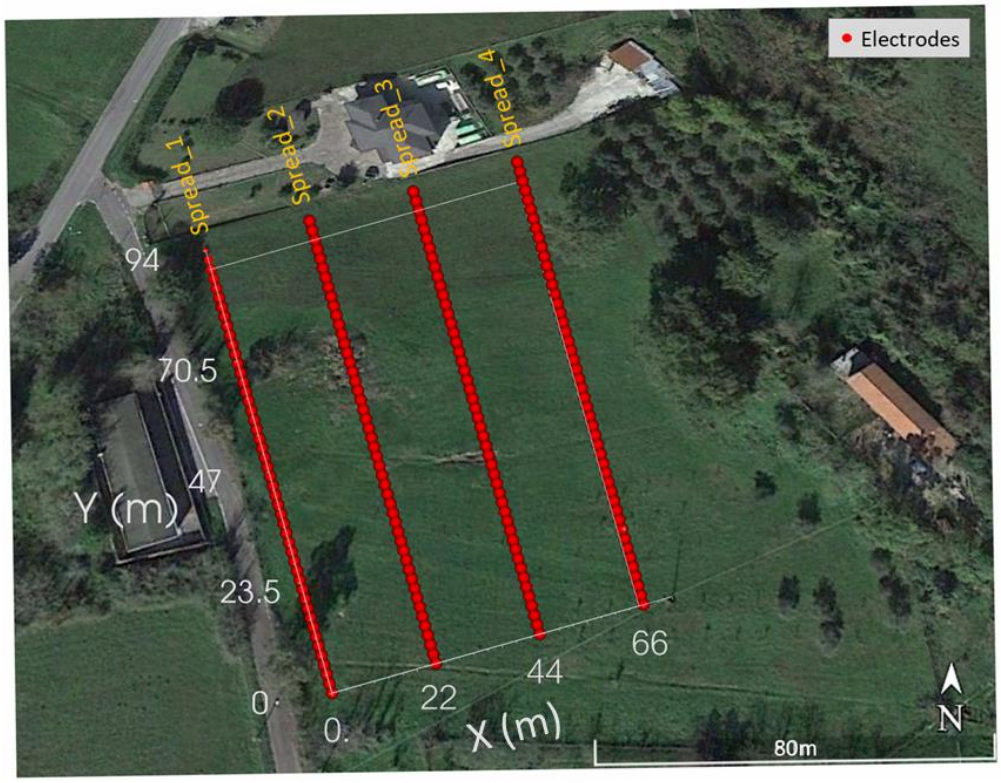

Figure 4.2 *Ailano survey area (Caserta, southern Italy). The red dotted lines indicate the parallel electrode spreads, 22 m apart, used for the 2D and 3D ERT surveys.*

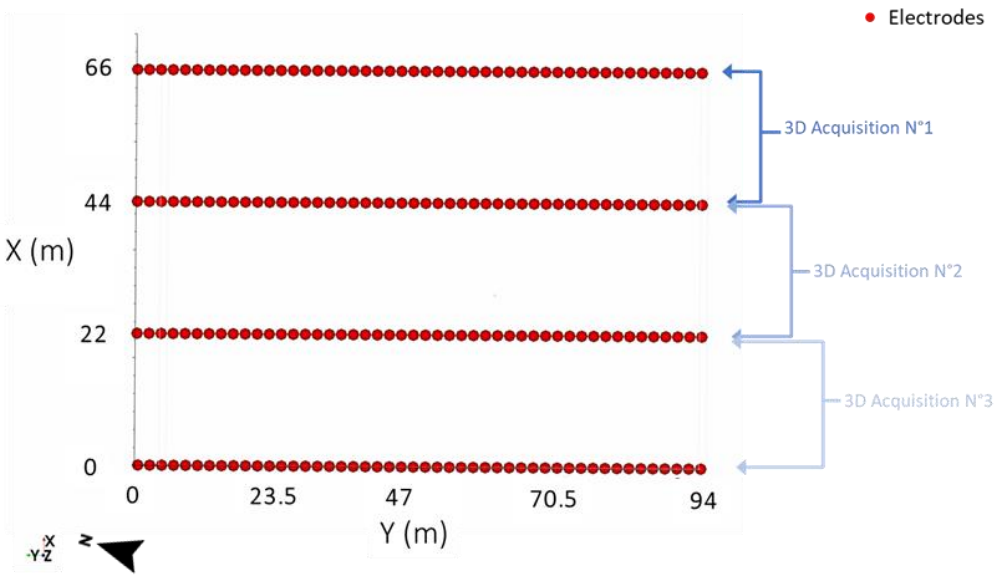

Figure 4.3 *Data acquisition scheme used for the 3D ERT survey in the Ailano area.*

The resulting dataset, consisting of about 23166 apparent resistivity values, was derived from the three separate runs and combined into a global 3D dataset for the final inversion process. The high number of collected data was make possible thanks

to the use of an *ad hoc* designed measurement sequence, which allows arbitrarily using the electrodes of each cable both as transmission and receiving devices (see par 2.1.2). Due to the high values of the measured voltages (on average about 100 mV) and the generally very low environmental noise, a very good signal-to-noise ratio was achieved.

As specified above, the four lines in Fig. 4.2 were also used for carrying out 2D ERT profiles aimed at further calibration of the new 3D data acquisition scheme. Each 2D ERT profile, lasted about 15 minutes, was performed by an acquisition sequence consisting of 198 current injections and 1434 measurement quadrupoles.

4.1.2 3D geophysical modeling of the Ailano area

The acquired data were processed following the Occam inversion approach, implemented by the ERT-Lab_64™ software (see par. 2.1), which produces a smooth model that fits a data set within certain tolerances, for deriving the smoothest model consistent with the acquired data in presence of strong resistivity contrasts between the features of interest and the hosting medium (Constable et al. 1987; Francese et al. 2009). Therefore, different tests were made by changing the dimension of the three-dimensional mesh used by the software for considering the spatial variability of the investigated physical parameter in the Ailano area. The best results were obtained for a regular mesh with dimensions: x = 4 m, y = 4 m, z = 4m (Fig. 4.4).

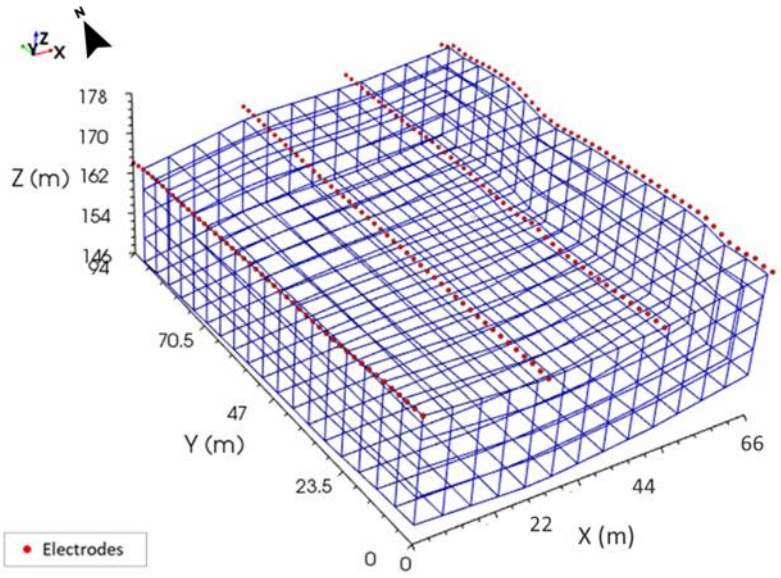

Figure 4.4 *3D mesh of the investigation volume (foreground region) used for the inversion of the 3D ERT survey carried out in the Ailano area.*

Fig. 4.5 shows the obtained inversion results. As it can be seen, the whole investigated volume is characterized by resistivity values, ρ, ranging from 0.50 Ωm to 100 Ωm. Based on the lithology of the survey area, the range 0.50 Ωm ≤ ρ ≤ 15 Ωm (blue volume in Fig. 4.5a) can be associated with the presence of a clay layer (C in Fig. 4.5a) that in some sectors reaches a thickness of about 10 m from the surface level; the range 20 Ωm ≤ ρ ≤ 40 Ωm (green volume in Fig. 4.6a) may be related to the presence of an aquifer (W in Fig. 4.6a), whose top is located about 8 m from the surface level and deepens up to the maximum investigation depth; finally, the range 70 Ωm ≤ ρ ≤ 100 Ωm (red volume in Fig. 4.6b) could be ascribed to the presence of a volume of CO_2 (G in Fig. 4.6b); this anomaly is located below the sinkholes visible in the field and is confined to the maximum exploration depth and reach in some points the surface level.

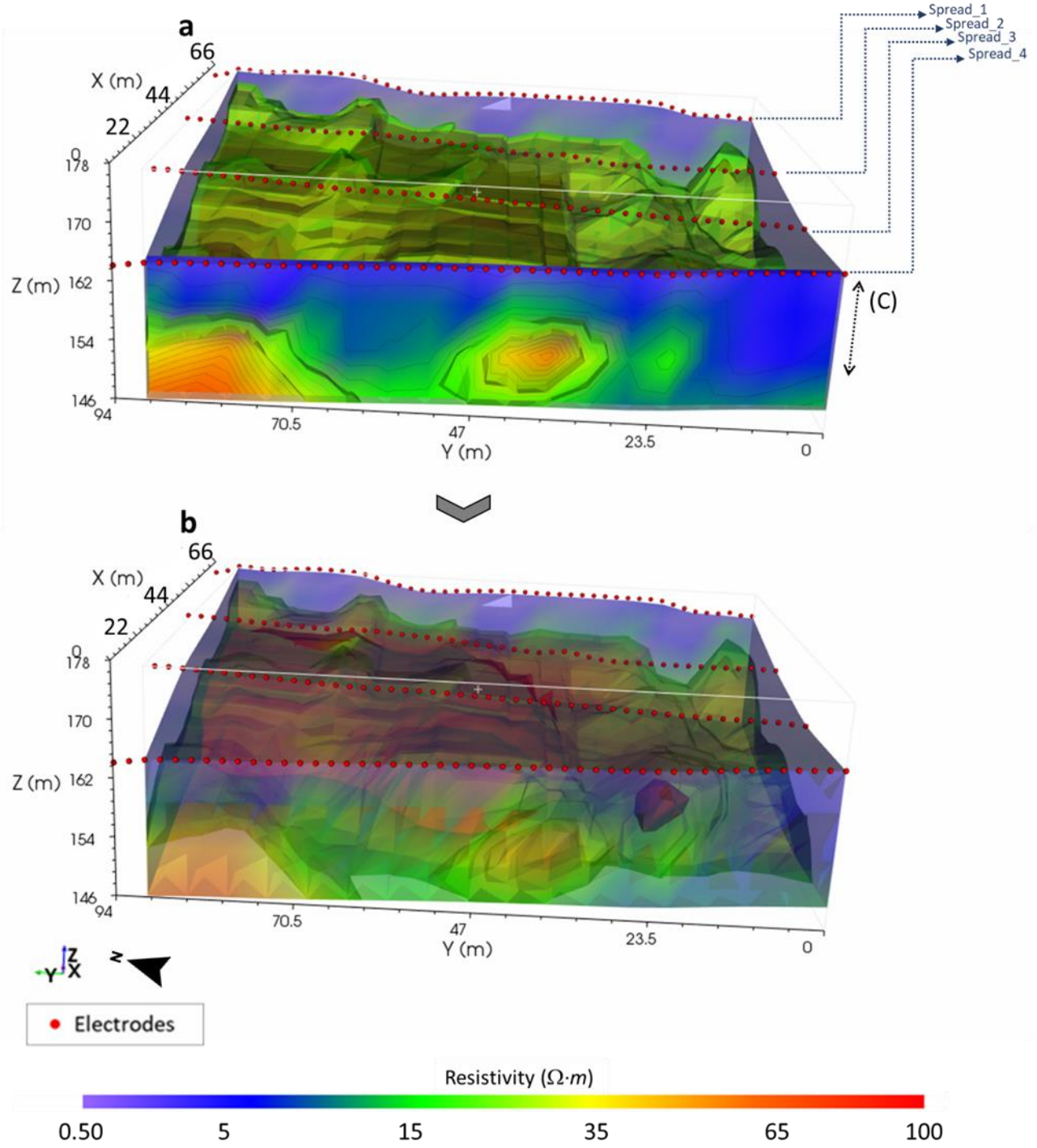

Figure 4.5 *Inversion results of the high-resolution 3D electrical resistivity tomography performed in the Ailano survey area. a) Resistivity volumes in the range 0.50 Ωm ≤ ρ ≤ 100 Ωm; b) resistivity volumes in the range 10 Ωm ≤ ρ ≤ 100 Ωm.*

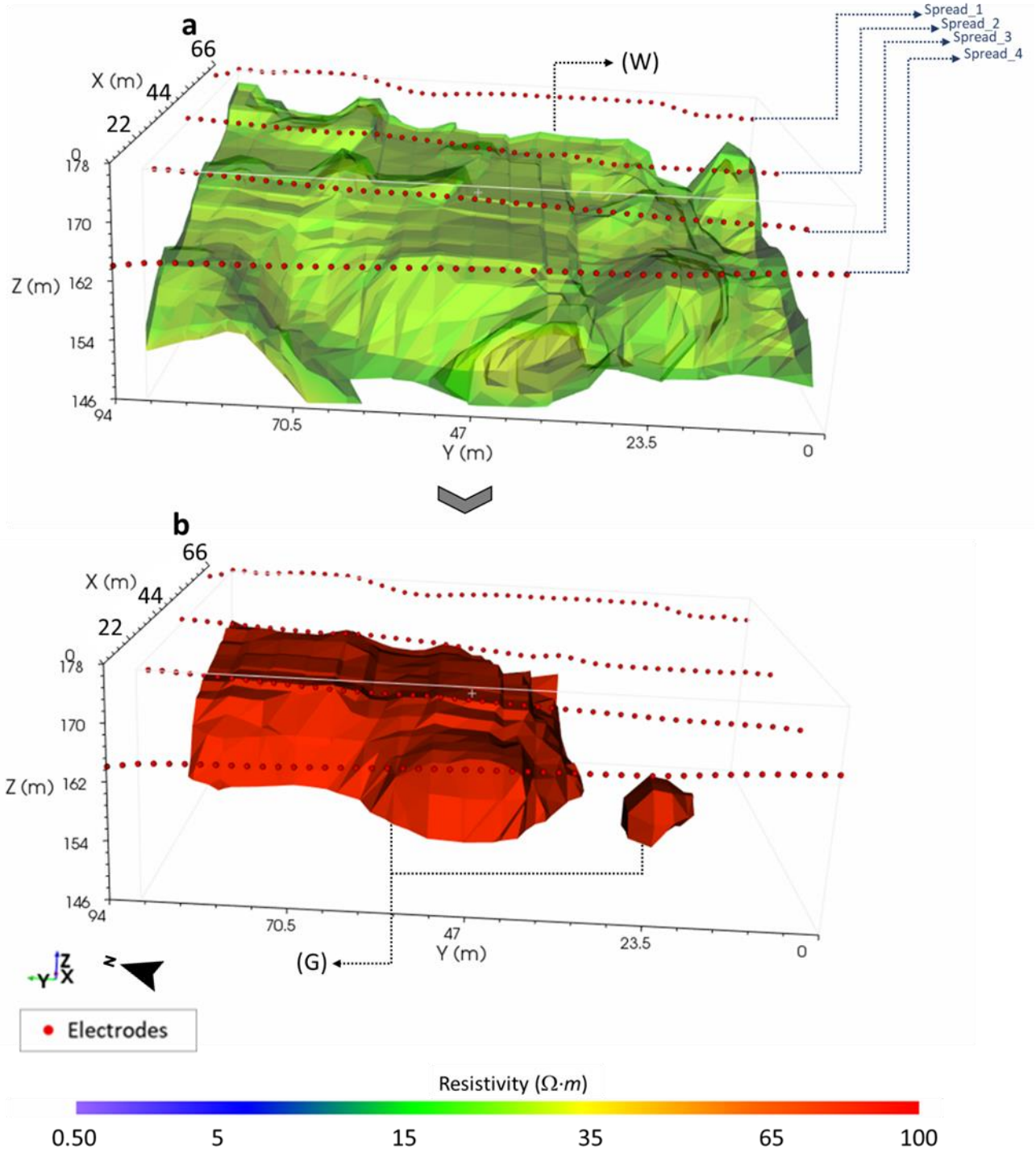

Figure 4.6 *Inversion results of the high-resolution 3D electrical resistivity tomography performed in the Ailano survey area. a) Resistivity volumes in the range 20 Ωm ≤ ρ ≤ 40 Ωm; b) resistivity volumes in the range 70 Ωm ≤ ρ ≤ 100 Ωm.*

It is worth noticing that the images in Figs. 4.5 and 4.6 suggest that the chosen 3D acquisition geometry is not particularly suitable in this geological context. In fact, the choice of a small electrode spacing (2 m) does not seem to have guaranteed,

contrary to what happens in other contexts, a good near surface resolution probably caused by a conspicuous presence of fluids and CO_2, which tend to saturate the shallow current flow paths generated by the used electrode arrangement. In fact, under these conditions, it is not possible to discriminate small local concentrations of CO_2 or to obtain information on fault structures.

4.2 Ciorlano area

The survey site in the Ciorlano area extends from NW to SE across the southern part of the Colle Sponeta fault (Fig. 4.7), and it is located north of the area called by local farmers "Soffione di Ciorlano", i.e. a sinkhole with bubbling phenomena (shown as a star in Fig. 4.7).

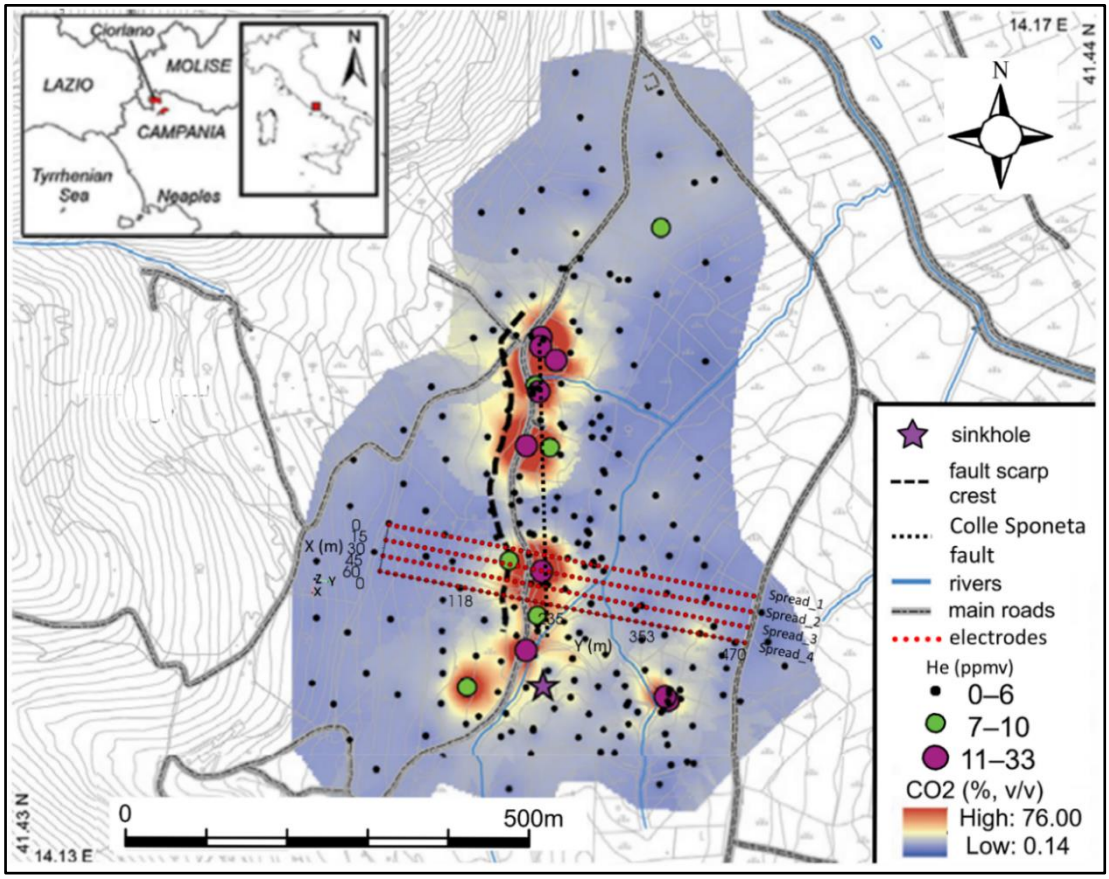

Figure 4.7 *Ciorlano survey area (Caserta, southern Italy). The red dotted lines indicate the parallel electrode spreads, 20 m apart, used for the 3D ERT survey; the black dotted line indicates the Colle Sponeta fault (modified after Ascione et al., 2018).*

Based on the results from the 3D ERT survey in the Ailano area , in this case study, a large electrode spacing and a relatively small distance between the acquisition lines (about 2 times the electrode spacing) were used for the data acquisition geometry. This choice aimed to detect local shallow CO_2 concentrations and to model fault structures up to investigation depths of about 100 m b.g.l..

4.2.1 Data collecting

The apparent resistivity data were collected using 4 parallel spreads of 48 electrodes with an electrode spacing of 10 m (Tab. 4.2), according to the target of the survey. The parallel lines, 20 m distant from each other, allowed to obtain a high-resolution 3D model with XYZ dimensions equal to (60 x 470 x 105) m^3 (Fig. 4.8).

Site	Array	Type of acquisition	Acquisition number	Electrode number	Quadrupole number	Electrode distance	Inter-line distance
Ciorlano (Caserta, southern Italy)	Pole-dipole	2D	4	48	1337	10 m	20 m
		3D	3	96	10722	10 m	20 m

Table 4.2 *Acquisition parameters for the 2D and 3D ERT surveys performed in the Ciorlano study areas.*

Figure 4.8 *Ciorlano survey area (Caserta, southern Italy). The red dotted lines indicate the parallel electrode spreads, 20 m apart, used for the 2D and 3D ERT surveys; the yellow triangles indicate the location of two HVSR surveys (T1 and T2, respectively).*

The 3D ERT survey was implemented in three phases which involved the data acquisition between pairs of consecutive spreads as shown in Fig. 4.9. Therefore, each acquisition overlapped the adjacent spreading to ensure optimal coverage of the whole investigated area (60 m x 470 m).

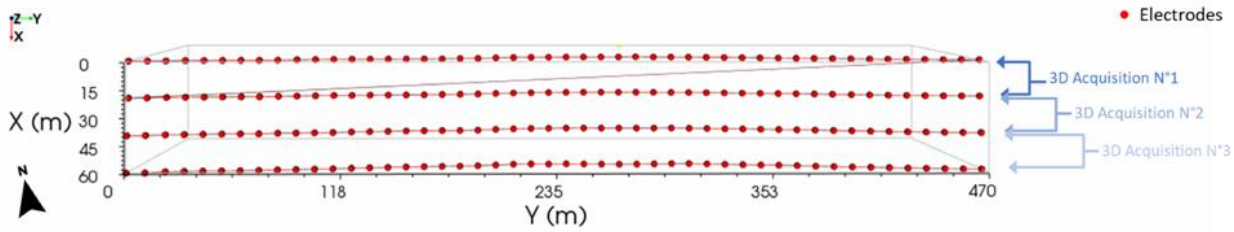

Figure 4.9 *Data acquisition scheme used for the 3D ERT survey in the Ciorlano area.*

In order to get a high resolution compared with the Ailano survey, the acquisition sequence parameters were changed for increasing the number of both current injections and measurement quadrupoles.

Each 3D acquisition was performed by a sequence consisting of 1116 current injections and 10722 quadrupoles. The necessary time to complete each 3D acquisition was around 50 minutes. The resulting dataset, consisting of about 32000 apparent resistivity values, was derived from the three separate runs and combined into a global 3D dataset for the final inversion process. The high number of well-distributed measurements (Fig. 4.10) allowed to obtain high resolution and an investigation depth around 105 m (Fig. 4.11).

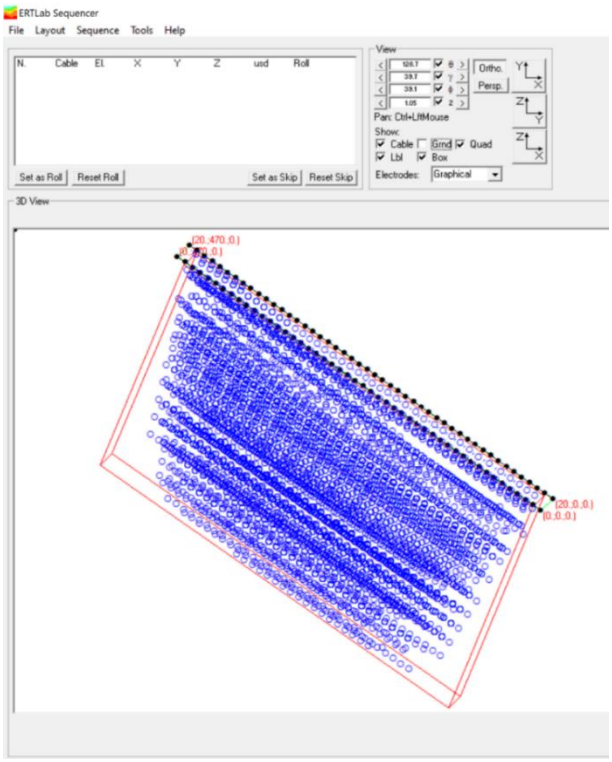

Figure 4.10 *3D ERT acquisition sequence used for the Ciorlano survey area. Black and blue dots indicate the positions of electrodes and quadrupoles, respectively (by ERT-Lab Sequencer Software, GeoStudi Astier, Livorno).*

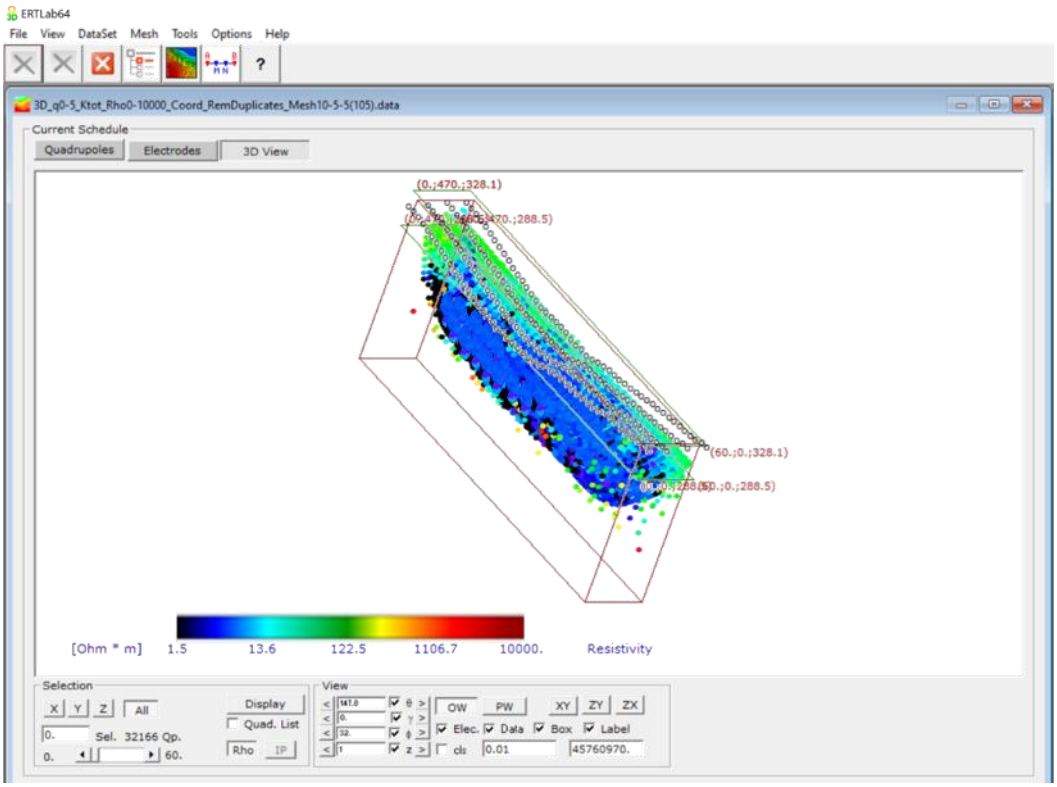

Figure 4.11 *Distribution of the apparent resistivity values acquired for the 3D ERT survey in the Ciorlano area.*

2D ERT profiles were also performed along the 4 alignments in Fig. 4.9 for the purpose of futher calibration of the proposed 3D data acquisition scheme. Each 2D ERT profile was realized by an acquisition sequence consisting of 198 current injections and 1337 measurement quadrupoles. A very short time (about 10 minutes) was needed for each 2D tomography thanks to the appropriate optimization of the data acquisition sequence and the use of the pole-dipole array, which allowed to exploit the characteristics of the Syscal Pro georesistivimeter in simultaneous measurements from up to 10 multi-channels.

4.2.2 3D geophysical modeling of the Ciorlano area

For the Ciorlano survey area, where two main lithologies characterized by a net contrast in their electrical properties (highly resistive outcropping carbonates and very conductive clays) are present, particular care was needed in choosing the initial guess model before starting the iterative procedure (see par. 2.1). Specifically, the 3D ERT data inversion was tested starting from 0.5 to 300 Ωm according to the DOI (depth of investigation) approach. The term DOI refers to ‘‘the depth below which surface data are insensitive to the value of the physical property of the earth’’ (Oldenburg and Li, 1999). In other words, this is the depth below which the earth structure is no longer constrained by the data, but the outlined features are artefacts of the inversion process. For the Ciorlano area, the depth of investigation was highlighted by means of a function obtained by the ratio of different resistivity distributions derived from different starting models. The final result provided by the ERT-Lab_64™ software was obtained starting from an initial homogeneous model of 100 Ωm, which represents the apparent resistivity value with the highest count in the global histogram of Fig. 4.12 and a good sensitivity to explore down to 80-100 m depth. The iterative process was stopped when the difference between consecutive root-mean square (RMS) errors was less than 5%. As there are no evident anthropic

disturbances, the noise level was referred to measurement errors or 3D structure effects (Viero et al., 2015).

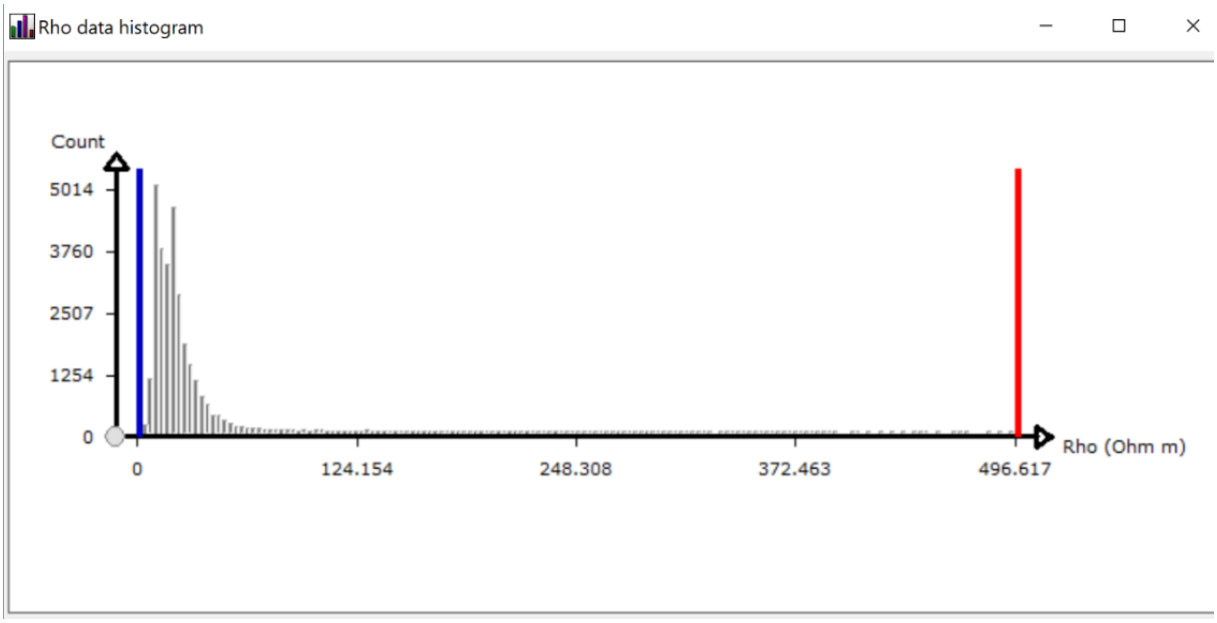

Figure 4.12 *Pre-processing phase of the ERT datasets: distribution of the apparent resistivity values recorded along pseudosections; the blue and red bars indicate, respectively, the minimum and maximum limits of the resistivity range selected by the operator to perform the data filtering.*

It is worth highlighting that the best inversion results were obtained for a regular three-dimensional mesh with dimensions: x = 2.5 m, y = 2.5 m, z = 2.5m (Fig. 4.13), which is smaller than that used for the Ailano 3D ERT survey. This choice was made possible by the lower ratio between the electrode spacing and the spread distance used for the Ciorlano survey, which favored a better model resolution in this specific geological context.

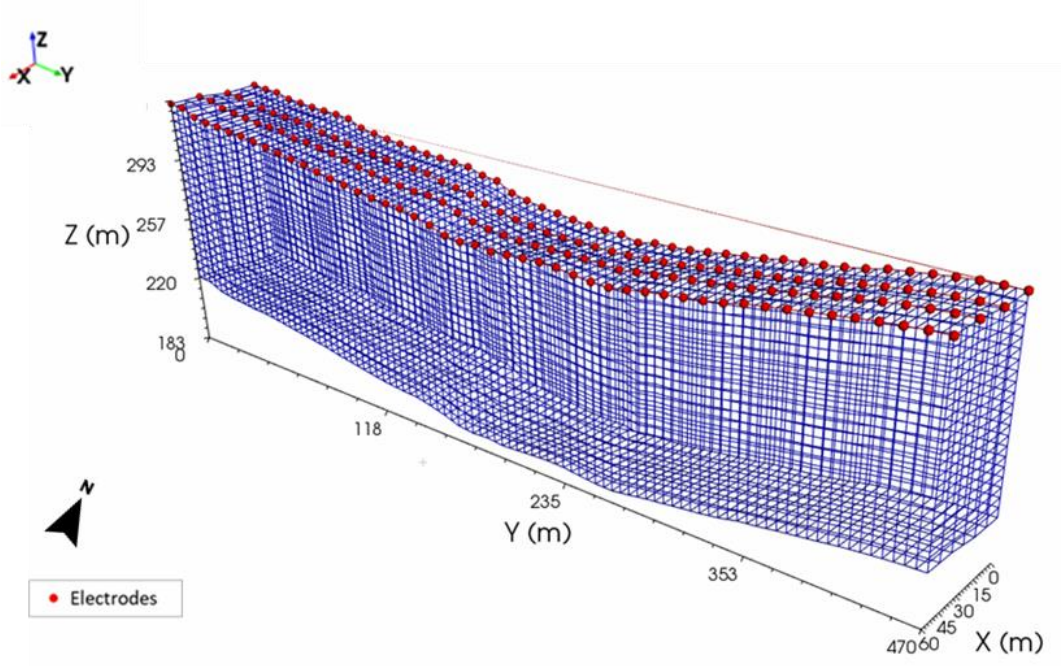

Figure 4.13 *3D mesh of the investigation volume (foreground region) used for the inversion of the 3D ERT survey carried out in the Ciorlano area.*

Fig. 4.14 shows the obtained inversion results. As it can be seen, the whole investigated volume is characterized by resistivity values, ρ, ranging from 1.50 Ωm to 10000 Ωm (Fig. 4.14a). Based on the lithology of the survey area, the range 1.50 Ωm ≤ ρ ≤ 20 Ωm (blue volume in Fig. 4.14) can be associated with the presence of a clay layer that, in the easternmost part, reach a thickness of about 60 m b.g.l. (C1 in Fig. 4.14b). Within this layer, more resistive patterns are observed (30 Ωm ≤ ρ ≤ 70 Ωm, green volume in Figs. 4.14b and 4.15a) potentially attributable to CO_2 migration paths, which would cause an increase in the resistivity values (Revil et al., 1999; Byrdina et al., 2009) in the easternmost part of the survey area, between 60 m and 70 m from the surface level (C2 in Fig. 4.15a). Finally, the range 1000 Ωm ≤ ρ ≤ 2000 Ωm (red volume in Figs. 4.14b and 4.15) is likely ascribable to the presence of CO_2 inside a fractured limestone mass located in the central part of the investigated volume, between 60 m and 70 m from the surface level (G in Fig. 4.15a). Such hypothesis is also supported by the presence of a small sinkhole, with groundwater

bubbling phenomenon due to CO_2 leakage, clearly visible on the field, at the time of the survey, in correspondence with lines 3 and 4 (S in Fig. 4.15a). This phenomenon is likely due to the contact between aquifer and CO_2, the latter coming from fractures of the carbonate basement whose top (1000 Ωm ≤ ρ ≤ 10000 Ωm) has been identified in the central part of the investigated area, at a depth of about 60 m from the surface level (B in Fig. 4.15b). Whilst, in correspondence of the progressives 210 m and 385 m along the Y axis, the top of the basement appears more superficial, specifically at a depth of about 70 m from the ground level (s. Fig. 4.15b). Therefore, the electro-layer recognized as a carbonate basement would be characterized by a structural high.

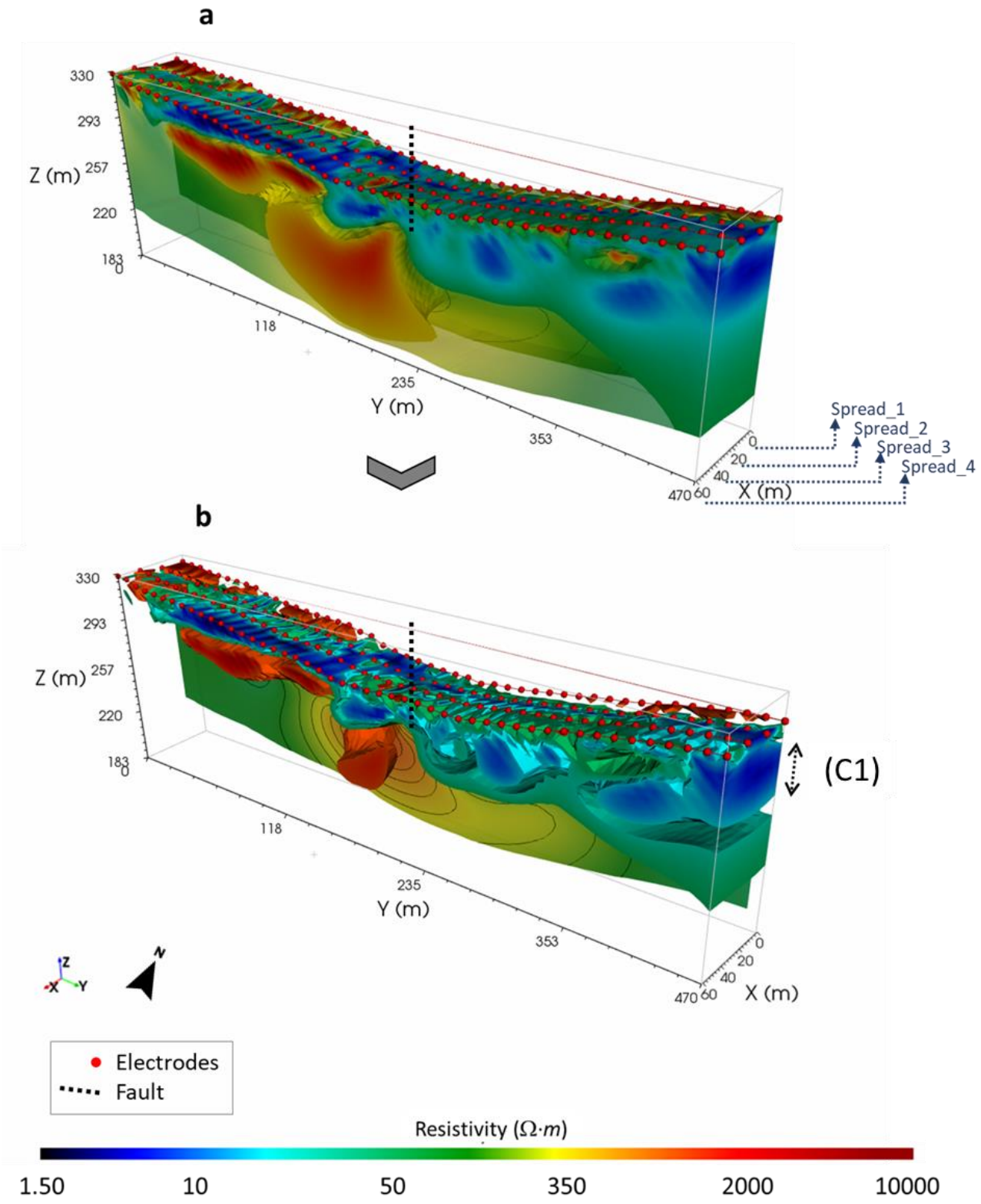

Figure 4.14 *Inversion results of the high-resolution 3D electrical resistivity tomography performed in the Ciorlano survey area. a) Resistivity volumes in the range 1.50 Ωm ≤ ρ ≤ 10000 Ωm; b) resistivity volumes in the ranges 1.50 Ωm ≤ ρ ≤ 20 Ωm, 30 Ωm ≤ ρ ≤ 70 Ωm and 1000 Ωm ≤ ρ ≤ 2000 Ωm.*

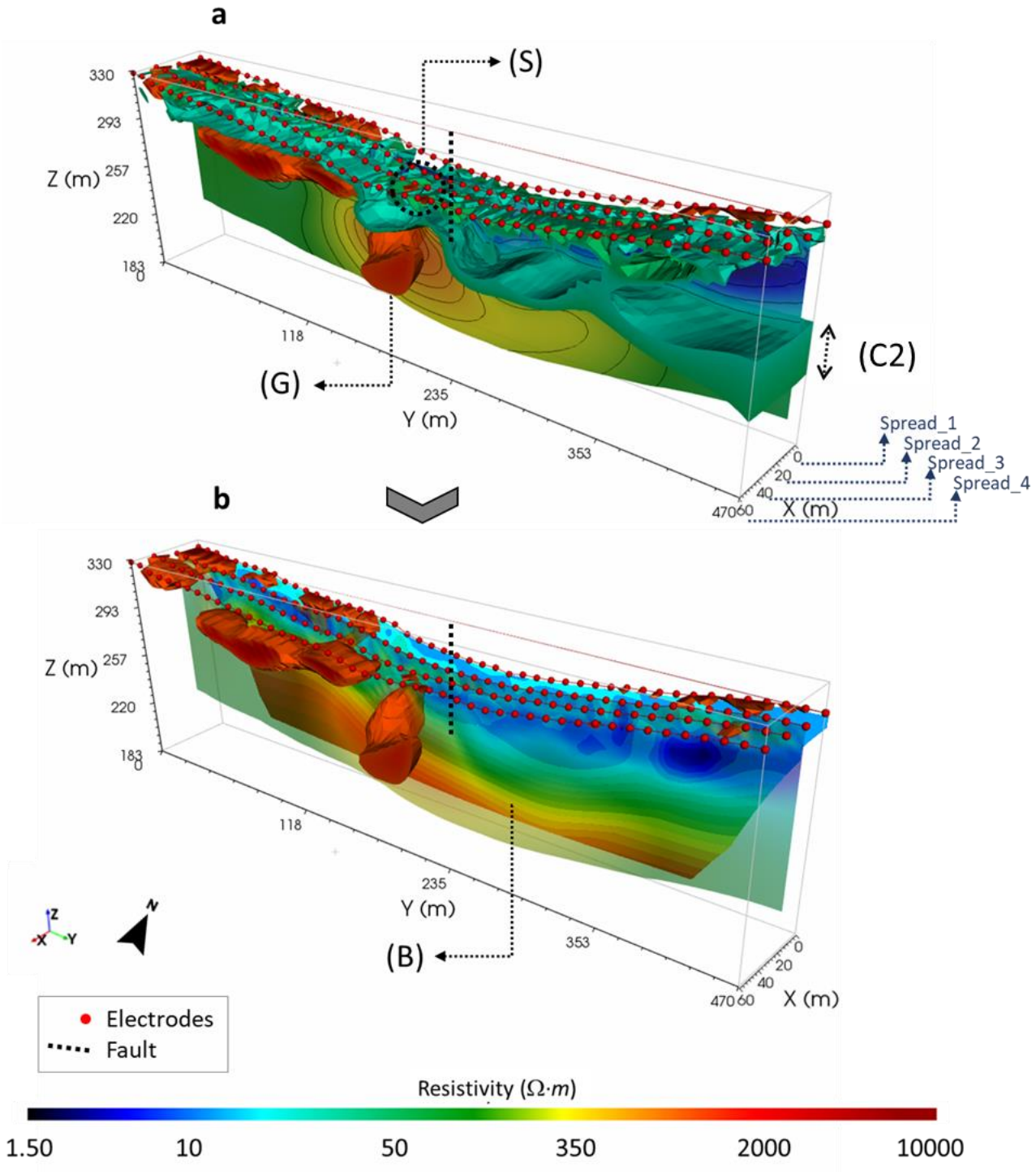

Figure 4.15 *Inversion results of the high-resolution 3D electrical resistivity tomography performed in the Ciorlano survey area. a) Resistivity volumes in the range 30 Ωm ≤ ρ ≤ 70 Ωm and 1000 Ωm ≤ ρ ≤ 2000 Ωm; b) resistivity volumes in the range 1000 Ωm ≤ ρ ≤ 2000 Ωm.*

The high-resolution of the 3D ERT survey in the Ciorlano area also highlighted the possible in-depth geometry of the fault structure. Indeed, by cutting the resistivity

volume in Fig. 4.14 (or Fig. 4.15) according to slices at different altitudes along the Z axis (Fig. 4.16), the resistive-conductive contact, that is observed near the progressive 235 m along the Y axis (Fig. 4.16d), could be indicative of the fault path, which appears clearly identified in the depth range from 34 m to 84 m from the ground surface (Figs. 4.14 and 4.15). In this regard, it is worth noticing that the fault is well identified as the center line of a resistive zone at about 70 m b.g.l. (altitude 246 m, Fig. 4.16a). Instead, at a depth of 20 m from the surface level (altitude 296 m, Fig. 4.16d) the fault is detected as the center line of an inhomogeneous conductive zone, where the less conductive sectors could suggest the presence of fractures filled by CO_2.

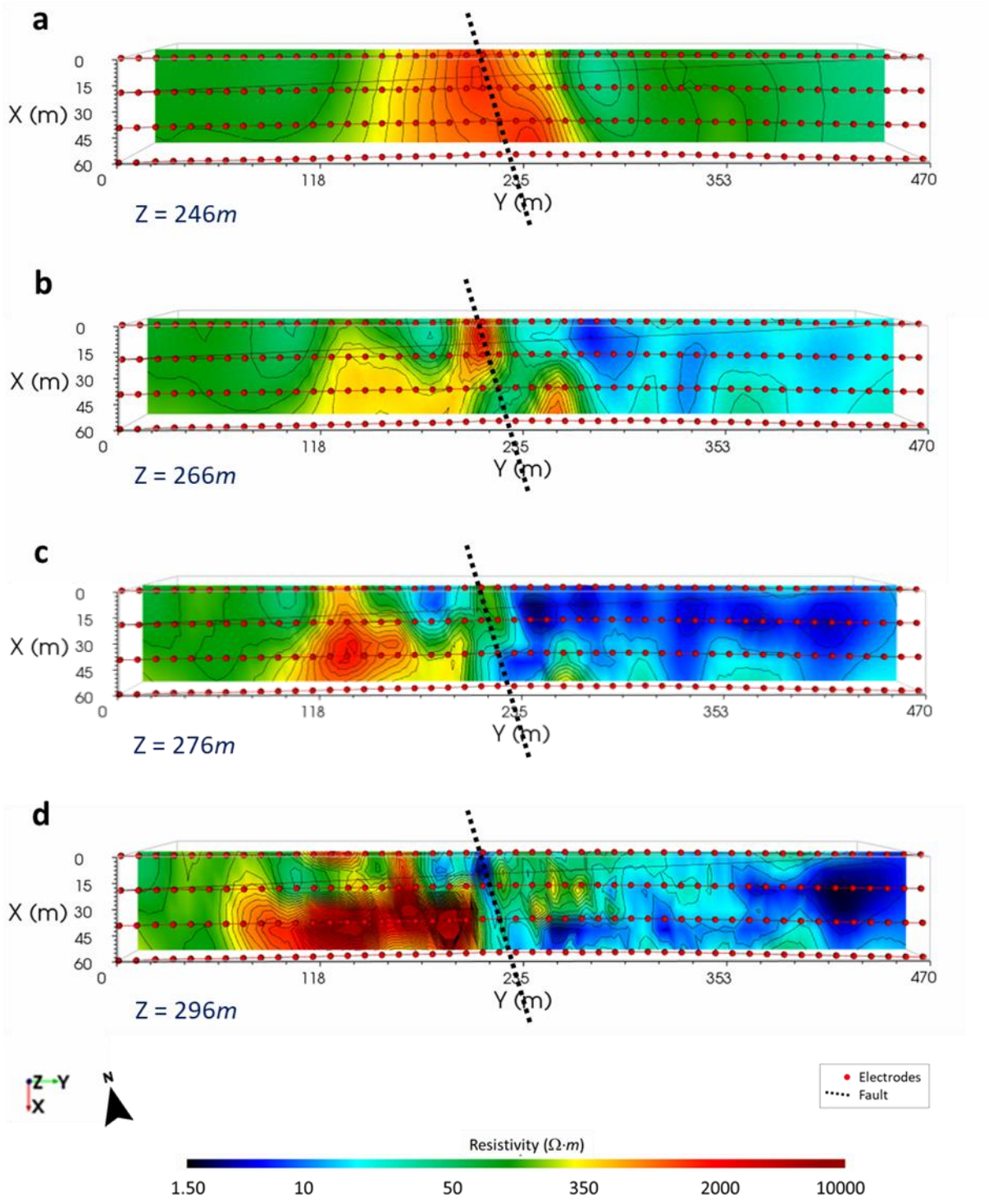

Figure 4.16 *Inversion results of the high-resolution 3D electrical resistivity tomography performed in the Ciorlano survey area, which are shown by cuts at different altitudes along the Z axis: a) slice Z = 246 m; b) slice Z = 266 m; c) slice Z = 276 m; d) slice Z = 296 m.*

4.2.3 Validation of resistivity data through comparison with passive seismic data (HVSR)

As seen in par. 4.1.2, the 3D ERT inversion results for the Ailano area have shown that the use of a small inter-electrode distance (s. Tab. 4.1) did not favour high-resolution modeling. In fact, a single resistive block, ascribable to saturated clayey material, and a central high-resistivity anomaly, likely correlated to CO_2 concentration, are clearly visible (s. Fig. 4.6). Whilst, no resistivity anomalies related to stratigraphical features and/or to any preferential pathways of the fluid leakage were highlighted. Therefore, for the second survey carried out in the Ciorlano area, a larger inter-electrode spacing and a smaller distance between two consecutive parallel lines were adopted (s. Tab. 4.2). This choice provided a very good resolution of the investigated subsurface that allowed us to correlate the observed resistivity anomaly distributions to fluids and CO_2 paths, as well as to the morphology of the fractured carbonate basement.

To validate our interpretative hypotheses, passive source seismic soundings were performed by using the Horizontal to Vertical Spectral Ratio (*HVSR*) technique (Bonnefoy-Claudet et al., 2006a, b). This method consists of passive measurements of environmental seismic noise, which is represented by small-amplitude continuous oscillations due to the superposition of effects generated both by natural sources (large-scale weather perturbations, wind, ocean waves, etc.) and anthropic sources (vehicular traffic or industrial activities). The H/V analysis (the ratio between the absolute values of the horizontal, *H*, and vertical, *V*, spectra) allows to identify the contrast between acoustic impedances in two adjacent layers. Sediments above a bedrock will give a peak in the H/V function (Haefner et al., 2010 and reference therein). However, even a fine sediment cover on the top of a gravel layer could generate a resonance and, therefore, a maximum in the H/V function (Parolai et al., 2002 and reference therein). In this case, the gravel layer is usually referred to as a

bedrock-like layer (i.e. comparable to the bedrock) even if its velocity (i.e. the propagation velocity of S waves, *Vs*, inside it) is less than 800 m/s (s. Tab. 4.3). These bedrock-like layers are able to generate wave entrapment phenomena, and therefore resonance phenomena, if the *Vs* discontinuity is clear. From the resonance frequency measurement, it is then possible to obtain a Vs estimate of the sediments (Castellaro et al., 2016), provided that the depth of the layer is known, or vice versa.

In addition to specific software, in order to transform a H/V curve into a *Vs* profile a constraint is needed, which is normally derived from the depth, *h*, of the contact between different lithologies, known from direct tests such as penetrometers or soundings. Without any constraint, there would be infinite models (that is, infinite Vs-h combinations) that could satisfy the same H/V curve. Approximate values of *Vs* velocity are shown in Tab. 4.3.

Soil types	Vs min (m/s)	Vs medium (m/s)	Vs max (m/s)
Very hard rocks (very fractured metamorphic rocks	1400	1620	---
Hard rocks (granites, igneous rocks, conglomerates, sandstones and shale medium fractured	700	1050	1400
Gravelly soils and soft / hard rocks (soft sedimentary rocks, sandstones, shales, gravels and soils with more than 20% gravels)	375	540	700
Compact clays and sandy soils (weak/very compact sands, silt and silty sandy clays, medium compact clays)	200	290	375
Soft soils (landfield in groundwater, soft clays)	100	150	200

Table 4.3 *Characteristic values of propagation velocity of the S waves in various soil types (Borcherdt, 1994).*

In the Ciorlano area, two HVSR acquisitions were carried out as shown in Fig. 4.8. To constrain the first contact between lithologies, the stratigraphy relative to a neighbouring survey was used (Fig. 4.17).

Figure 4.17 *Results from direct tests carried out in an area adjacent to the test site of Ciorlano. a) Survey stratigraphy; b) cataloguing box from 5.00 m to 10.00 m from the ground level; c) cataloguing box from 25.00 m to 30.00 m from the ground level.*

In the simple case of a homogeneous layer on a bedrock, the value of Vs30 can be calculated by measuring the resonance frequency if the depth *h* of the bedrock (or bedrock-like) given by direct measurements is known. In the case of multi-layer terrain, as for the Ciorlano survey area, the value of Vs30 is calculated based on the reconstructed velocity profile by the formula: Vs30 = 30/Σ(hi/Vsi) [m/s]. For the two HVSR soundings carried out in the Ciorlano area (T1 and T2 in Fig. 4.8), Vs30 values equal to 428 m/s and 344 m/s, respectively, were found. The processing of the data coming from the two HVSR acquisitions (Figs. 4.18) provided punctual stratigraphic columns that show values of Vs, and corresponding depths, which are consistent with the results from the 3D ERT survey. Indeed, the HVSR analysis confirms, for both T1 and T2 sites, the presence of a fractured (bedrock-like) rock layer at a depth of 60 m from the ground level, which deepens in the central part of the investigated area reaching values of *Vs* that correlate well with a carbonate basement.

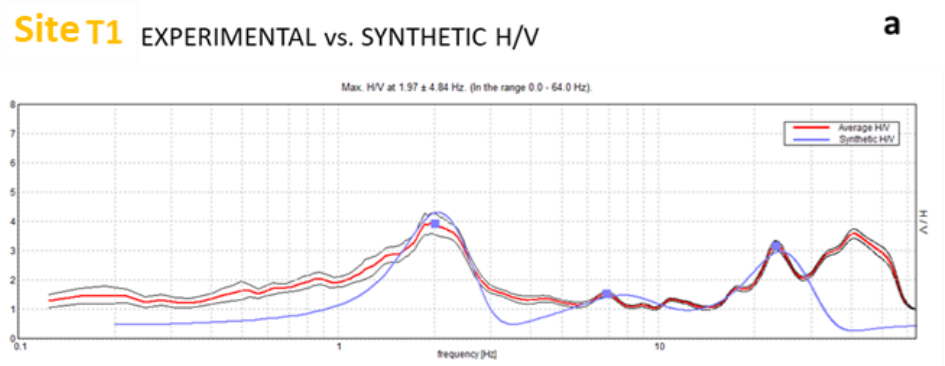

Depth at the bottom of the layer [m]	Thickness [m]	Vs [m/s]	Poisson ratio
2.00	2.00	186	0.45
13.00	11.00	380	0.42
70.00	57.00	558	0.45
inf.	inf.	1119	0.45

Vs(0.0-30.0)=428m/s

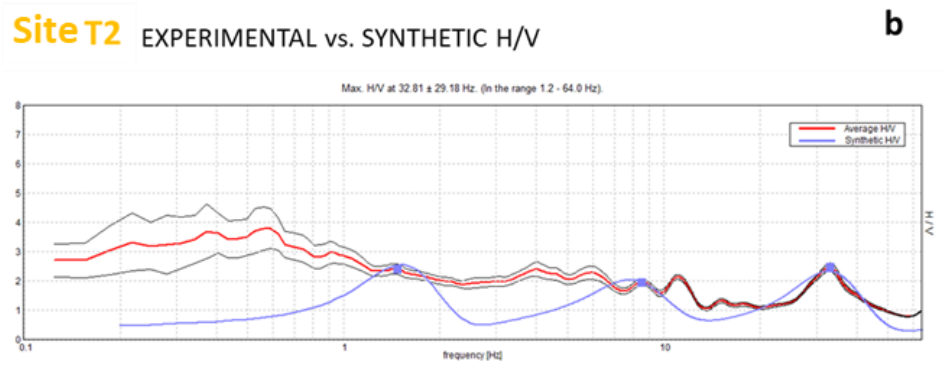

Depth at the bottom of the layer [m]	Thickness [m]	Vs [m/s]	Poisson ratio
1.00	1.00	132	0.45
8.00	7.00	254	0.42
68.00	60.00	423	0.45
inf.	inf.	780	0.45

Vs(0.0-30.0)=344m/s

Figure 4.18 *Results of the two HVSR soundings performed in the Ciorlano survey area (T1 and T2 in Fig. 4.8). a) Results related to the T1 site; b) results related to the T2 site.*

Chapter 5.

Modeling of CO_2 uprising by integration of geophysical and geochemical data

5.1 Introduction

As described in Chapter 1, the identification and the architecture of active faults permeable to CO_2 flows are fundamental for defining the geometry of the seismic-active zone and for understanding the processes governing the fluids flow along the damage zone of the faulty areas. The fluids flow study in a geological complex system requires an integrated approach that includes field surveys, laboratory measurements and numerical simulations. Repeated field surveys help define fluid migration paths and their evolution over time. (McManus and Hanor, 1993 and references therein). On the other side, laboratory measurements provide useful data for understanding active transport processes in flow systems and constrain the information about the rock parameters. Finally, numerical simulations allow different possible scenarios to be tested and help to predict the behaviour of the fluid flow circulation and the related risk analysis.

In particular, the geophysical surveys carried out in the Ciorlano area allowed the localization and modeling of preferential non-volcanic CO_2 migration paths in the proximity of a gas vent distinguished in the study area during the geophysical survey. This information, related to recent and accurate geological and geochemical analyses, has allowed us to simulate CO_2 rising along the main Colle Sponeta fault through the TOUGH2 numerical simulator. The integrated interpretation of all the available geological information with the geophysical results obtained in this research project allowed to obtain an accurate characterization of the investigated

system at a specific time, providing a constrain on the temporal evolution of diffuse CO_2 degassing at Colle Sponeta fault.

5.2 Numerical methods for fluid uprising simulation

Numerical modelling has become an important tool in managing geothermal systems and planning their exploitation. In the last ten years, numerical modelling of fluids flow in the subsoil has been an increasingly used research tool to study a wide range of geological processes, such as generation and migration of hydrocarbons and gases along seismically active faults.

The transport of multi-phase and multi-component fluids in porous and fractured rocks can be described by a set of partial differential equations expressing the principles of mass and energy conservation. These equations cannot be solved analytically, but have to be solved numerically, discretizing them in space and time, in order to obtain an equivalent system of linear algebraic equations, which can be resolved using direct or iterative approaches. The idea behind this operation is that every structure, however complex, can be fragmented into a finite number of elements having a simple shape. This procedure is simpler if compared with the problem posed on the whole structure, despite the greater time expenditure to calculate the solutions. However, thanks to the technological progress in the last decades, the use of gradually sophisticated techniques has increased the reliability of the numerical methods, which are used to quantify the transport processes in different tectonic environments. The “finite difference methods” have been used by numerous authors such as Bethke (1985, 1986a, b), Deming et al. (1990) e Deming and Nunn (1991), with the aim to quantify the transport processes in sedimentary basins. The “finite element methods” have a large flexibility in representing complex geometries and mechanical deformation along faults and, therefore, have been used by several authors such as Smith and Chapman (1983), Garven and Freeze

(1984a, b), Garven (1985, 1986, 1989), Ravenhurst and Zentilli (1987), Ge and Garven (1992, 1994), Person and Garven (1992, 1994), Raffensperger and Garven (1995a, b), Wieck et al. (1995). However, both methods require that the flow domain be discretized by a numerical mesh composed of a regular grid of rows and columns. This discretization could approximate the more the original system the more the elementary components are small and, in the transition to the limit (that is in the case of infinitesimal components), the description can be considered continuous. In general, a balance between the accuracy degree, required for the solution, and the complexity of solving the problem, is sought. For this reason, an optimal description of the system is required.

The realization of a numerical simulation is based on a series of work phases, the first of which represents the most delicate phase of the entire procedure and consists in the collection of data useful for the description of the system and in the elaboration of the conceptual model of the study area; the schematization must include both thermo-physical and chemical aspects. After the numerical model creation, it is necessary to establish the boundary and initial conditions. The boundary conditions concern the assignment of the values of the physical parameters, such as temperature and pressure at the model boundaries, and the assignment of heat or mass flows through the external surfaces delimiting the model. On the other way, the initial conditions describe the initial state of the system in terms of temperature, pressure and gas concentration. In general, the entire work is divided in the following steps:

1. model geometry discretization;
2. input parameters and boundary conditions definition;
3. simulation;
4. result interpretation and validation by comparison with the experimental data acquired in the study area;

5. use of validated models for predictive purposes.

For the present research, the TOUGH2 (Transport of Unsaturated Groundwater and Heat) numerical simulator software is used. It is a program that simulates flows of heat and multiphase, multicomponent fluid mixtures in porous and fractured media. It is particularly effective for describing water properties and phase transition, considering the relative permeability of the formations crossed by the fluids and the effects of capillarity pressure. Tough2 is essentially implemented for the study of geothermal systems and tank engineering, but is also successfully used in the environment risk evaluation, nuclear waste isolation studies, environmental assessment and remediation and in detecting the pollution propagation. This program, developed by *Lawrence Livermore Laboratory Berkely* (Pruess et al., 1991), uses a modular approach through interchangeable modules, called EOS (Equation of State), which define components, phases and thermodynamic properties of the study system, such as viscosity, enthalpy and fluids density. Table 5.1 lists some fluid property modules that are included in TOUGH2.

Module	Fluid components for flow simulation
EOS 1	water (liquid, vapor, two-phase), including 'two waters" for tracing fluid movement
EOS 2	water-C02 mixtures; originally developed by O'Sullivan et al. (1985)
EOS 3	water-air mixtures (Pruess et al., 1987)
EOS 4	water-air mixtures, including vapor pressure lowering according to Kelvin's equation (Edlefsen and Anderson, 1943)
EOS 5	water-hydrogen mixtures
EOS 7	mixtures of water-brine-air
EOS 8	water, non-condensable gas, and black oil
EOS 9	saturated/unsaturated flow according to Richards equation

Table 5.1 *List of Tough2 modules (modified from Pruess et al., 1991).*

Using the EOS modules, Tough2 can be used for modelling many different kinds of geothermal fields, as well as other complex sub-surface flow problems. In Fig. 5.1 a diagram of Tough2 structure is shown.

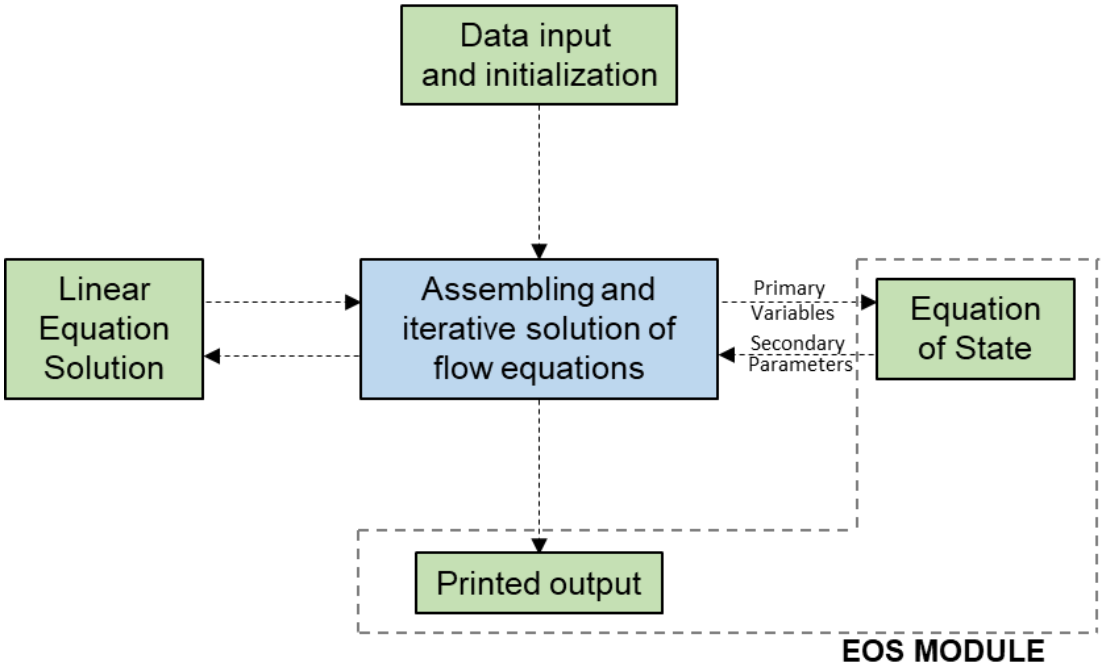

Figure 5.1 *Schematic structure and architecture of TOUGH2 (modified from Pruess et al., 1999).*

The Tough2 calculation code is structured on two main one-dimensional arrays which contain, respectively, the primary thermodynamic variables and the secondary thermophysical parameters required to assemble the equation governing the flow. Fluid advection is described with a multiphase extension of Darcy's law; the interference between the phases on a porous medium is represented by relative permeability functions. Heat flow occurs by conduction and convection, the latter including sensible as well as latent heat effects. The description of thermodynamic conditions assumes the local equilibrium of all phases. Fluid and formation parameters can be arbitrary nonlinear functions of the primary thermodynamic variables.

In general, space discretization occurs directly by integral form of the mass conservation equations, using the integral finite difference method (IFDM) that allows to create regular and non-regular grids in three dimensions. Time discretization is employed through the use of implicit methods because the flows are expressed in function of unknown thermodynamic parameters. Tough2 uses a

"cell-based" approach generating a grid made by a series of cells to which some fluid-thermodynamic variables and fluids velocity are associated, including velocity vector between two adjacent cells. Thus, the time-space discretization generates nonlinear algebraic equations that are solved through Raphson-Newton iterations, whose time-steps are automatically modified during the simulation, according to the speed convergence of the iterative process. This makes multi-phase flow simulation more effective, as time-intervals can change by different magnitude orders. Linear equation solution, at each time interval, can be performed using different methods selected by the user (e.g. "preconditioned conjugate gradient method" and "direct solution of sparse matrix method"). Direct methods are predictable but only interactive methods allow to solve problems using very large grids, for examples grids characterized by more than 10.000 blocks.

In detail, mass and energy-balance equations have the following general formulation:

$$\underbrace{\frac{d}{dt}\int_{V_n} M^k dV_n}_{\text{accumulation}} = \underbrace{\int_{S_n} \left(\overrightarrow{F^k} \cdot \vec{n}\right) dS_n}_{\text{flow}} + \underbrace{\int_{V_n} q^k \, dV_n}_{\text{production}}, \tag{5.1}$$

where V_n is an arbitrary sub-domain of the analysed flow system, which is bounded by the closed surface S_n, $\vec{n}$ is the normal vector to the surface element dS_n, M is the mass or energy per volume unit, K is the component number, F is the heat flow [kg/(m^{2}s)] of mass flow [J/(m^{2}s)], q represents the flow rate or heat rate from sources or wells per volume unit (kg/m^3 o J/m^3, respectively).

By discretizing the continuous space variables, the accumulation term in eq. (5.1) results:

$$\int_{V_n} M \, dV = V_n \; M_n, \tag{5.2}$$

where M is an extensive quantity per volume unit and M_n is its medium value in the sub-domain volume, while the surface integral in eq. (5.1) becames:

$$\int_{S_n} \left(\overrightarrow{F^k} \cdot \vec{n}\right) dS = \sum_m A_{nm} F_{nm}, \tag{5.3}$$

where A_{nm} is the contact surface between the volume elements (or grid blocks) V_n and V_m (the n index is about the considered volume and the m index is about the volume in contact with V_n), F_{nm} is the average value of the F component perpendicular to the A_{nm} surface, as shown in Fig. 5.2.

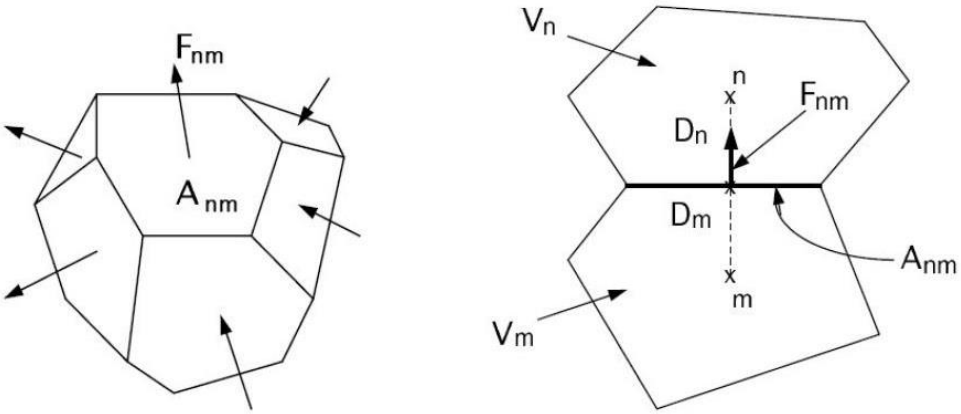

Figure 5.2 *Spatial discretization and geometric data in the integral finite difference method (IFDM) (from Pruess et al., 1999).*

Replacing eqs. (5.2) and (5.3) in eq. (5.1), one has:

$$\frac{dM_n^k}{dt} = \frac{1}{V_n} \sum_m A_{nm} F_{nm}^k + q_n^k. \tag{5.4}$$

The time is discretized as first order finite differences, and the terms related to flows and sources (second member in eq. 5.4) are evaluated at time step $t^{j+1} = t^j + \Delta t$, with the aim to obtain numerical stability and effective calculation of the multiphase flow. Thus, the time-space discretization generates the system of non-linear algebraic equations of the type:

$$R_n^{k,j+1} = M_n^{k,j+1} - M_n^{k,j} - \frac{\Delta t}{V_n}\left[\sum_m A_{nm} F_{nm}^{k,j+1} + V_n q_n^{k,j+1}\right] = 0, \tag{5.5}$$

where the first member of the equation is the residual.

The Raphson-Newton iterative method, implemented on the eqs. (5.5), stops at the iteration that provides residues satisfying the following predetermined relative convergence condition:

$$\left|\frac{R_{n,p+1}^{k,j+1}}{M_{n,p+1}^{k,j+1}}\right| \leq \varepsilon_1.$$

Another fundamental feature of the TOUGH2 simulator is represented by the use of an optimization process to obtain a well calibrate model of the analyzed geothermal system (O´Sullivan et al., 2001). Specifically, during the calibration process, the input model parameters, such as permeability, temperature and mass, are adjusted to match the values actually measured.

As above specified, the thermophysical properties of fluid mixtures needed for assembling the governing mass and energy-balance equations are provided by the EOS modules (see Tab. 5.1), which can represent different fluid mixtures. The fluid phase conditions are recognized from the numerical values of the primary variables (see for example Tab. 5.2). Each EOS module fulfils three additional important functions:

- the phase conditions pertaining to a given set of primary variables are identified for all the volume elements (grid blocks);
- the appearance (or disappearance) of phases is recognized as primary variables change during the Newton-Raphson iteration process;
- primary variables are switched and properly re-initialized in response to a change of phase.

The idea of primary variables/secondary parameters, as implemented in TOUGH2, essentially eliminates any direct connection between the choice of primary variables

and the secondary parameters that are used to set up the flow equations. This provides maximum flexibility and convenience in the choice of primary variables, because only secondary parameters are used in the flow equations.

In this PhD study, the EOS2 module is used, which is an updated version of the module originally developed by O'Sullivan et al. (1985) for the description of fluids in gas-rich geothermal reservoirs that may contain masses of CO_2 with fractions ranging from a few percent to occasionally 80% or more (Atkinson et al., 1980). EOS2 describes the non-ideal behaviour of gaseous CO_2 and the dissolution of CO_2 in the aqueous phase; moreover, EOS2 is able to simultaneously consider the effect of brine and vapour. According to the Henry's law, the partial pressure of an uncondensed gas, P_{NCG}, in the gas phase is proportional to the molar fraction of NCG, x_{aq}^{NCG}, dissolved in the aqueous phase:

$$P_{NCG} = K_h x_{aq}^{NCG}. \tag{5.6}$$

The coefficient of the Henry's law, K_h, for dissolving CO_2 in water strongly depends on temperature; this correlation has been improved by O'Sullivan et al. (1985) for extremely high temperature conditions found in geothermal reservoirs. It is accurate within the temperature range 40˚C ≤ T ≤ 330˚C, but it becomes rather inaccurate at lower temperatures and even reaches negative values for T < 30˚C (see Fig. 5.3).

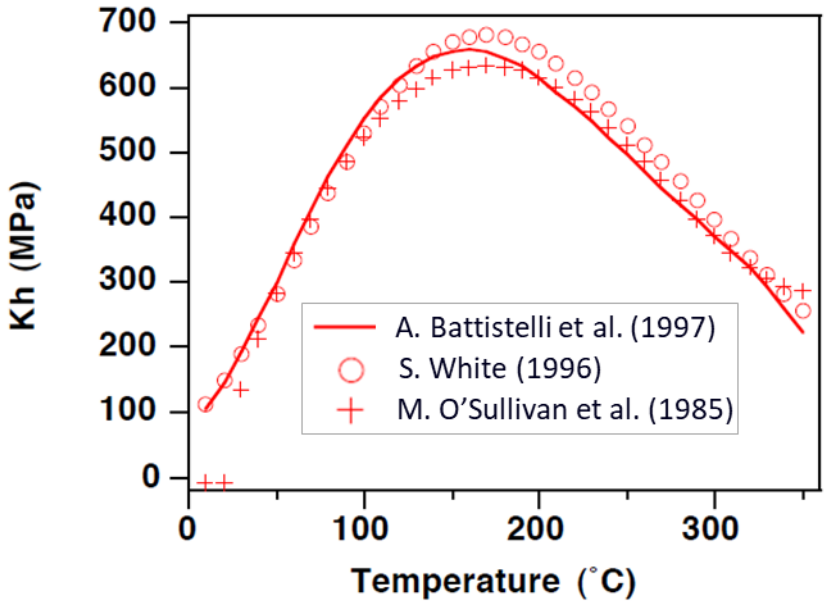

Figure 5.3 *Coefficient of the Henry's law as a function of the temperature for dissolving CO_2 in water (from Pruess et al., 1999).*

The HENRY subroutine in EOS2 has been replaced with a new routine that uses the correlation developed by Battistelli et al. (1997), which is more appropriated for 0˚C ≤ T ≤ 350˚C. The viscosity of the vapor-CO_2 mixtures is described with a formulation due to Pritchett et al. (1981); other correlations of thermophysical properties are based on the Sutton and McNabb model (1977). Specifications and parameters of the used EOS2 are summarized in Table 5.2.

Components
1: water
2: CO_2
Chosen parameters
NK, NEQ, NPH, NB = 2, 3, 2, 6
molecular diffusion can be modeled by setting NB = 8
Primary Variables
single-phase conditions: P, T, PCO_2 (pressure, temperature, CO_2 partial pressure)
two-phase conditions: Pg, Sg, PCO_2 (gas phase pressure, gas saturation, CO_2 partial pressure)

Table 5.2 *Characteristics of the EOS2 module, where NK is the number of components in a system phase; NEQ is the number of equations (mass and heat balances) per grid block; NPH is the number of phases that can be present; NB is the number of secondary parameters.*

5.3 Geological Modeling of Colle Sponeta fault

The geological modelling of the Colle Sponeta fault is a fundamental step to characterize the CO_2-permeable active fault. An accurate 3D geological model that represents a scheme as realistic as possible of the study area is needed. The reliability of the model is provided by the quality and quantity of available surface and subsurface data. Since the modelling requires the spatial discretization of the investigated volume, the geophysical investigations are key elements as they provide volumetric information of the buried structures. The results of the high-resolution 3D ERT prospecting illustrated in the previous chapter, integrated with borehole data, have indeed allowed an accurate definition of the geometrical and physical properties of the analyzed fault zone. However, from a computational point of view, it is not possible to discretize the volume through a grid made up of too many blocks ($10^6 – 10^9$), because the computation time required would be too large. For this reason, the software performs flow simulations using upscaling techniques that allow to select on the geological model the significant characteristics for the flow simulation, such as the main faults rather than some layers of sedimentary rock. Since the chosen grid must best adapt to the geological model to be schematized, appropriate petrophysical parameters, initial and boundary conditions must be assigned to each block of the grid.

Based on the results of the geophysical investigations carried out in the study area (see Chap. 4), a synthetic geological model with a length of 470 m, a width of 60 m and a thickness of 120 m was considered (De Paola et al., 2019; Di Maio et al., 2019). More specifically, from the inversion of the 3D ERT data (Fig. 5.4a), the system was approximated by a sequence of three layers representative of the lithostratigraphic units of the study area (Fig. 5.4b), i.e.

1. a shallow and impermeable clay layer with a thickness of 10 m;

2. a water saturated layer of alluvial coverage deposits (silt and clays) with a thickness of 60 m;
3. a carbonate basement from a depth of 70 m below the ground level.

The chosen volume was then discretized into a grid made up of 4.230 regular-shaped elementary cells and referenced according to a XYZ coordinate system with the X-axis in the SN direction, the Y-axis in the WE direction and the Z-axis oriented upwards (Fig. 5.4b). The discretization along the three axes is as follows:

- 6 cells 10 m long in the X direction;
- 47 cells 10 m long in the Y direction;
- 15 layers in the Z direction, with cells 2 m long for the first layer and 10 m long for the other layers.

As regards the petrophysical parameters and the initial and boundary conditions to be assigned to each layer for the numerical simulation, geological and geochemical literature data were considered, which are summarized in Tables 5.3 and 5.4. As shown in Table 5.3, the second layer is assumed to be the most permeable layer between a less permeable clay shallow layer and the underlying fractured carbonate basement. A decrease in porosity values with depth is also supposed; however, the stability of the simulation results was verified by varying the value of such parameter by 5%.

As shown in Fig. 5.4b, the considered volume includes the Colle Sponeta fault (darker cells) as a homogeneous and isotropic region between two parallel sub-vertical planes equidistant from the progressive 235 m along the Y-axis. The angle of inclination measured from the horizontal axis (dip angle) is fixed at 70^{o}, in agreement with the inclination of the eastern border of the central resistive zone clearly evident in the 3D resistivity model of Fig. 5.4b; in this three-dimensional model, the fault extension along the Y and Z axes is supposed 60 m and 120 m, respectively (Fig. 5.4b).

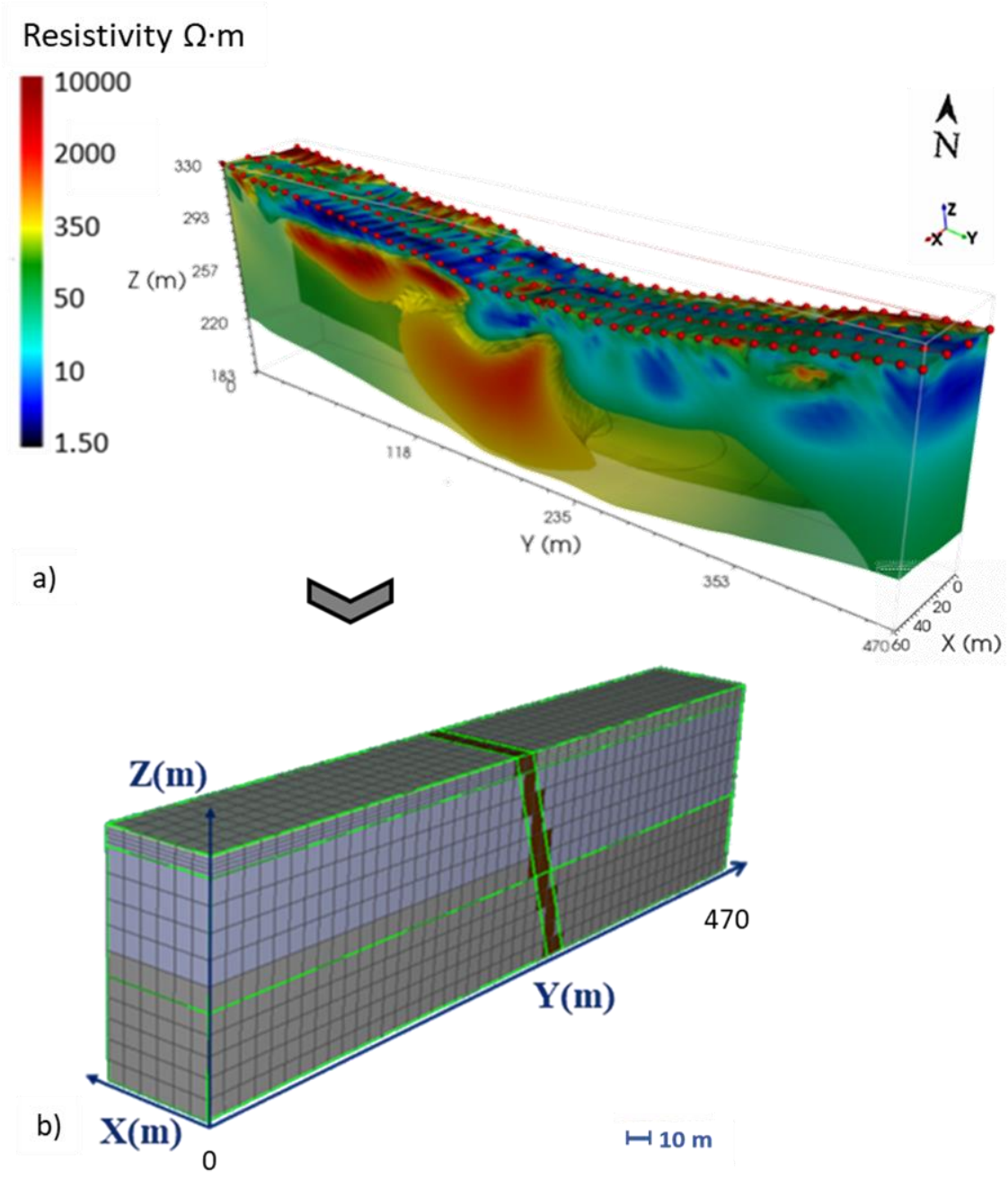

Figure 5.4 *a) 3D resistivity model; b) 3D geological model derived from the model (a) and used for simulating CO_2 emissions along the Colle Sponeta fault, which is described by the darker cells in the central part of the model.*

Rock Type	Depth (m b.g.l.)	Density (kg/m^3)	Porosity	Permeability (m^2)	Thermal conductivity (W/m°C)	Specific heat (J/kg°C)
Clay	0 – 10	1330	0.47	1.0E – 17	2.68	879
Clay + Gravel + Sand	10 – 70	1800	0.27	1.0E – 09	2.47	800
Damage zone		1600	0.88	2.0E – 17	2.48	839

Table 5.3 *Parameters used for characterizing the model in Fig. 5.4b.*

Initial conditions	
System phases	2
Pressure type	Lithostatic
Gas saturation	0.7
CO_2 gas pressure	70% lithostatic pressure

Table 5.4 *Parameters used for describing the initial conditions of the model in Fig. 5.4b.*

Figure 5.5 shows an example of geological model with highlighted in yellow an assumed geometry for the source cells, i.e. the cells with fixed conditions, which simulate a possible source for the CO_2 fluid flow. We note that the location of the source cells is a working hypothesis that cannot be easily inferred from geological, geophysical and geochemical data.

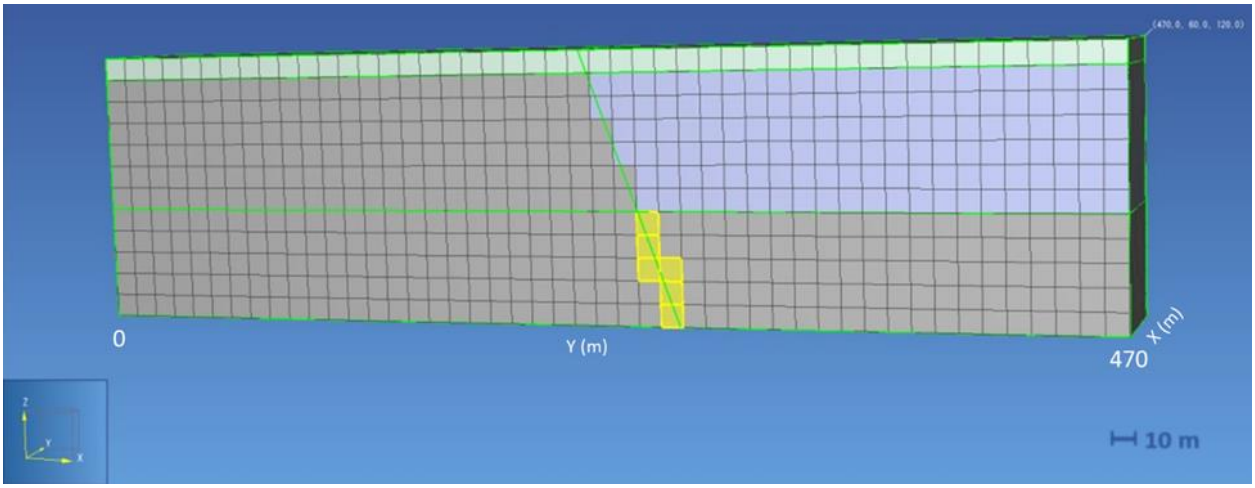

Figure 5.5 *Location of an assumed possible source (yellow cells) for the CO_2 fluid flow.*

The 3D model has been realized by using the PetraSim software, which is the graphical interface for the TOUGH2 family of simulators by an interactive 3D environment that includes mesh generation, parameter definition, and result visualization. To define a source cell, injection rate (or flux) and enthalpy have to be fixed as input parameters. In the following section, the results of numerical

simulations performed by assuming three different geometries for the source cells are presented and discussed.

5.4 Numerical simulation results of CO_2 uprising

Three different source systems were hypothesized for the geological model shown in Figure 5.4b. Numerical simulation of the temporal evolution of CO_2 degassing in such models was aimed at defining the system that better than the others is able to reproduce the values of CO_2 flow and gas saturation measured in the survey area (Ascione et al., 2018). Specifically, for the characterization of the source cells a constant rate of CO_2 flow equal to 5.78 kg/s (Ascione et al., 2018) and an enthalpy value of 505 J/kg was assigned to all the source cells of the grid, whilst a slightly higher rate (6.0 kg/s) and an entalpy value of 205 J/kg was assumed for the water-steam mixture. Finally, the gas saturation of the cells was assumed equal to 98%, according to Ascione et al. (2018).

In Figure 5.7a, the first investigated model is shown, where the CO_2 source cells (in yellow) are located in the fault roof block and, in particular, at the top of the carbonate basement. This model hypotheses that the fracture system spreading through the basement is obstructed and that the preferential migration path of water and CO_2 comes from the east, specifically, from the Matese Massif (Ascione et al., 2018). On the basis of this hypothesis, numerical simulations of the fluids and CO_2 rising dynamics have been performed to estimate the flux and gas saturation values within the investigated subsoil volume. The time required to reach stationary conditions was around 60 years. In Figs. 5.7b and 5.7c, the results are presented after 10 years and 60 years of simulated dynamics in terms of distribution of CO_2 flow vectors and of gas saturation, respectively. From these results, it is interesting to note the formation of convective circulation of the CO_2 flow at the top of the fault in the package composed of silts and clays. Indeed, because of buoyancy forces, CO_2

is expected to rise to the top of the permeable layer. However, a fraction of the CO_2 dissolves in the aqueous phase, it increases its density and the associated negative buoyancy force can induce convective circulation that will carry dissolved CO_2 downward, while causing additional dissolution of CO_2 into upflowing waters that are low in CO_2 (Pruess et al., 1999).

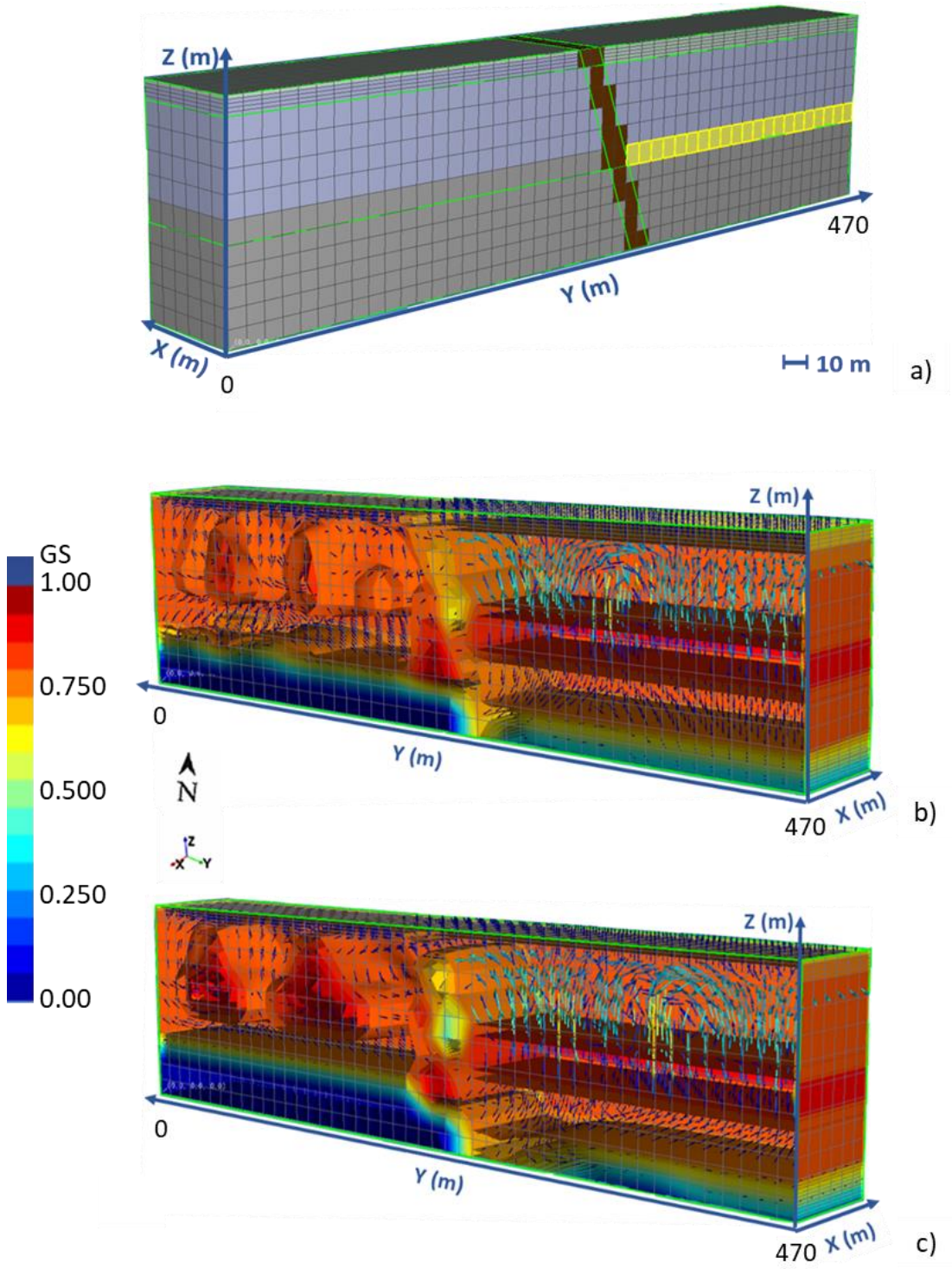

Figure 5.6 *1st source system: a) Three-dimensional geological model with location of the source cells (in yellow). Distribution of CO_2 flow vectors and gas saturation iso-surfaces (GS) after 10 years (b) and 60 years (c) of simulated dynamics.*

The second hypothesis proposed for the source system is illustrated in Figure 5.8a. In this model, the CO_2 source cells (in yellow) are positioned along the fault

plane at the depth of the carbonate basement. In this case, it has been assumed that the source is deep and that the fault acts as a preferential conduit for the upward migration of CO_2. Also for this source model, the numerical simulation was performed until to reach the stationary conditions, which were obtained after about 100 years of simulation. As examples, Figs. 5.8b and 5.8c show the results after 10 years and 100 years, respectively, of simulated dynamics. In this case, it is worth noting that after 10 years CO_2 storage masses form in the silt-clay package 60 m thick at the top of the fault, and their convective cells seem to reproduce the areas of higher resistivity which is possible to identify within the surface conductive layer of the 3D electrical resistivity model (see Fig. 5.4a).

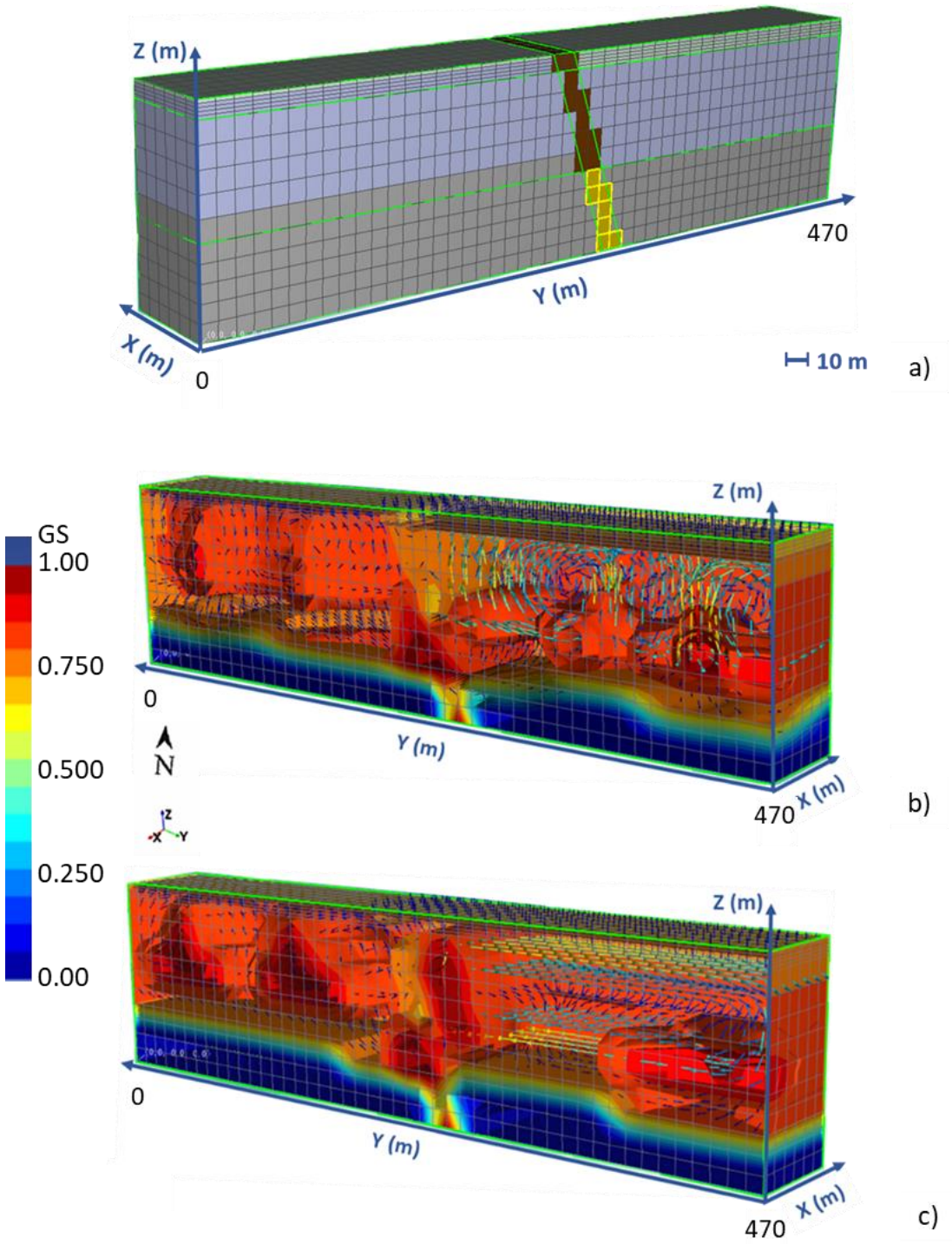

Figure 5.7 *2nd source system: a) Three-dimensional geological model with location of the source cells (in yellow). Distribution of CO_2 flow vectors and gas saturation iso-surfaces (GS) after 10 years (b) and 100 years (c) of simulated dynamics.*

The third hypothesis analysed for the source system is illustrated in Figure 5.9a. This hypothesis was formulated on the basis of the inversion results of the 3D electric resistivity survey that provided an extremely detailed characterization of the

investigated subsoil volume, highlighting the possible geometry of the fault plane (s. Figs. 4.12 and 4.14). In particular, from slices a, b, c, d in Figure 4.14, the damage zone is identified as a large resistive zone at a depth of 84 m b.g.l.. Thus, for the source model of Figure 5.9a, a larger damage zone was considered along the Y axis of the chosen reference system, having an extension of about 70 m. For this type of model, it is assumed that a much wider area, corresponding to the entire degraded zone at the fault boundaries, acts as a preferential path for CO_2 migration. As for the previous model (Fig. 5.8a), the CO_2 source cells (in yellow) were positioned along the entire damage zone at the depth of the carbonate basement. The time interval considered for studying the temporal evolution of the system was 100 years. As examples, in Figs. 5.9b and 5.9c the results of the numerical simulations after 10 years and 100 years of simulated dynamics, respectively, are shown. Also, in this case, the formation of convective circulation of the CO_2 flow at the top of the fault is evident in the silt and clay package characterized by greater permeability.

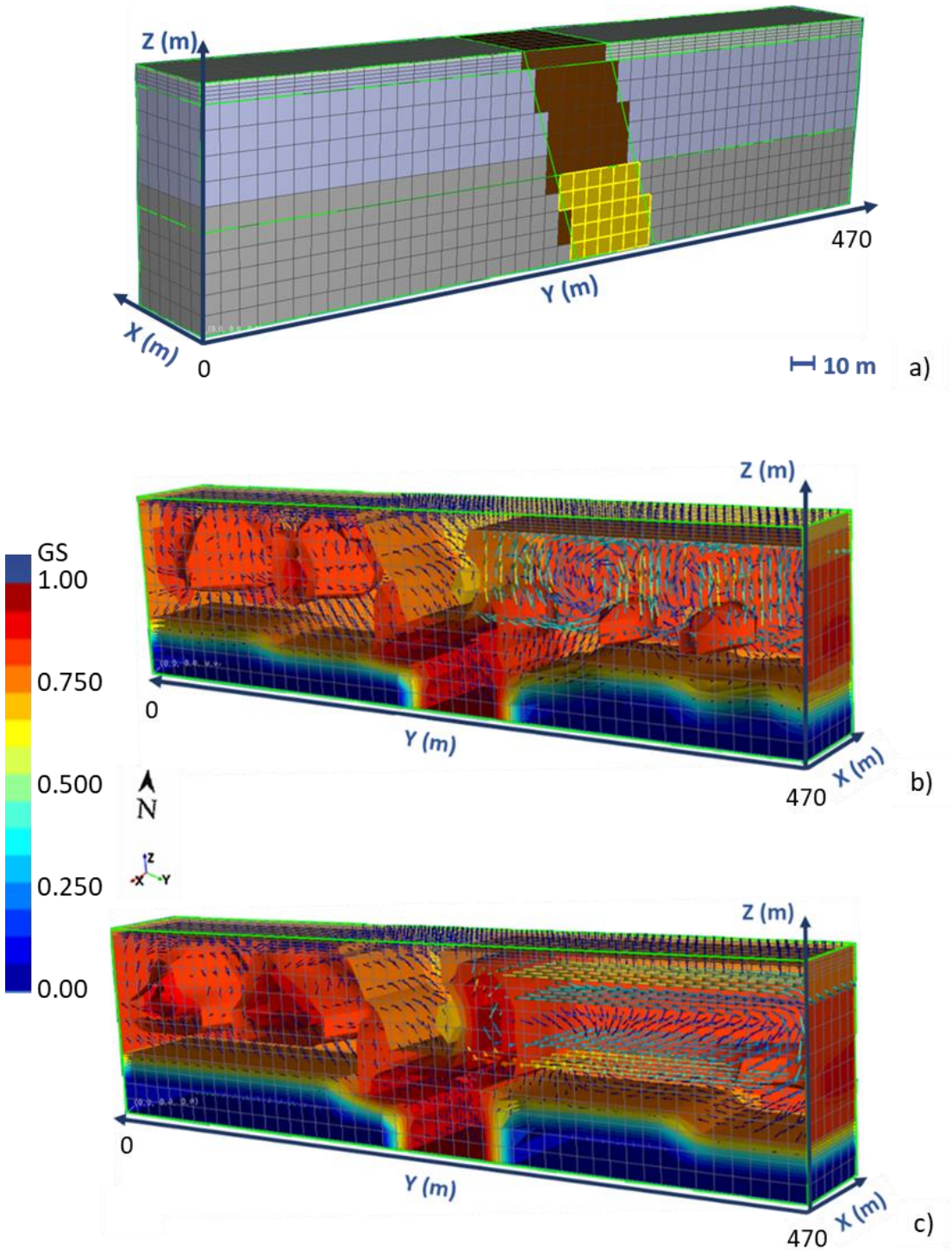

Figure 5.8 *3rd source system: a) Three-dimensional geological model with location of the source cells (in yellow) along the entire damage zone at the depth of the carbonate basement. Distribution of CO_2 flow vectors and gas saturation iso-surfaces (GS) after 10 years (b) and 100 years (c) of simulated dynamics.*

To evaluate the differences in the CO_2 flow and gas saturation estimates obtained from the numerical simulations carried out for the three different CO_2 source

geometries, the results obtained for the same cell of the simulation grid placed on the surface and near the fault (identified with the cell number 3690) have been analyzed. In particular, for this grid cell gas saturation and CO_2 flow have been represented as a function of time in Fig. 5.10a and 5.10b, respectively, thus permitting the comparison between the estimates provided by the numerical simulations and the values measured in situ, which for the Ciorlano area are of the order of 33 g/dm^2 and 76% (v/v), respectively (see also Chap. 3).

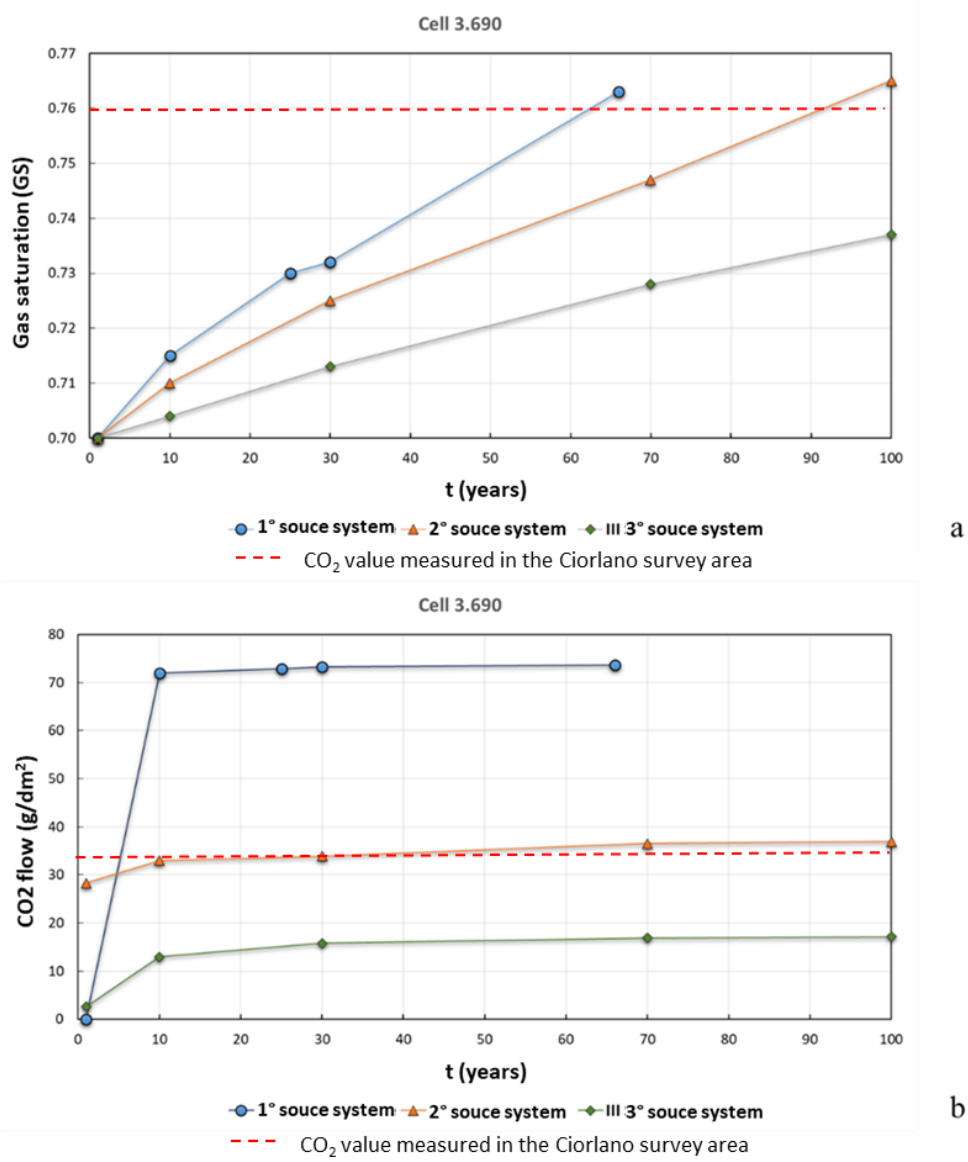

Figure 5.9 *(a) Gas saturation and (b) CO_2 flow values estimated for the cell n. 3690 at different time steps for the three hypothesized source systems. The red dashed line marks the value measured in the survey area.*

From the comparison shown in Figure 5.10a, it turns out that the first and second source systems are able to return gas saturation values comparable with those measured in situ after about 60 years and 90 years, respectively. The third hypothesized source system, on the other hand, returns, in the simulated time, much lower saturation values in gas, not comparable with those measured in situ. An explanation for this type of behaviour can be found in the dimension of the degraded area; indeed, the larger the area fractured and permeated by fluids, the longer is the time for the silt and clay pack to become saturated. By comparing the results of the three source models in terms of CO_2 flow estimates as reported in Fig. 5.10b, it is possible to realize that the first hypothesized source system, as well as the third one, returns flow values that are not reasonable for the area because they are much larger and much lower with respect the measured flows values for the first and third case, respectively. On the contrary, the second source system seems to be able to reproduce flow values comparable with those measured in situ. In particular, after 10 years of simulation, a CO_2 flow of 33 g/dm^2 is found after 10 years of simulation. Furthermore, for longer simulation times the estimated CO_2 flow does not appear to undergo significant variations and after 100 years it seems to have reached an asymptotic value, which is indicative of stationary conditions.

In summary, the first hypothesized source system reproduces only the measured gas saturation values, but not those of CO_2 flow. For the third system, instead, it would take a simulation time much longer than 100 years to obtain both gas saturation values and flow estimates higher than those obtained, which are significantly lower than those measured. However, since the CO_2 flow curve for the third model shown in Figure 5.10b seems to have reached an asymptotic value, it is reasonable to deduce that even if the simulation times is increased, it would not obtain flow values comparable with those measured. Thus, the model that provides the gas flow and saturation estimates that best compare with those measured in

situ turns to be the second model, which therefore suggests as source for the CO_2 degassing a relatively narrow fractured area along the Colle Sponeta fault.

In conclusion, the simulation results at different time steps for three different source models have been compared and the second source model has been found the best candidate to represent the survey area. More specifically, for this model the time evolution of the upward migration of CO_2 was simulated for different time periods and results after 10, 30 and 100 years are reported in Fig. 5.11a, b and c, respectively. As it is shown, a CO_2 convective flow is clearly present in the eastern part of the model: in particular, convective cells seem to be reduced to a single large convective cell from 10 to 100 years, likely due to an increase in the degree of saturation. On the western side, a large amount of gas under pressure is visible and the very low porosity degree of the lithology does not allow the escape of CO_2.

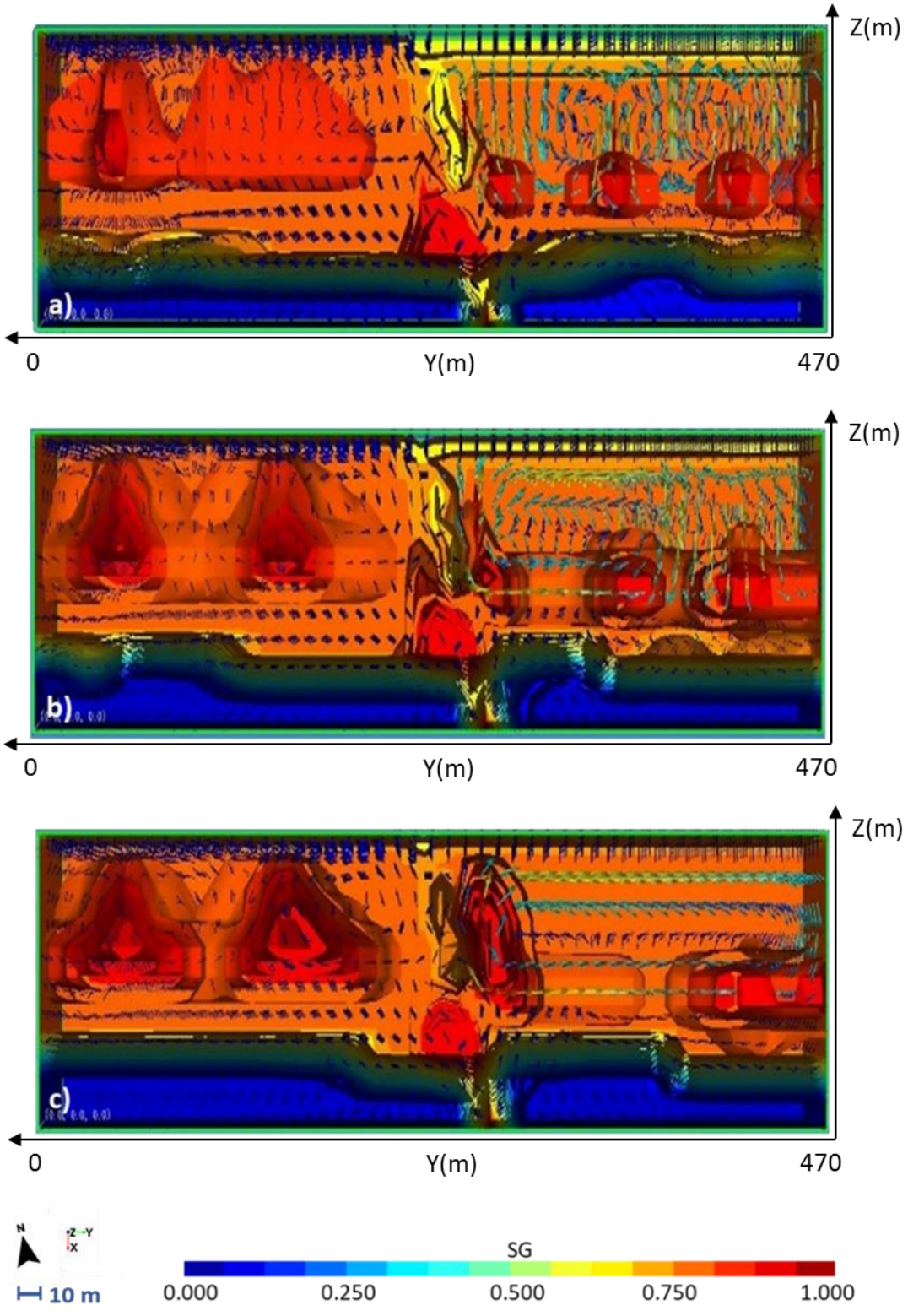

Figure 5.10 *Simulation results for the second source models at different time steps: a) 10 years; b) 30 years; c) 100 years.*

CONCLUSIONS

The present PhD research proposes a methodological approach based on high-resolution 3D ERT surveys and numerical modeling, which integrates geophysical, geological and geochemical data, to study the diffuse CO_2 degassing along active fault zones. The proposed procedure has been applied to the Ciorlano area (Matese Mts., southern Apennines, Italy) at the aim to localize and model preferential non-volcanic CO_2 migration pathways in the vicinity of a gas vent detected in the study area.

An innovative high-resolution 3D ERT technique based on non-conventional electrode configurations, generally applied to civil engineering fields, has been improved and optimized to investigate complex geological environments. The proposed technique, validated by comparing the results from non-conventional and standard electrode arrays applied in a test area, has been tested for applications in engineering, archaeological and geological field, in order to evaluate its effectiveness in relation to different targets. The main advantage of using non-conventional measurement arrays, in addition to overcoming logistical problems realted to complex topography areas and/or to historical sites that prevent the use of standard electrode layouts, is the high definition of the buried body/structure geometries. The obtained well-resolved subsurface models, in fact, offered useful hints to identify predisposing factors to dangerous debris landslides in the Mt. Faito area (Lattari Mts., southern Italy), as well as to explain historical damages observed in the Basilica of Santa Maria (Alvignano village, southern Italy) as a result of a seismic shaking. This preliminary phase of optimization of the proposed technique allowed to successfully apply for the first time the 3D ERT survey to reconstruct the architecture of active fault zones. In fact, the high-resolution 3D ERT surveys carried out in the Ailano and Ciorlano areas (Matese Mts., southern Italy), integrated with

literature geological data, provided a detailed geostructural and physical characterization of the investigated subsurface volumes, which allowed to identify and model, in term of resistivity contrasts, the Colle Sponeta fault zone and the complex migration path of the non-volcanic CO_2 flow. In particular, the 3D resistivity model obtained for the Ciorlano area suggests that the relatively high resistivity (about 60-70 Ωm) patterns observed in the shallow clay layer, at a depth of about 60 m b.g.l. in the easternmost part of the surveyed area, could be associated with possible CO_2 migration paths, which would cause an increase in the resistivity values. Furthermore, the very high resistivities (1000-2000 Ωm) observed in the central portion of the studied volume up to the maximum exploration depth (about 100 m g.g.l.) are very likely attributable to CO_2 volumes in the underlying fractured carbonate basement.

Finally, the 3D geophysical model, suitably integrated with recent and accurate geological and geochemical analyses, guided the numerical simulation of the CO_2 uprising along the main Colle Sponeta fault. Three different scenarios have been hypothesized corresponding to three different CO_2 source models. In particular, a model that hypothesizes the CO_2 source system located along the fault plane at the depth of the carbonate basement, was found to be the best candidate to represent the surveyed area. Indeed, the performed numerical simulations allow to well reproduce the gas flow and saturation estimates measured in situ.

It is worth noting that the proposed methodology can be helpful in many geological research fields, such as geothermal exploration and gas hazard assessment, due to the possibility of defining with high accurancy geometry and physical characteristics of fault systems in term of resistivity contrasts, whose knowledge is fundamental to identify possible preferential paths for gas movements, as well as gas storage reservoirs.

Finally, as for the future perspectives of the research, the use of new wireless systems for electric tomography, such as the *full waver system* (Iris Instruments - France) or the *multi-source system* (MPT - USA), will be experienced. This will allow to investigate very large areas reaching high investigation depths in relatively short times, thus allowing 4D ERT surveys for monitoring the carbon dioxide degassing. Such a monitoring could provide useful constraints to the subsequent numerical modeling for predicting future hazard scenarios.

Bibliography

Abrahamsen, P., Lia, O., and Omre, H., 1992: An Integrated Approach to Prediction of Hydrocarbon in Place and Recoverable Reserve with Uncertainty Measures, in: European Petroleum Computer Conference, Society of Petroleum Engineers.

Alcalde, J., Bond, C.E., Johnson, G., Butler, R.W., Cooper, M. A., and Ellis, J.F., 2017a: The Importance of Structural Model Availability on Seismic Interpretation, J. Struct. Geol., 97, 161–171.

Alcalde, J., Bond, C.E., Johnson, G., Ellis, J. F., and Butler, R.W., 2017b: Impact of Seismic Image Quality on Fault Interpretation Uncertainty, GSA Today, 27, 4–10.

Alcalde, J., Bond, C.E., and Randle, C.H.: Framing Bias, 2017c: The Effect of Figure Presentation on Seismic Interpretation, Interpretation, 5, T591–T605.

Alessio, E., Milani, B., Mestroni, G., Calligaris, M., Faleschini, P., and Attia, W.M., 1990: Synthesis and characterization of new halogen-tetramethylene sulfoxide-ruthenium (II) and ruthenium (III) complexes; crystal structure of cis-dichlorotetrakis (tetramethylene sulfoxide) ruthenium (II) and hydrogen trans-bis (tetramethylene sulfoxide) tetrachlororuthenate (III). *Inorganica chimica acta*, *177*(2), 255-265.

Amato, A., and Cinque, A., 1999: Erosional landsurfaces of the Campano–Lucano Apennines (S. Italy): genesis, evolution, and tectonic implications. *Tectonophysics*, *315*(1-4), 251-267.

Amato, A., Aucelli, P.P.C., and Cinque, A., 2003: The long–term denudation rate in the Southern Apennines Chain (Italy): a GIS – aided estimation of the rock volumes eroded since middle Pleistocene time. Quaternary International 101-102, 3–1.

Angerer, E., Crampin, S., Li, X.Y., and Davis, T.L., 2001: Processing and modelling time-lapse effects of over-pressured fluid-injection in a fractured reservoir, Geophy.J.Int. (submitted).

Annunziatellis, A., Beaubien, S.E., Bigi, S., Ciotoli, G., Coltella, M., and Lombardi, S., 2008, Gas migration along fault systems and through the vadose zone in the Latera caldera (central Italy): Implications for CO2 geological storage: International Journal of Greenhouse Gas Control, v. 2, p. 353–372.

Arts, R.J., Baradello, L., Girard, J.F., Kirby, G., Lombardi, S., Williamson, P., and Zaja, A., 2009: Results of geophysical monitoring over a “leaking” natural analogue site in Italy. Energy Procedia, 1(1), 2269-2276.

Ascione, A., Caiazzo, C., and Cinque, A., 2007: Recent faulting in Southern Apennines (Italy): geomorphic evidence, spatial distribution and implications for rates of activity. Bollettino della Società Geologica Italiana 126, 293–305.

Ascione, A., Ciarcia, S., Di Donato, V., Mazzoli, S., and Vitale, S., 2012: The Pliocene-Quaternary wedge-top basins of southern Italy: an expression of propagating lateral slab tear beneath the Apennines. Basin Research 24, 456–474

Ascione, A., Iannace, A., Imbriale, P., Santangelo, N., and Santo, A., 2014: Tufa and travertines of southern Italy: Deep-seated, fault-related CO2 as the key control in precipitation: Terra Nova, v. 26, p. 1–13

Ascione A., Ciotoli G., Bigi S., Buscher J., Mazzoli S., Ruggiero L., Sciarra A., Tartarello M.C., Valente E., 2018: Assessing mantle versus crustal sources for non-volcanic degassing along fault zones in the actively

extending southern Apennines mountain belt (Italy). *Geological Society of America Bulletin*, 130 (9/10), 1697-1722.

Ascione A., Ciotoli G., Bigi S., Buscher J., Mazzoli S., Ruggiero L., Sciarra A., Tartarello M. C., and Valente E., 2018: Assessing mantle versus crustal sources for non-volcanic degassing along fault zones in the actively extending southern Apennines mountain belt (Italy). Geological Society of America Bulletin, 130(9/10), 1697-1722.

Aucelli, P. P., Cesarano, M., Di Paola, G., Filocamo, F., and Rosskopf, C.M., 2013: Geomorphological map of the central sector of the Matese Mountains (Southern Italy): an example of complex landscape evolution in a Mediterranean mountain environment. *Journal of Maps*, *9*(4), 604-616.

Atkinson P.G., Celati R., Corsi R., and Kucuk F., 1980: Behavior of the Bagnore Steam/CO2 Geothermal Reservoir, Italy. Soc. Pet. Eng. J., 228 – 238.

Battistelli A., Calore C., and Pruess K., 1997: The Simulator TOUGH2/EWASG for Modeling Geothermal Reservoirs with Brines and Non-Condensible Gas. Geothermics, 26 (4) 437 – 464.

Barnes, A.E., 2000: Attributes for automating seismic facies analysis. In 2000 SEG Annual Meeting. Society of Exploration Geophysicists.

Beaubien, S.E., Ruggiero, L., Annunziatellis, A., Bigi, S., Ciotoli, G., Deiana, P., Graziani, S., Lombardi, S., and Tartarello, M.C., 2015: The importance of baseline surveys of near-surface gas geochemistry for CCS monitoring, as shown from onshore case studies in northern and southern Europe: Oil Gas Science Technology— Rev. IFP Energies nouvelles, v. 70, p. 615–633

Becken, M., and Ritter, O., 2012: Magnetotelluric studies at the San Andreas Fault Zone: implications for the role of fluids. Surveys in Geophysics, 33(1), 65-105.

Bentley, L.R., and Gharibi, M., 2004: Two-and three-dimensional electrical resistivity imaging at a heterogeneous remediation site. Geophysics, 69(3), 674-680.

Bergmann P., Schmidt-Hattenberger C., Kiessling D., Rücker C., Labitzke T., Henninges J., Baumann G., and Schütt H., 2012: Surface-downhole electrical resistivity tomography applied to monitoring of CO2 storage at Ketzin, Germany. Geophysics, 77, B253-B267.

Bergström, L., 1997: Hamaker constants of inorganic materials. Advances in colloid and interface science, 70, 125-169.

Bernard, H., Fjeldså, J., and Mohamed, M. 2009: A case study on the effects of disturbance and conversion of tropical lowland rain forest on the non-volant small mammals in north Borneo: management implications. Mammal Study, 34(2), 85-97.

Bethke C.M., 1985: A numerical model of compaction-driven groundwater flow and heat transfer and its application to the paleohydrology of intracratonic sedimentary basins. Journal of Geophysical Research, 90, 6817-6828.

Bethke, C.M., 1986a: Inverse hydrologic analysis of the distribution and origin of Gulf Coast-type geopressured zones. Journal of Geophysical Research, 91, 6535-6545.

Bethke, C.M., 1986b: Hydrologic constraints on the genesis of the upper Mississippi valley mineral district from Illinois Basin brines. Econ. Geol., 81,233-249.

Bichler, A., Bobrowsky, P., Best, M., Douma, M., Hunter, J., Calvert, T., and Burns, R., 2004: Three-dimensional mapping of a landslide using a multi-geophysical approach: the Quesnel Forks landslide. Landslides, 1(1), 29-40.

Boadu, F.K., & Owusu-Nimo, F., 2010: Influence of petrophysical and geotechnical engineering properties on the electrical response of unconsolidated earth materials. *Geophysics*, *75*(3), G21-G29.

Boyle, A., Wilkinson, P.B., Chambers, J.E., Meldrum, P.I., Uhlemann, S., and Adler, A., 2018: Jointly reconstructing ground motion and resistivity for ERT-based slope stability monitoring. Geophysical Journal International, 212(2), 1167-1182.

Bonardi, G., Amore, F.O., Ciampo, G., De Capoa, P., and Perrone, V., 1988: Il “Complesso Liguride" Auct.: stato delle conoscenze e problemi aperti sulla sua evoluzione appenninica ed i suoi rapporti con l'Arco calabro.

Bond, C.E., 2015: Uncertainty in Structural Interpretation: Lessons to Be Learnt, J. Struct. Geol., 74, 185–200.

Bond, C., Gibbs, A., Shipton, Z., and Jones, S., 2007: What Do You Think This Is? “Conceptual Uncertainty” in Geoscience Interpretation, GSA Today, 17, 4.

Bond, C.E., Philo, C., and Shipton, Z.K., 2011: When There Isn’t a Right Answer: Interpretation and Reasoning, Key Skills for Twenty-First Century Geoscience, Int. J. Sci. Educ., 33, 629–652.

Bonnefoy-Claudet, S., Cotton, F., Bard, P.Y., Cornou, C., Ohrnberger, M., and Wathelet, M., 2006a: Robustness of the H/V ratio peak frequency to estimate 1D resonance frequency. In Proceedings of the 3rd International Symposium on the Effects of Surface Geology on Seismic Motion.

Bonnefoy-Claudet, S., Cotton, F., and Bard, P.Y., 2006b: The nature of noise wavefield and its applications for site effects studies: A literature review. Earth-Science Reviews, 79(3-4), 205-227.

Bottari, C., Ferranti, L., Di Maio, R., Frisetti, A., De Paola, C., La Manna, M., Marazzi, F., 2019: Archaeoseismological and geophysical survey to study the 847 AD earthquake evidence in Central-Southern Italy. 38° National convention GNGTS, Extended Abstract.

Bottari, C., Ferranti, L., Di Maio, R., Frisetti, A., De Paola, C., La Manna, M., Marazzi, F., 2020: The 847 CE earthquake in central-southern Italy: New hints from archaeosismological and geophysical investigations in the Volturno River Valley area. Tectonophysics, 774, 228301.

Boschi, E., Guidoboni, E., Ferrari, G., Valensise, G., and Gasperini, P., 1997: Catalogue of strong Italian earthquakes, 461 B.C. to 1990: Bologna, Italy, ING-SGA, 644 p. and CD-ROM.

Břežný, M., Pánek, T., Lenart, J., Grygar, R., Táborík, P., and McColl, S.T., 2018: Sackung and enigmatic mass movement folds on a structurally-controlled mountain ridge. Geomorphology, 322, 175-187.

Brown, A., 1996: Interpretation of Three-dimensional Seismic Data, seventh ed.

Butler, R.W.H., 1987: Thrust sequences. J. Geol. Soc. 144, 619e634.

Butler, R.H.W., McCaffrey, W.D., 2004: Nature of the thrust zones in deep water sand-shale sequences: outcrop examples from the Champsaur sandstones of SE France. Mar. Pet. Geol. 21, 911e921.

Butler, R.W.H., Mazzoli, S., Corrado, S., De Donatis, M., Di Bucci, D., Gambini, R., Naso, G., Nicolai, C., Scrocca, D., Shiner, P., and Zucconi, V., 2004: Applying thick-skinned tectonic models to the Apennine thrust belt of Italy: Limitations and implications. In: McClay, K. R. (ed.), Thrust Tectonics and Hydrocarbon Systems. American Association of Petroleum Geologists, Memoirs82, 647-667.

Butler, R.W., and Mazzoli, S., 2006: Styles of continental contraction: A review and introduction. *Special papers-Geological Society of America*, *414*(1).

Butler, R.W.H., and Paton, D.A., 2010: Evaluating lateral compaction in deepwater fold and thrust belts: how much are we missing from Nature's Sandbox? GSA Today 20, 4e10.

Byrdina S., Revil A., Pant S.R., Koirala B.P., Shrestha P.L., Tiwari D.R., Gautam U.P., Shrestha K., Sapkota S.N., Contraires S., and Perrier F., 2009: Dipolar self-potential anomaly associated with carbon dioxide and radonflux at Syabru-Bensi hot springs in central Nepal. J. Geophys. Res. 114, B10101.

Caiazzo, C., Ascione, A., and Cinque, A., 2006: Late Tertiary–Quaternary tectonics of the Southern Apennines (Italy): new evidences from the Tyrrhenian slope.

Calabrò, R.A., Corrado, S., Di Bucci, D., Robustini, P., and Tornaghi, M., 2003: Thin-skinned vs. thick-skinned tectonics in the Matese Massif, Central–Southern Apennines (Italy): Tectonophysics, v. 377, p. 269–297.

Capalbo, A., Ascione, A., Aucelli, P.P.C, Mazzoli, S., 2010: Evaluation of the erosion rate in the Southern Apennines (Italy) based on geological-geomorphological data. Il Quaternario – Italian Journal of Quaternary Sciences 23(1), 75-90.

Caputo, R., Piscitelli S., Oliveto A., Rizzo E., and Lapenna V., 2003: Theuse of electrical resistivity tomographies in active tectonics: Examplesfrom the Tyrnavos Basin, Greece, J. Geodyn.,36,19–35, doi:10.1016/S0264-3707(03)00036-X.

Carcione, J.M., 2007: Wave Fields in Real Media: Wave Propagationin Anisotropic, Anelastic, Porous and Electromagnetic Media. Handb. Geophys. Explor., 38, 2nd ed., 514 Elsevier.

Carcione J.M., Gei D., Picotti S., and Michelini A., 2012: Cross-hole electromagnetic and seismic modeling for CO2 detection and monitoring in a saline aquifer. Journal of Petroleum Science and Engineering.

Carcione, J.M., and Picotti S., 2006: P wave seismic attenuation by slow-wave diffusion: Effects of inhomogeneous rock properties. Geophysics,71,1–8.

Cardozo, N., Bhalla, K., Zehnder, A.T., and Allmendinger, R.W., 2003: Mechanical models of fault propagation folds and comparison to the trishear kinematic model. J. Struct. Geol. 25, 1e18.

Carrigan, C.R., Yang, X., LaBrecque, D. J., Larsen, D., Freeman, D., Ramirez, A.L., Daily, W., Aines, R., Newmark, R., Friedmann, J., and Hovorka, S., 2013: Electrical resistance tomographic monitoring of CO2 movement in deep geologic reservoirs. Intl. J. of Greenhouse Gas Control, 18, 401–408.

Cartwright, J.A., Trudgill, B.D., and Mansfield, C.S., 1995: Fault growth by segment linkage; an explanation for scatter in maximum displacement and trace length data from the Canyonlands Grabens of SE Utah. J. Struct. Geol., 17, 1319e1326.

Castellaro, S., 2016: The complementarity of H/V and dispersion curves. Geophysics, 81(6), T323-T338.

Cello, G., Guerra, I., Tortorici, L., Turco, E., and Scarpa, R., 1982: Geometry of the neotectonic stress field in southern Italy: geological and seismological evidence. Journal of Structural Geology, 4, 385-393.

Cello, G., Gambini, R., Mazzoli, S., Read, A., Tondi, E., and Zucconi, V., 2000: Fault zone characteristics and scaling properties of the Val d'Agri fault system (Southern 93 Apennines, Italy). Journal of Geodynamics, 29, 293–307.

Chadwick, R., Noy, D., Arts, R., and Eiken, O., 2009: Latest time-lapse seismic data from Sleipner yield new insights into CO2 plume development Energy Procedia, 1, 2103-2110.

Chávez, R.E., Tejero, A., Argote, D.L., Cifuentes, G., Hernández-Quintero, J.E., and García-Serrano, A., 2017: Interior imaging of El Castillo Pyramid, Chichen Itza, Mexico, using ERT-3D methods: preliminary results. Geofísica Internacional, 56(2), 219-227.

Chambers, J.E., Wilkinson, P.B., Kuras, O., Ford, J.R., Gunn, D.A., Meldrum, P.I., and Ogilvy, R.D., 2011: Three-dimensional geophysical anatomy of an active landslide in Lias Group mudrocks, Cleveland Basin, UK. Geomorphology, 125(4), 472-484.

Chambers, J.C., Wilkinson, P.B., Wardrop, D., Hameed, A., Hill, I., Jeffrey, C., Loke, M.H., Meldrum, P.I., Kuras, O., Cave, M., and Gunn, D.M., 2012: Bedrock detection beneath river terrace deposits using three-dimensional electrical resistivity tomography. Geomorphology, 177-178, 17-25.

Chiarabba, C., Jovane, L., and Di Stefano, R., 2005: A new view of Italian seismicity using 20 years of instrumental recordings: Tectonophysics, 395, 251–268.

Childs, C., Nicol, A., Walsh, J.J., and Watterson, J., 1996: Growth of vertically segmented normal faults. J. Struct. Geol., 18, 1389e1397.

Childs, C., Nicol, A., Walsh, J.J., and Watterson, J., 2003: The growth and propagation of synsedimentary faults. J. Struct. Geol., 25, 633-648.

Chiodini, G., Cardellini, C., Amato, A., Boschi, E., Caliro, S., Frondini, F., and Ventura, G., 2004: Carbon dioxide Earth degassing and seismogenesis in central and southern Italy: Geophysical Research Letters, 31, L07615.

Chiodini, G., Cardellini, C., Caliro, S., Chiarabba, C., and Frondini, F., 2013: Advective heat transport associated with regional Earth degassing in central Apennine (Italy): Earth and Planetary Science Letters, 373, 65–74.

Christensen, N.B., Sherlock, D., and Dodds K., 2006: Monitoring CO2 injection with cross-hole electrical resistivity tomography. Exploration Geophysics, 37(1), 44–49.

Chopra, S., and Marfurt, K.J., 2005: Seismic Attributes e a historical perspective. Geophysics, 70, 3SO-28SO.

Chopra, S., and Marfurt, K.J., 2007: Curvature attribute applications to 3D seismic data. The Leading Edge, 26(4), 404-414.

Chopra, and Marfurt, K.J., 2010: Integration of coherence and volumetric curvatures images. The Leading Edge, 30, 1092-1107.

Ciarcia, S., Vitale, S., Di Staso, A., Iannace, A., Mazzoli, S., and Torre, M., 2009: Stratigraphy and tectonics of an Internal Unit of the southern Apennines: implications for the geodynamic evolution of the peri-Tyrrhenian mountain belt. Terra Nova, 21(2), 88-96.

Ciarcia, S., Mazzoli, S., Vitale, S., and Zattin, M., 2012: On the tectonic evolution of the Ligurian accretionary complex in southern Italy. GSA Bulletin, 124(3-4), 463-483.

Cinque, A., Patacca, E., Scandone, P., Tozzi, M., 1993: Quaternary kinematic evolution of the Southern Apennines. Relationships between surface geological features and deep lithospheric structures. Annali di Geofisica, 36, 249-260.

Cinque, A., Ascione, A., and Caiazzo, C., 2000: Distribuzione spazio-temporale e caratterizzazione della fagliazione quaternaria in Appennino meridionale, in Galadini, F., Meletti, C., Rebez, A., eds., Le Ricerche del GNDT nel Campo della Pericolosita Sismica: CNR-GNDT, Roma, Italy, 107–136.

Cippitelli, G., 2007: The CROP-04 seismic profile. Interpretation and structural setting of the Agropoli-Barletta Geotraverse, inCROP-04. Bollettino della Società Geologica Italiana, Special Paper7, 267-281.

Ciotoli, G., Etiope, G., Guerra, M., and Lombardi, S., 1999: The detection of concealed faults in the Ofanto Basin using the correlation between soil-gas fracture surveys. Tectonophysics, 301(3-4), 321-332.

Constable, S.C., Parker, R.L., and Constable, C.G., 1987: Occam's inversion: A practical algorithm for generating smooth models from electromagnetic sounding data. Geophysics, 52(3), 289-300.

Corradi, A., Ruffo, P., and Visentin, C., 2009: 3D hydrocarbon migration by percolation technique in an alternate sandshale environment described by a seismic facies classified volume. Mar. Pet. Geol., 26, 495-503.

Corniello, A., Ducci, D., and Guarino, P.M., 1999: The western part of the Matese carbonatic massif and Venafro plain: Hydrogeology and hydrogeochemistry. Bollettino della Societa Geologica Italiana, 118, 523–535.

Cowie, P.A., and Scholz, C.H., 1992: Displacement-length scaling relationship for faults; data synthesis and discussion. J. Struct. Geol., 14, 1149-1156.

Cyr, A.J., Olivetti, V., Granger, D.E., Molin, P., and Faccenna, C., 2008: Comparing the Spatial Variability of Cosmogenic10Be Erosion Rates and Channel Steepness to Quaternary Uplift Rates in Northern and Southern Italy. In: 2008 Joint Meeting of the Geological Society of America, Soil Science Society of America, American Society of Agronomy, Crop Science Society of America, Gulf Coast Association of Geological Societies with the Gulf Coast Section of SEPM, Geological Society of America Abstracts with Programs40(6), 431.

Dabas, M., Tabbagh, A., and Tabbagh, J., 1994: 3-D inversion in subsurface electrical surveying—I. Theory. Geophysical Journal International, 119(3), 975-990.

Dahlin, T., 1996: 2D resistivity surveying for environmental and engineering applications. First break, 14(7), 275-283.

Dahlin, C., Aronsson, H., Wilks, H.M., Lebedev, N., Sundqvist, C., and Timko, M.P., 1999: The role of protein surface charge in catalytic activity and chloroplast membrane association of the pea NADPH: protochlorophyllide oxidoreductase (POR) as revealed by alanine scanning mutagenesis. Plant molecular biology, 39(2), 309-323.

Dahlin, T., Leroux, V., and Nissen, J., 2002: Measuring techniques in induced polarisation imaging. Journal of Applied Geophysics, 50(3), 279-298.

Daily W., Ramirez A., LaBrecque D., and Nitao J., 1992: Electrical resistivity tomography of vadose water movement. Water Resources Research, 28, 1429– 1442.

Daily, W., Ramirez, A., and Johnson, R. 1998: Electrical impedance tomography of a perchloroethylene release. Journal of Environmental & Engineering Geophysics, 2(3), 189-201.

Daily W., Ramirez A., Binley A., LaBrecque D., 2004: Electrical resistance tomography. The Leading Edge, 23, 438-442.

De Groot, F.M. F., Fuggle, J.C., Thole, B.T., and Sawatzky, G.A., 1990: 2p x-ray absorption of 3d transition-metal compounds: An atomic multiplet description including the crystal field. Physical Review B, 42(9), 5459.

Deming, D., and Nunn, J.A., 1991: Numerical simulations of brine migration by topographically driven recharge. Journal of Geophysical Research, 96, 2485-2499.

Dey, A., and Morrison, H.F., 1979: Resistivity modelling for arbitrarily shaped two-dimensional structures. Geophysical Prospecting, 27(1), 106-136.

De Paola, N.D., Hirose, T., Mitchell, T., Toro, G.D., Viti, C., and Shimamoto, T., 2011: Fault lubrication and earthquake propagation in thermally unstable rocks. Geology, 39, 35–38.

De Paola, C., and Candela S., 2017: Determination of the posts length of a bulkhead using high resolution ERT 3D. 36th National Congress of GNGTS, Extended Abstract.

De Paola, C., and Candela S., 2018: High-resolution geoelectrical characterization of the conditions of the coverage overlying a tunnel being excavated by a new 3d data acquisition technique. 37th National Congress of GNGTS, Extended Abstract.

De Paola, C., Di Maio, R., and Piegari E., 2018: High-resolution geoelectrical characterization of steep pyroclastic slopes by a new 3D data acquisition technique. Proceedings 24th European Meeting of Environmental and Engineering Geophysics, Near Surface Geoscience, Extended Abstract.

De Paola, C., Di Maio, R., and Piegari, E., 2019: ERT and SP measurements for the Characterization of Fault-Controlled Soil CO2 Degassing. Proceedings 25th European Meeting of Environmental and Engineering Geophysics (Vol. 2019, No. 1, pp. 1-5). European Association of Geoscientists & Engineers.

Deming, D., Nunn J.A., and Evans, D.G., 1990: Thermal effects of compaction-driven groundwater flow from over thrust belts. Journal of Geophysical Research, 95, 6669-6683.

Dewey, J.F., Helman, M.L., Knott, S.D., Turco, E., and Hutton, D.H.W., 1989: Kinematics of the western Mediterranean. Geological Society, London, Special Publications, 45, 265-283.

Diaferia, I., Barchi, M., Loddo, M., Schiavone, D., and Siniscalchi, A., 2006: Detailed imaging of tectonic structures by multiscale Earth resistivity tomographies: The Colfiorito normal faults (central Italy). Geophysical Research Letters, 33(9).

Di Bucci, D., Massa, B., Tornaghi, M., and Zuppetta, A., 2005: Structural setting of the 1688 Sannio earthquake epicentral area (Southern Italy) from surface and subsurface data: Journal of Geodynamics, 40(2), 294–315.

Di Maio, R., De Paola, C., Forte, G., Piegari, E., Pirone, M., Santo, A., and Urciuoli, G., 2020: An integrated geological, geotechnical and geophysical approach to identify predisposing factors for flowslide occurrence. Engineering Geology, 267, 105473.

Di Maio, R., Patella, D., Petrillo, Z., Siniscalchi, A., Cecere, G., and De Martino, P., 2000: Application of electric and electromagnetic methods to the definition of the Campi Flegrei caldera (Italy). Annali di Geofisica, 43(2), 375-390.

Di Maio, R., La Manna, M., and Piegari, E., 2015: 3D Reconstruction of Buried Structures from Magnetic, Electromagnetic and ERT Data: Example from the Archaeological Site of Phaistos (Crete, Greece). Archaeological Prospection, 23(1), 3-13.

Di Maio, R., and Piegari, E., 2012: A study of the stability analysis of pyroclastic covers based on electrical resistivity measurements. Journal of Geophysics and Engineering, 9(2), 191-200.

Di Maio, R., Piegari, E., Salone R., and De Paola C., 2019: Modeling of non-volcanic CO2 earth degassing. Application to a case study from Ciorlano area (southern Apennines, Italy). Proceedings 38th National Congress of GNGTS.

Drahor, M.G., Göktürkler, G., Berge, M.A., Kurtulmuş, T.Ö., and Tuna, N., 2007: 3D resistivity imaging from an archaeological site in south-western Anatolia, Turkey: a case study. Near Surface Geophysics, 5(3), 195-201.

Dutzer, J.F., Basford, H., and Purves, S., 2009: Investigating fault sealing potential through fault relative seismic volume analysis. Pet. Geol. Conf. Ser., 7, 509-515.

Ellis, R.G., and Oldenburg, D.W., 1994: Applied geophysical inversion. Geophysical Journal International, 116(1), 5-11.

Esposito, E., Luongo, G., Marturano, A., and Porfido, S., 1987: Il terremoto di S. Anna del 26 luglio 1805: Memorie della Società Geologica Italiana, 37, 171–191.

Evans, D.J., Meneilly, A., Brown, G., 1992: Seismic facies analysis of Westphalian sequences of the southern North Sea. Mar. Pet. Geol., 9, 578-589.

Faccenna, C., Davy, P., Brun, J.-P., Funiciello, R., Giardini, D., Mattei, M., and Thierry Nalpas, T., 1996: The dynamics of back-arc extension: an experimental approach to the opening of the Tyrrhenian Sea. Geophysical Journal International, 126, 781–795.

Farooq, M., Basra, S.M.A., and Ahmad, N., 2007: Improving the performance of transplanted rice by seed priming. Plant Growth Regul., 51, 129–137.

Faulkner, D.R., Jackson, C.A.L., Lunn, R., Schlisch, R., Shipton, Z., Wibberley, C., and Withjack, M., 2010: A review of recent developments regarding the structure, mechanics and fluid flow properties of fault zones. J. Struct. Geol., 32, 1557-1575.

Fischanger, F., Morelli, G., LaBrecque, D., and Occhi, M., 2007: Monitoring resins injection with 3D Electrical Resistivity Tomography (ERT) using surface and multi-borehole electrode arrays. Proceedings 20th EEGS Symposium on the Application of Geophysics to Engineering and Environmental Problems, European Association of Geoscientists & Engineers, 1226–1233.

Fracassi, U., and Valensise, G., 2007: Unveiling the sources of the catastrophic 1456 multiple earthquake: Hints to an unexplored tectonic mechanism in southern Italy: Bulletin of the Seismological Society of America, 97(3), 725–748.

Francese, R., Mazzarini, F., Bistacchi, A., Morelli, G., Pasquarè, G., Praticelli, N., and Zaja, A., 2009: A structural and geophysical approach to the study of fractured aquifers in the Scansano-Magliano in Toscana Ridge, southern Tuscany, Italy. Hydrogeology Journal, 17(5), 1233-1246.

Freeman, B., Yielding, G., and Badley, M., 1990: Fault Correlation during Seismic Interpretation, First Break, 8, 87–95.

Frezzotti, M.L., Peccerillo, A., and Panza, G., 2009: Carbonate metasomatism and CO2 lithosphere–asthenosphere degassing beneath the western Mediterranean: An integrated model arising from petrological and geophysical data. Chemical Geology, 262(1), 108–120.

Forte, E., Pipan, M., Casabianca, D., Di Cuia, R., and Riva, A., 2012: Imaging and characterization of a carbonate hydrocarbon reservoir analogue using GPR attributes. Journal of Applied Geophysics, 81, 76-87.

Frodeman, R., 1995: Geological Reasoning: Geology as an Interpretive and Historical Science. Geol. Soc. Am. Bull., 107, 960–968.

Fournier, F., and Derain, J.F., 1995: A statistical methodology for deriving reservoir properties from seismic data. Geophysics, 60, 1437-1450.

Furre, A.K., Eiken O., Alnes, Vevatne J.N., and Kiær A.F., 2017: 20 years of monitoring CO2-injection at Sleipner. Energy Procedia, 114, 3916–3926.

Galli, P., and Galadini, F., 2003: Disruptive earthquakes revealed by faulted archaeological relics in Samnium (Molise, southern Italy): Geophysical Research Letters, 30(5).

Galli, P., and Naso, J.A., 2009: Unmasking the 1349 earthquake source (southern Italy): paleoseismological and archaeoseismological indications from the Aquae Iuliae fault. Journal of Structural Geology, 31, 128–149.

Gao, D., 2003: Volume texture extraction for 3D seismic visualization and interpretation. Geophysics, 68, 1294-1302.

Gao, D., 2007: Application of three-dimensional seismic texture analysis with special reference to deep-marine facies discrimination and interpretation: offshore Angola, West Africa. AAPG Bull., 91, 1665-1683.

Gasperini, P., Bernardini, F., Valensise, G., and Boschi, E., 1999: Defining seismogenic sources from historical earthquake felt reports. Bulletin of the Seismological Society of America, 89, 94–110.

Garven, G., and Freeze, R.A., 1984a: Theoretical analysis of the role of groundwater flow in the genesis of stratabound ore deposits, 1, Mathematical and numerical model. American Journal of Science, 284, 1085-1124.

Garven, G., and Freeze, R.A., 1984b: Theoretical analysis of the role of groundwater flow in the genesis of stratabound ore deposits, 2, Quantitative results. American Journal of Science, 284, 1125-1174.

Gelius, L.J., and Asgedom, E., 2011: Diffraction-limited imaging and beyond-the concept of super resolution. Geophys. Prospect., 59, 400-421.

Ge, S., and Garven, G., 1992: Hydromechanical modeling of tectonically driven groundwater flow with application to the Arkoma foreland basin. Journal of Geophysical Research, 97, 9119-9144.

Ge, S., and Garven, G., 1994: A theoretical model for thrust-induced deep groundwater expulsion with application to the Canadian Rocky Mountains. Journal of Geophysical Research, 99, 13851-13868.

Gerard, J., and Buhrig, C., 1990: Seismic facies of the Permian section of the Barents Shelf: analysis and interpretation. Mar. Pet. Geol. 7, 234-252.

Giocoli, A., Magrì, C., Vannoli, P., Piscitelli, S., Rizzo, E., Siniscalchi, A., Burrato P., Basso C.,and Di Nocera, S., 2008: Electrical resistivity tomography investigations in the ufita Valley (southern Italy). Annals of Geophysics, 51(1), 213-223.

Giocoli, A., Galli, P., Giaccio, B., Lapenna, V., Messina, P., Peronace, E., Romano, G., and Piscitelli, S. 2011: Electrical resistivity tomography across the Paganica-San Demetrio fault system (L'Aquila 2009 earthquake). Bollettino di Geofisica Teorica ed Applicata, 52(3), 457-469.

Godefroy, G., Laurent, G., and Bonneau, F., 2019: Structural Interpretation of Sparse Fault Data Using Graph Theory and Geological Rules. Mathematical Geosciences, 51, 1091–1107.

Googas, 2006: Results of INGV-DPCV5 project: The catalogue of Italian gas emissions.

Guéguen, Y., and Palciauskas, V., 1994: Introduction to the Physics of Rocks. Princeton University Press.

Günther, T., and Rücker, C., 2006: A general approach for introducing information into inversion and examples from dc resistivity inversion. Proceedings 12th EAGE European Meeting of Environmental and Engineering Geophysics (pp. cp-14). European Association of Geoscientists & Engineers.

Günther, A., and Jensen, K.F., 2006: Multiphase microfluidics: from flow characteristics to chemical and materials synthesis. Lab on a Chip, 6(12), 1487-1503.

Haefner, R.J., Sheets, R.A., and Andrews, R.E., 2010: Evaluation of the horizontal-to-vertical spectral ratio (HVSR) seismic method to determine sediment thickness in the vicinity of the South Well Field, Franklin County, OH. The Ohio Journal of Science, 110(4), 77-85.

Hagrey, S.A. 2010: 2D optimized electrode arrays for borehole resistivity tomography and CO 2 sequestration modelling. Pure and Applied Geophysics, 169(7), 1283-1292.

Hardy, S., and Allmendinger, R., 2011: Trishear. A review of kinematics, mechanics, and 783 applications. In: McClay, K., Shaaw, J., Suppe, J. (Eds.), Thrust Fault-related Folding, vol. 94. American Association of Petroleum Geologists Memoir, 95-119.

Heinicke, J., Koch, U., and Martinelli, G., 1995: CO2 and Radon measurements in the Vogtland area (Germany) — a contribution to earthquake prediction research. Geophysical Research Letters, 22, 771–774.

Hesthammer, J., Landrø, M., and Fossen, H., 2001: Use and abuse of seismic data in reservoir characterisation. Mar. Pet. Geol., 18, 635-655.

Hippolyte, J.-C., Angelier, J., Roure, F., and Casero, P., 1994: Piggyback basin development and thrust belt evolution: structural and palaeo-stress analyses of Plio-Quaternary basins in the Southern Apennines. Journal of Structural Geology, 16, 159-173.

Hovorka, S.D., Meckel, T.A., and Treviño, R.H., 2013: Monitoring a large-volume injection at Cranfield, Mississippi—Project design and recommendations. International Journal of Greenhouse Gas Control, 18, 345-360.

Iacopini, D., Butler, R.W.H., Purves, S., McArdle, N., and De Freslon, N., 2016: Exploring the seismic expression of fault zones in 3D seismic volumes. Journal of Structural Geology, 89, 54-73.

Improta, L., and Corciulo, M., 2006: Controlled source nonlinear tomography: A powerful tool to constrain tectonic models of the Southern Apennines orogenic wedge, Italy. Geology, 34, 941-944.

Italiano, F., Martelli, M., Martinelli, G., and Nuccio, P.M., 2000: Geochemical evidence of melt intrusions along lithospheric faults of the Southern Apennines, Italy: Geodynamic and seismogenic implications: Journal of Geophysical Research, 105(B6), 13569–13578.

Italiano, F., Martinelli, G., and Plescia, P., 2008: CO2 Degassing over Seismic Areas: The Role of Mechanochemical Production at the Study Case of Central Apennines. Pure and Applied Geophysics, 165, 75–94.

Jamieson, W.J., 2011: Geometrical analysis of fold development in overthrust terrane. J. Struct. Geol. 9, 207-219.

Jomard, H., Lebourg, T., Guglielmi, Y., and Tric, E. 2010: Electrical imaging of sliding geometry and fluids associated with a deep-seated landslide (La Clapière, France). Earth Surface Processes and Landforms: The Journal of the British Geomorphological Research Group, 35(5), 588-599.

Kastens, K., Mascle, J., Auroux, C., Bonatti, E., Broglia, C., Channell, J., and Hieke, W. 1988: ODP Leg 107 in the Tyrrhenian Sea: Insights into passive margin and back-arc basin evolution. Geological Society of America Bulletin, 100(7), 1140-1156.

Kemski, J., Klingel, R., and Siehl, A., 1996: Classification and mapping of radon-affected areas in Germany. Environmental International, 22, S789–S798.

Kneisel, C., and Hauck, C., 2008: Applied geophysics in periglacial environments. Cambridge University Press.

Khaidukov, V., Landa, E., and Moser, T.J. 2004: Diffraction imaging by focusing-defocusing: An outlook on seismic superresolution. Geophysics, 69(6), 1478-1490.

Kiessling, D., Schmidt-Hattenberger, C., Schuett, H., Schilling, F., Krueger, K., Schoebel, B., Danckwardt, E., Kummerow, J., 2010: Geoelectrical methods for monitoring geological CO2 storage: First results from cross-hole and surface-downhole measurements from the CO2SINK test site at Ketzin (Germany). International Journal of Greenhouse Gas Control, 4, 816-826.

Kikuta, K., Hongo, S., Tanase, D., and Ohsumi, T., 2005: Field test of CO2 injection in Nagaoka, Japan. In: Greenhouse Gas Control Technologies. Volume II Contributed Papers and Panel Discussion. RUBIN, E.S., KEITH, D.W., and GILBOY, C.F. (editors), Oxford: Elsevier Science Ltd., 1367–1372.

Koukadaki, M.A., Karatzas, G.P., Papadopoulou, M. P., and Vafidis, A. 2007: Identification of the saline zone in a coastal aquifer using electrical tomography data and simulation. Water Resources Management, 21(11), 1881.

Kumar, D., 2012: Efficacy of electrical resistivity tomography technique in mapping shallow subsurface anomaly. Journal Geological Society of India, 80, 304-307.

Kunetz, G., 1966: Principles of direct current - Resistivity prospecting. Geoexploration Monographs, 1, pp. 103.

LaBrecque, D., Bennett, J., Heath, G., Schima, S., and Sowers, H., 1998: Electrical resistivity tomography monitoring for process control in environmental remediation. Proceedings of the Symposium on the Application of Geophysics for Environmental and Engineering Problems (SAGEEP), 613–622.

Lambiase, S., and Ruggiero, A. 1980: La forra del Torano (Matese Centrale): un caso di convergenza fra morfogenesi carsica e fluviale. Atti della Società Toscana di Scienze Naturali–Memorie, 171-192.

Lebourg, T., Binet, S., Tric, E., Jomard, H., and El Bedoui, S., 2005: Geophysical survey to estimate the 3D sliding surface and the 4D evolution of the water pressure on part of a deep-seated landslide. Terra Nova, 17(5), 399-406.

Lecocq, T., and Camelbeeck, T., 2016: A geophysical cross-section of the Hockai Fault Zone (Eastern Belgium): imaging an intraplate weak crustal zone. AGUFM, 2016, T43D-3078.

Leighton, T.G., White, P.R., 2012: Quantification of undersea gas leaks from carbon capture and storage facilities, from pipelines and from methane seeps, by their acoustic emissions. Proc. R. Soc. A: Math. Phys. Eng. Sci., 468 (2138), 485-510.

Lines, L.R., and Treitel, S., 1984: Tutorial: A review of least-squares inversion and its application to geophysical problems. Geophysical Prospecting, 32(2), 159-186.

Locati, M., Camassi, R., and Stucchi, M., 2011: DBMI11, the 2011 version of the Italian Macroseismic Database: Milano, Italy.

Loke, M.H., and Barker, R.D., 1996: Rapid least-squares inversion of apparent resistivity pseudosections using a quasi-Newton method. Geophysical Prospecting, 44, 131-152.

Loke, M.H., 1999: Electrical imaging surveys for environmental and engineering studies. A practical guide to 2D and 3D surveys.

Loke, M.H., 2000: Topographic modelling in electrical imaging inversion. Proceedings 62nd EAGE Conference and Technical Exhibition, Extended Abstracts, D-2.

Loke, M.H., Acworth, I., Dahlin T., 2003: A comparison of smooth and blocky inversion methods in 2D electrical imaging surveys. Exploration Geophysics, 34, 182–187.

Loke, M.H. 2014: Tutorial: 2-D and 3-D electrical imaging surveys. Geotomo Softwares, Penang.

Long, J.J., Imber, J., 2010: Geometrically coherent continuous deformation in the volume surrounding a seismically imaged normal fault-array. J. Struct. Geol., 32, 222-234.

Macrae, E.J., 2013: Uncertainty in geoscience interpretation: Statistical quantification of the factors that affect interpretational ability and their application to the oil and gas industry. PhD Thesis, University of Strathclyde, Department of Civil and Environmental Engineering.

Marescot, L., Monnet, R., and Chapellier, D., 2008: Resistivity and induced polarization surveys for slope instability studies in the Swiss Alps. Engineering Geology, 98(1-2), 18-28.

McBride J.H., and Stephenson W.J., 2003: Contributions to Neotectonics and Seismic Hazard from Shallow Geophysical Imaging. Special Volume of Tectonophysics, 368, 1–4, 1– 227.

Marfurt, K.J., and Chopra, S., 2007: Seismic Attributes for Prospect Identification and Reservoir Characterization. SEG Geophysical development (11).

Mazzarini, L., Pacchiarotti, I., Colom, F., Sani, G., Kotzalidis, G.D., Rosa, A.R., and Sanchez-Moreno, J., 2009: Predominant polarity and temperament in bipolar and unipolar affective disorders. Journal of Affective Disorders, 119(1-3), 28-33.

Mazzoli, S., and Helman, M., 1994: Neogene patterns of relative plate motion for Africa-Europe: some implications for recent central Mediterranean tectonics. Geologische Rundschau, 83, 464-468.

Mazzoli, S., Corrado, S., De Donatis, M., Scrocca, D., Butler, R.W.H., Di Bucci, D., Naso, G., Nicolai, C., Zucconi, V., 2000: Time and space variability of “thin-skinned” and “thick-skinned” thrust tectonics in the Apennines (Italy). Rendiconti Lincei, Scienze Fisiche e Naturali, 11, 5-39.

Mazzoli, S., Barkham, S., Cello, G., Gambini, R., Mattioni, L., Shiner, P., and Tondi, E., 2001. Reconstruction of continental margin architecture deformed by the contraction of the Lagonegro Basin, southern Apennines, Italy. Journal of the Geological Society, 158(2), 309-319.

Mazzoli, S., D’Errico, M., Aldega, L., Corrado, S., Invernizzi, C., Shiner, P., and Zattin, M., 2008: Tectonic burial and ‘young’ (< 10 Ma) exhumation in the southern Apennines fold and thrust belt (Italy). Geology, 36, 243–246.

Mazzoli, S., Szaniawski, R., Mittiga, F., Ascione, A., and Capalbo, A., 2012: Tectonic evolution of Pliocene–Pleistocene wedge-top basins of the southern Apennines: new constraints from magnetic fabric analysis. Canadian Journal of Earth Sciences, 49(3), 492-509.

Mazzoli, S., Ascione, A., Candela, S., Iannace, A., Megna, A., Santini, S., and Vitale, S., 2013: Subduction and continental collision events in the Southern Apennines: constraints from two crustal cross-sections. Rendiconti Online Societa Geologica Italiana, 25, 78-84.

Mazzoli, S., Ascione, A., Buscher, J.T., Pignalosa, A., Valente, E., and Zattin, M., 2014: Low-angle normal faulting and focused exhumation associated with late Pliocene change in tectonic style in the southern Apennines (Italy). Tectonics, 33(9), 1802-1818.

McBride, C.M., Emmons, K.M., and Lipkus, I.M., 2003: Understanding the potential of teachable moments: the case of smoking cessation. Health education research, 18(2), 156-170.

Mckenna, J.J., Gurevich, B., Urosevic, M., and Evans, B.J., 2003: Rock physics – application to geological storage of CO2. Australian Petroleum Production and Exploration Association Journal, 43, 567–576.

McManus, K.M., and Hanor, J.S., 1993: Diagenetic evidence for massive evaporite dissolution, fluid flow, and mass transfer in the Louisiana Gulf Coast. Geology, 21, 727-730.

Menardi Noguera, A., and Rea, G., 2000: Deep structure of the Campanian-Lucanian Arc (southern Apennines). Tectonophysics, 324, 239-265.

Merritt, A.J., Chambers, J.E., Murphy, W., Wilkinson, P.B., West, L.J., Gunn, D.A., and Dixon, N. 2014: 3D ground model development for an active landslide in Lias mudrocks using geophysical, remote sensing and geotechnical methods. Landslides, 11(4), 537-550.

Michetti, A.M., Blumetti, A.M., Esposito, E., Ferreli, L., Guerrieri, L., Porfido, S., Serva, L., and Vittori, E., 2000: Earthquake Ground Effects and Seismic Hazard Assessment in Italy examples from the Matese and Irpinia areas, Southern Apennines. In: Active Fault Research for the New Millennium: Hokudan, Japan, Proceedings of the Hokudan Symposium and School on Active Faulting, 279–284.

Milano, G., Di Giovambattista, R., and Alessio, G., 1999: Earthquakes swarms in the Southern Apennines chain (Italy): The 1997 seismic sequence in the Sannio–Matese mountains. Tectonophysics, 306, 57–78.

Milano, G., Ventura, G., and Di Giovambattista, R., 2002: Seismic evidence of longitudinal extension in the Southern Apennines chain (Italy): The 1997–1998 Sannio–Matese seismic sequence. Geophysical Research Letters, 29(20).

Milano, G., Di Giovambattista, R., and Ventura, G., 2005: The 2001 seismic activity near Isernia (Italy): Implications for the seismotectonics of the Central–Southern Apennines. Tectonophysics, 401(3), 167–178.

Milano, G., Di Giovambattista, R., and Ventura, G., 2006, Seismicity and stress field in the Sannio-Matese area. Annals of Geophysics Supplement, 49(1), 347–356.

Mitra, S., 1990: Fault-propagation folds: geometry, kinematic evolution, and hydrocarbon traps (1). AAPG Bulletin, 74(6), 921-945.

Morelli, G., and LaBrecque, D.J. 1996: Advances in ERT inverse modelling. European Journal of Environmental and Engineering Geophysics, 1(2), 171-186.

Moser, T.J., Howard, C.B., 2008: Diffraction imaging in depth. Geophys. Prospect., 56, 627-641.

Neidell, N.S., and Taner, M.T., 1971: Semblance and other coherency measures for multichannel data. Geophys., 36, 482-497.

Myer, L.R., 2001: Laboratory measurement of geophysical properties for monitoring of CO2 sequestration. Proceedings 1st National Symposium on Carbon Sequestration, Morgantown, WV, May, 14-17.

Nakatsuka, Y., Xue, Z., Yamada, Y., Matsuoka, T., 2009: Experimental study on monitoring and quantifying of injected CO2 from resistivity measurement in saline aquifer storage. Energy Procedia, 1, 2211–2218.

Nicol, A., Seebeck, H, Field, B., McNamara, D., Childs, C., Craig J., Rolland, A., 2017: Fault permeability and CO2 storage. Energy Procedia, 114, 3229–3236.

Newmark, R.L., Daily, W.D., Kyle, K.R., and Ramirez A.L., 1998: Monitoring DNAPL Pumping Using Integrated Geophysical Techniques. Journal of Environmental and Engineering Geophysics, Society of Exploration Geophysicists.

Nguyen, F., Garambois, S., Jongmans, D., Pirard, E., and Loke, M.H., 2005: Image processing of 2D resistivity data for imaging faults. J. Appl. Geophys., 57, 260–277.

Nooner, S.L., Eiken, O., Hermanrud, C., Sasagawa, G.S., Stenvold, T., and Zumberge, M.A., 2007: Constraints on the in situ density of CO2 within the Utsira formation from time-lapse seafloor gravity measurements. International Journal of Greenhouse Gas Control, 1, 198–214.

Noy, D., Holloway, S., Chadwick, R., Williams, J., Hannis, S., and Lahann, R., 2012: Modelling large-scale carbon dioxide injection into the Bunter Sandstone in the UK Southern North Sea. International Journal of Greenhouse Gas Control, 9, 220–233.

Oddone, E., 1915: Gli elementi fisici del grande terremoto marsicano-fucense del 13 gennaio 1915. Boll. Soc. Sismol. Ital., 19, 71-215.

Oldenburg, D.W., and Li, Y., 1999: Estimating depth of investigation in dc resistivity and IP surveys. Geophysics, 64(2), 403-416.

O'Sullivan, M.J., Bodvarsson, G.S., Pruess, K., and Blakeley, M.R., 1985: Fluid and Heat Flow in Gas-Rich Geothermal Reservoirs. Society of Petroleum Engineers Journal, 25 (2), 215–226.

O'Sullivan, M.J., Pruess, K., and Lippmann, M.J., 2001: State of the art of geothermal reservoir simulation. Geothermics, 30 (4), 395-429.

Papp, B., Deák, F., Horváth, Á., Kiss, Á., Rajnai, G., and Szabó, Cs, 2008: A new method for the determination of geophysical parameters by radon concentration measurements in bore-hole. Journal of Environmental Radioactivity, 99(11), 1731–1735.

Patacca, E., and Scandone, P., 2001: Late thrust propagation and sedimentary response in the thrust-belt–foredeep system of the Southern Apennines (Pliocene-Pleistocene). In: Vai G.B., Martini I.P. (eds) Anatomy of an Orogen: the Apennines and Adjacent Mediterranean Basins. Springer, Dordrecht.

Patacca, E., Sartori, R., and Scandone, P., 1993: Tyrrhenian basin and Apennines. Kinematic evolution and related dynamic constraints. In: Recent evolution and seismicity of the Mediterranean region. Springer Netherlands, 161-171.

Parasnis, D.S. 1986: Electrical methods. In: Principles of Applied Geophysics, Springer, Dordrecht, 104-172.

Parolai, S., Bormann, P., and Milkereit, C. 2002: New relationships between Vs, thickness of sediments, and resonance frequency calculated by the H/V ratio of seismic noise for the Cologne area (Germany). Bulletin of the Seismological Society of America, 92(6), 2521-2527.

Park, S.K., and Wernicke, B. 2003: Electrical conductivity images of Quaternary faults and Tertiary detachments in the California Basin and Range. Tectonics, 22(4), 1030.

Pasierb, B., 2012: Resistivity tomography in prospecting geological surface and anthropogenic objects. Czasopismo Techniczne, 23, 201-209.

Person, M., and Garven, G., 1992: Hydrologic constraints on petroleum generation within continental rift basins: Theory and application to the Rhine graben. American Association of Petroleum Geologists Bulletin, 76, 468-488.

Person, M., and Garven, G., 1994: A sensitivity study of the driving forces on fluid flow during continental-rift basin evolution. Geological Society of America Bulletin, 106, 461-475.

Petersson, A.J., 1907: Method of charging electric furnaces for producing carbid from lime and carbon. U.S. Patent No. 863-044.

Pettinelli, E., Beaubien, S.E., and Zaja A.,2010: Characterization of a CO2 gas vent using various geophysical and geochemical methods. Geophysics, 75 (3), B137-B146.

Picotti, S., Carcione, J.M., Gei, D., Rossi, G., and Santos J.E., 2012: Seismic modeling to monitor CO2 geological storage: The Atzbach-Schwanenstadt gas field. Journal of Geophisical Research, 117 (B6),https://doi.org/10.1029/2011JB008540.

Pidlisecky, A., Haber, E., and Knight, R., 2007: RESINVM3D: A 3D resistivity inversion package. Geophysics, 72(2), H1-H10.

Porfido, S., Esposito, E., Vittori, E., Tranfaglia, G., Guerrieri, L., and Pece, R., 2007: Seismically induced ground effects of the 1805, 1930 and 1980 earthquakes in the Southern Apennines (Italy). Bollettino della Societa Geologica Italiana, 126(2), 333–346.

Pritchett, J.W., Rice, M.H., and Riney, T.D., 1981: Equation-of-State for Water-Carbon Dioxide Mixtures: Implications for Baca Reservoir. Report DOE/ET/27163-8, Systems, Science and Software, La Jolla, CA.

Pruess, K., Oldenburg, K., and Moridis, G., 1999: TOUGH2 user's guide, version 2.0, Lawrence Berkeley National Laboratory, University of California, Berkeley.

Raffensperger, J.P., and Garven, G., 1995a: The formation of unconformity-type uranium ore deposits, 1, Coupled groundwater flow and heat transport modeling. American Journal of Science, 295, 581-636.

Raffensperger, J.P., and Garven, G., 1995b: The formation of unconformity-type uranium ore deposits. 2. Coupled hydrochemical modeling. American Journal of Science, 295, 639-696.

Ramirez, A., Daily, W., LaBrecque, D., Owen, E., and Chesnut, D., 1993: Monitoring an underground steam injection process using electrical resistance tomography. Water Resources Research, 29, 73–87.

Ramirez A., Daily, W., Binley, A., LaBrecque, D., and Roelant, D., 1996: Detection of leaks in underground storage tanksusing electrical resistance methods. Journal of Engineering and Environmental Geophysics,1(3), 189–203.

Ravenhurst, C.E., and Zentilli, M., 1987: A model for the evolution of hot (>200 C) overpressured brines under an evaporite seal: the Fundy/Magdalen Carboniferous Basin of Atlantic Canada and its associated Pb-Zn-Ba deposits. In: Sedimentary Basins and Basin Forming Mechanisms. Canadian Society of Petroleum Geologists, 12, 335–350.

Revil, A., Karaoulis, M., Johnson, T., and Kemna, A., 2012: Review: Some low-frequency electrical methods for subsurface characterization and monitoring in hydrogeology. Hydrogeology Journal, 20, 617-658.

Revil, A., Schwaeger, H., Cathles, L.M., Manhardt, P., 1999: Streaming potential in porous media. 2. Theory and application to geothermal systems. Journal of Geophysical Research, 104 (B9), 20033-20048.

Reynolds, J.M., 2011: An introduction to applied and environmental geophysics. John Wiley & Sons.

Rittgers, J.B., Sirles, P., Morelli, G., and Occhi, M., 2010: Case history: Monitoring resin injections with the aid of 4D geophysics. In: 23rd EEGS Symposium on the Application of Geophysics to Engineering and Environmental Problems (pp. cp-175). European Association of Geoscientists & Engineers.

Roure, F., Casero, P., and Vially, R., 1991: Growth processes and melange formation in the southern Apennines accretionary wedge. Earth and Planetary Science Letters, 102(3-4), 395-412.

Rovida, A., Locati, M., Camassi, R., Lolli, B., and Gasperini, P., 2016: CPTI15, the 2015 version of the Parametric Catalogue of Italian Earthquakes: Istituto Nazionale di Geofisica e Vulcanologia.

Rucker, D.F., McNeill, M., Schindler, A., and Noonan, G., 2009: Monitoring of a secondary recovery application of leachate injection into a heap. Hydrometallurgy, 99(3-4), 238-248.

Saito, H., Nobuoka, D., Azuma H., Xue Z., and Tanase, D., 2006: Time-Lapse Crosswell Seismic Tomography for Monitoring Injected CO2 in an Onshore Aquifer, Nagaoka, Japan. Journal Exploration Geophysics, 37 (1), 30–36.

Santangelo, N., and Santo, A. 1991: Endokarstic evolution of carbonatic massifs in Campania (southern Italy): Geological and geomorphological implications. Proceedings of the International Conference on Environmental Changes in Karst areas: ICECKA: Italy, September 15th–27th, 1991. Quaderni del Dipartimento di Geografia, 13, 83-93.

Santo, A., Ascione, A., Del Prete, S., Di Crescenzo, G., and Santangelo, N., 2011: Collapse sinkholes distribution in the carbonate massifs of central and southern Apennines. Acta Carsologica, 40, 95–112.

Sartori, R., 2003: The Tyrrhenian back-arc basin and subduction of the Ionian lithosphere. Episodes, 26, 217-221.

Sasaki, Y. 1992: Resolution of resistivity tomography inferred from numerical simulation 1. Geophysical Prospecting, 40(4), 453-463.

Schaaf, A., and Bond, C.E., 2019: Quantification of uncertainty in 3-D seismic interpretation: implications for deterministic and stochastic geomodeling and machine learning. Solid Earth, 10, 1049–1061.

Serva, L., Esposito, E., Guerrieri, L., Porfido, S., Vittori, E., and Comerci, V., 2007: Environmental effects from five historical earthquakes in southern Apennines (Italy) and macroseismic intensity assessment: Contribution to INQUA EEE Scale Project: Quaternary International, 173(17), 30–44.

Schlaf, J., Randen, T., and Sonneland, L., 2005: Introduction to seismic texture. In: Iske A., Randen T. (eds) Mathematical Methods and Modelling in Hydrocarbon Exploration and Production. Mathematics in Industry, vol 7. Springer, Berlin, Heidelberg.

Shiner, P., Beccacini, A., and Mazzoli, S., 2004: Thin-skinned versus thick-skinned structural models for Apulian Carbonate Reservoirs: constraints from the Val D'Agri Fields. Marine Petroleum Geology, 21, 805-827.

Sharma, P.V., 1997: Environmental and Engineering Geophysics. Cambridge University Press, UK.

Schlumberger, C., 1920: Etude sur la prospection electrique du sous-sol. Gauthier-Villars.

Schmidt-Hattenberger, C., Bergmann, P., Kießling, D., Krüger, K., Rücker, C., Schütt, H., Ketzin Group, 2011: Application of a Vertical Electrical Resistivity Array (VERA) for Monitoring CO2 Migration at the Ketzin Test Site: First Performance Evaluation. Energy Procedia, 4, 3363-3370.

Schuermans, B., Bellucci, V., and Paschereit, C.O., 2003: Thermoacoustic modeling and control of multi burner combustion systems. In: ASME Turbo Expo 2003, collocated with the 2003 International Joint Power Generation Conference (pp. 509-519). American Society of Mechanical Engineers Digital Collection.

Sherlock, V., Connor, B., Robinson, J., Shiona, H., Smale, D., and Pollard, D., 2014: TCCON Data from Lauder, New Zealand, 20HR, Release GGG2014R0. TCCON Data Archive, hosted by the Carbon Dioxide Information Analysis Center, Oak Ridge National Laboratory, Oak Ridge, Tennessee, USA.

Seminsky, K.Z., Zaripov, R.M., and Olenchenko, V.V., 2016: Interpretation of shallow electrical resistivity images of faults: tectonophysical approach. Russian Geology and Geophysics, 57(9), 1349-1358.

Smith, L., and Chapman, D.S., 1983: On the thermal effects of groundwater flow, 1, Regional scale systems. Journal of Geophysical Research, 88, 593-608.

Speranza, F., and Chiappini, M., 2002: Thick-skinned tectonics in the external Apennines, Italy: New evidence from magnetic anomaly analysis. Journal of Geophysical Research, 107, 2290.

Steckler, M.S., Piana Agostinetti, N., Wilson, C.K., Roselli, P., Seeber, L., Amato, A., Lerner-Lam, A., 2008: Crustal structure in the Southern Apennines from teleseismic receiver functions. Geology, 36(2), 155–158.

Sudha, K., Tezkan, B., Israil, M., and Rai, J. 2011: Combined electrical and electromagnetic imaging of hot fluids within fractured rock in rugged Himalayan terrain. Journal of Applied Geophysics, 74(4), 205-214.

Sumner, J.S., 1976: Principles of induced polarization for geophysical exploration. Elsevier

Suppe, J., 1983: Geometry and Kinematic of fault bend folding. Am. J. Sci. 283, 684-721.

Suppe, J., and Medwedeff, D.A., 1990: Geometry and kinematics of fault-propagation folding. Eclogae Geolicae Helveticae, 83, 409-454.

Sutton, F.M., and Mc Nabb, A., 1977: Boiling Curves at Broadlands Field, New Zealand. N. Z. J. Sci., 20, 333–337.

Suzuki, K., Toda, S., Kusunoki, K., Fujimitsu, Y., Mogi, T., and Jomori A., 2000: Case studies of electrical and electromagnetic methods applied to mapping active faults beneath the thick quaternary. Eng. Geol. Amsterdam, 56, 29–45, doi:10.1016/S0013-7952(99)00132-5.

Telford, W.M., Telford, W.M., Geldart, L.P., and Sheriff, R.E., 1990: Applied Geophysics. Cambridge University Press.

Taner, M.T., Koehler, F., and Sheriff, R.E., 1979: Complex seismic trace analysis. Geophysics, 44(6), 1041-1063.

Tannert, C., Elvers, H.-D., and Jandrig, B., 2007: The Ethics of Uncertainty: In the Light of Possible Dangers, Research Becomes a Moral Duty. EMBO reports, 8, 892–896.

Tejero-Andrade, A., Argote-Espino, D.L., Cifuentes-Nava, G., Hernández-Quintero, E., Chávez, R.E., and García-Serrano, A., 2018: 'Illuminating' the interior of Kukulkan's Pyramid, Chichén Itzá, Mexico, by means of a non-conventional ERT geophysical survey. Journal of Archaeological Science, 90, 1-11.

Thore, P., Shtuka, A., Lecour, M., Ait-Ettajer, T., and Cognot, R., 2002: Structural Uncertainties: Determination, Management, and Applications. Geophysics, 67, 840–852.

Thiele, S.T., Jessell, M.W., Lindsay, M., Wellmann, J.F., and Pakyuz-Charrier, E., 2016: The Topology of Geology 2: Topological Uncertainty, J. Struct. Geol., 91, 74–87.

Trautz, R.C., Pugh, J.D., Varadharajan, C., Zheng, L., Bianchi, M., Nico, P.S., and Dafflon, B., 2013: Effect of dissolved CO2 on a shallow groundwater system: A controlled release field experiment. Environmental Science & Technology, 47(1), 298-305.

Turco, E., Macchiavelli, C., Mazzoli, S., Schettino, A., and Pierantoni, P.P., 2012: Kiematic evolution of Alpine Corsica in the framework of Mediterranean mountain belts. Tectonophysics, 579, 193-206.

Uhlemann, S., Kuras, O., Richards, L.A., Naden, E., and Polya, D.A., 2017: Electrical resistivity tomography determines the spatial distribution of clay layer thickness and aquifer vulnerability, Kandal Province, Cambodia. Journal of Asian Earth Sciences, 147, 402-414.

Valensise, G., and Pantosti, D., 2001: Seismogenic faulting, moment release patterns and seismic hazard along the central and southern Apennines and Calabrian Arc. In: Vai, G.B., and Martini, I.P., eds., Anatomy of an Orogen: The Apennines and Adjacent Mediterranean Basins. Dordrecht, The Netherlands, Kluwer Academic Publishing, 495– 512.

Valente, E., Ascione, A., Ciotoli, G., Cozzolino, M., Porfido, S., and Sciarra, A., 2018: Do moderate magnitude earthquakes generate seismically induced ground effects? The case study of the M w= 5.16, 29th December 2013 Matese earthquake (southern Apennines, Italy). International Journal of Earth Sciences, 107(2), 517-537.

Vandeweijer, V., van der Meer B., Hofstee C., Mulders F., D'Hoore D., and Graven H., 2011: Monitoring the CO2 injection site: K12-B. Energy Procedia, 4, 5471 – 5478.

Vanneste, K., Verbeeck, K., and Petermans, T. 2008: Pseudo-3D imaging of a low-slip-rate, active normal fault using shallow geophysical methods: The Geleen fault in the Belgian Maas River valleyImaging a slow active normal fault in 3D. Geophysics, 73(1), B1-B9.

Vargas, D., Cifuentes, G., Hernandez, J.E., and Chavez, R.E., 2014: Non-conventional 3D electric resistivity tomography arrays. In: Near Surface Geoscience 2014-20th European Meeting of Environmental and Engineering Geophysics (Vol. 2014, No. 1, pp. 1-5). European Association of Geoscientists & Engineers.

Vitale, S., Dati, F., Mazzoli, S., Ciarcia, S., Guerriero, V., and Iannace, A., 2012: Modes and timing of fracture network development in poly-deformed carbonate reservoir analogues, Mt. Chianello, southern Italy. Journal of Structural Geology, 37, 223-235.

Vitale, S., Prinzi E.P., Tramparulo, F., De Paola C., Di Maio R., Piegari E., Sabbatino M., Natale J., Notaro P., and Ciarcia S., 2020: Late Miocene-early Pliocene out-of-sequence thrusting in the southern Apennines (Italy). Journal of Geodynamics (submitted).

Viero, G., Lunelli, L., Passerini, A., Bianchini, P., Gilbert, R. J., Bernabò, P., Tebaldi, T., Diaspro, A., Pederzolli C., and Quattrone, A., 2015: Three distinct ribosome assemblies modulated by translation are the building blocks of polysomes. Journal of Cell Biology, 208(5), 581-596.

Walia, V., Lin, S.J., Fu, C.C., Yang, T.F., Hong, W.L., Wen, K.L., and Chen, C.H., 2010: Soil-gas monitoring: a tool for fault delineation studies along Hsinhua Fault (Tainan), Southern Taiwan. Applied Geochemistry, 25(4), 602–607.

Walsh, J.J., Bailey, W.R., Childs, C., Nicol, A., and Bonson, C.G., 2003a: Formation of segmented normal faults: a 3-D perspective. J. Struct. Geol., 25, 1251-1262.

Walsh, J.J., Childs, C., Imber, J., Manzocchi, T., Watterson, J., and Nell, P.A.R., 2003b: Strain localisation and population changes during fault system growth within the Inner Mora Firth, Northern North Sea. J. Struct. Geol., 25, 307-315.

West, B., May, S., Eastwood, J.E., and Rossen, C., 2002: Interactive seismic facies classification using textural and neural networks. The Leading Edge, 21, 1042-1049.

Wieck, J., Person, M., and Strayer, L., 1995: A finite element method for simulating fault block motion and hydrothermal fluid flow within rifting basins. Water Resources Research, 31, 3241-3258.

Wilson, M., and Monea, M., 2004: IEA GHG Weyburn CO2 Monitoring & Storage Operation Summary Report 2000–2004 (Regina: Petroleum Technology Research Centre).

Wise, D.J., Cassidy, J., and Locke, C.A., 2003: Geophysical imaging of the Quaternary Wairoa North Fault, New Zealand: A case study. J. Appl. Geophys., 53, 1–16.

Yang, T.F., Chou, C.Y., Chen, C.H., Chyi, L.L., and Jiang, J.H., 2003: Exhalation of radon and its carrier gases in SW Taiwan. Radiation Measurements, 36, 425–429.

Yang, T.F., Walia, V., Chyi, L.L., Fu, C.C., Chen, C.-H., Liu, T.K., Song, S.R., Lee, C.Y., and Lee, M., 2005: Variations of soil radon and thoron concentrations in a fault zone and prospective earthquakes in SW Taiwan. Radiation Measurements, 40, 496–502.

Zhang, M., Lin, H., Sun, H., and Cai, Y., 2019: Estimation of Net Primary Production Using Landsat 8 Time Series in a Heavily Urbanized Area, Central China. Remote Sensing, 2019, 11(2), 133.

Zavalishin, B.R., 2000: Diffraction problems of 3D seismic imaging. Geophys. Prospect., 48, 631-645.